Universidad Politécnica de Valencia
Departamento de Física Aplicada

Tesis Doctoral

Ultrasonic transmission through periodically perforated plates

Autor:

Héctor Estrada Beltrán

Director:

Dr. Antonio Uris Martínez

Tutor:

Prof. Francisco Javier Meseguer Rico

Organismo:

Centro de Tecnologías Físicas
Unidad Asociada ICMM-CSIC/UPV

Valencia, Octubre de 2011

Agradecimientos

La presente tesis doctoral no hubiera sido posible sin la ayuda de mucha gente a la cual quiero mostrar mi agradecimiento en estas líneas.

A Jaime Llinares por orientarme, darme la oportunidad de hacer el doctorado y presentarme a Francisco Meseguer.

A Francisco Meseguer por depositar su confianza en mí para participar en este proyecto, por mostrarme el mundo fascinante de la física y guiarme en el campo de la investigación.

A Antonio Uris por su dedicación como director de este trabajo y por transmitirme su constancia y empuje.

A Francisco Belmar y Pilar Candelas por iniciarme en el mundo de los ultrasonidos y de los taladros, por su guía en los entresijos del doctorado y por las horas de fresadora y de medidas que compartimos.

A Javier García de Abajo por su inestimable ayuda con los modelos teóricos, por su paciencia y por mostrarme el mundo de la física teórica y el arte de los modelos numéricos.

A José M. Bravo por su entusiasmo y ayuda con los experimentos y los cálculos de FEM.

Al CSIC por la beca JAE-predoctoral, gracias a la cual he podido desarrollar esta investigación a tiempo completo.

Al grupo de metamateriales del Centro de Tecnologías Físicas por el excelente ambiente de trabajo. A Roberto Fenollosa por las conversaciones siempre interesantes sobre física y su ayuda en el laboratorio. A Isabelle Rodríguez por su gran ayuda con el lado químico de la fuerza. A Fernando Ramiro por esas entretenidas conversaciones y por su interés por las cosas del otro lado del Atlántico. A Michal Tymczenko por hacerme hablar en inglés. A Fernando y a Michal por su ayuda con los cacharros del taller y del

laboratorio para los montajes experimentales, por su consejo y ayuda con Maquinón y por sus discusiones de Mac contra PC. A Moisés Garín por ser un férreo defensor y promotor del sofware libre, la limpieza y la seguridad en el trabajo. A Ana Moreno por su ayuda en el laboratorio y su compañía a la hora de comer y a Elisabet Xifré y a Elvira Bonet por alegrarme las mañanas. A Umut y a Lei por las amenas e interesantes conversaciones de camino a casa.

A Fernando Cabrelles por su ayuda con el montaje experimental y la fresadora, por enseñarme que las cosas pueden ser más difíciles que lo que uno piensa y más fáciles que lo que uno imagina.

Al grupo de Javier: Rebecca, Isabel, Alejandro, Xesús, Viktor y Johan por las amenas conversaciones sobre física y la inmejorable compañía en Madrid y en congresos.

A Vicente y Ana por su acogida, su apoyo, su ejemplo y su consejo. A Vicent por hacerme sentir como en casa y a Ana por su excelente sentido del humor.

A mis padres, Héctor e Idelvira, por su esfuerzo y su apoyo desde la distancia, por su entrega, su comprensión y su generosidad. A mis hermanas, Victoria y Verónica, por su alegría y complicidad.

A mi esposa Ana, por su paciencia, su apoyo constante y su amor.

Abstract

Being capable of mimicking some phenomena inherent in atomic scales, macroscopic periodic structures have been subject to intensive research in the last two decades. Perforated plates, although a very common periodic structure, seem to keep unexplored sound transmission properties, whose study has been triggered by the discovery of Extraordinary Optical Transmission through subwavelength holes perforated in metallic plates while interacting with light.

In this work it is shown that perforated plates do not only exhibit full transmission resonant peaks and Wood anomaly minima when the holes are arranged periodically, but also extraordinary sound screening due to the hydrodynamic short circuit arising from the coupling between the plate and the fluid.

Furthermore, the role of the geometrical parameters of the perforated plates in the transmission features is also reported here illustrating different strategies to tailor the transmission spectrum.

High complexity transmission was observed for periodically perforated aluminum plates immersed in water when the incidence angle is varied. Leaky surface waves coming from the vibration of the plate arise, which is demonstrated using a new theoretical model involving full elasto-acoustic coupling.

A complete landscape of the coupling effect is portrayed thanks to the complementary study of solid-solid phononic plate transmission and in-plate wave propagation. As a direct consequence, Scholte-Stoneley-like modes folding and band gap are observed without the need of corrugations or holes.

Finally, the transmission properties of individual holes and hole arrays for light, electrons, and sound are put together. The differences are analyzed and discussed here. It has been found that, although for light the hole array itself leads to 100% transmission and surface bound modes, this is neither the case for sound nor for electrons. Thus, hole

resonances are the key mechanism that enables the occurrence of exotic phenomena for sound. The main results mentioned here are thoroughly explained and discussed based on theoretical and experimental data.

Resumen

Las estructuras periódicas macroscópicas han sido objeto de una intensa investigación durante las dos últimas décadas debido a su capacidad de imitar fenómenos ondulatorios que son inherentes a la escala atómica. Aunque las placas perforadas son estructuras muy comunes en acústica, éstas parecen guardar propiedades de transmisión de sonido inexploradas, cuyo estudio ha sido impulsado por el descubrimiento de la Transmisión Óptica Extraordinaria en láminas de metal perforadas con agujeros distribuidos periódicamente cuando interactúan con la luz.

En el presente trabajo se muestra que las placas perforadas no sólo presentan máximos de transmisión total resonante y mínimos de la anomalía de Wood cuando los agujeros están distribuidos de forma periódica, sino también apantallamiento acústico extraordinario debido al cortocircuito hidrodinámico producido por el acoplamiento entre la placa y el fluido.

También se detalla el rol de los parámetros geométricos de las placas perforadas en las características de transmisión, ilustrando diferentes estrategias para moldear el espectro de transmisión.

La transmisión acústica a través de placas de aluminio con perforaciones regulares sumergidas en agua presenta una alta complejidad tanto a incidencia normal como cuando se varía el ángulo de incidencia del sonido. Aparecen ondas de superficie radiantes provenientes de la vibración de la placa, lo cual es demostrado usando un nuevo modelo teórico que incluye el acoplamiento elastoacústico completo.

Gracias al estudio complementario de la transmisión y la propagación en placa de una placa fonónica sólido-sólido se retrata una perspectiva completa del efecto del acoplamiento. Como consecuencia directa, se observan fenómenos de plegamiento y bandas de propagación prohibida en modos tipo Scholte-Stoneley sin necesidad de corrugaciones o de agujeros.

Finalmente, se comparan las propiedades de transmisión de agujeros individuales y redes de agujeros para luz, electrones y sonido analizando y comentando sus diferencias. Se ha encontrado que, aunque para la luz la red de agujeros en sí misma lleva a transmisiones del 100 % y modos atrapados a la superficie, esto no se produce ni para electrones ni para sonido. En consecuencia, las resonancias del agujero constituyen el mecanismo clave que posibilita la existencia de fenómenos exóticos en sonido. Los resultados principales aquí mencionados son explicados de manera detallada y comentados sobre la base de datos teóricos y experimentales.

Resum

Les estructures periòdiques macroscòpiques han sigut objecte d'una intensa investigació durant les dos últimes dècades degut a la seua capacitat d'imitar fenòmens ondulatoris que són inherents a l'escala atòmica. Encara que les plaques perforades són estructures molt comunes en acústica, aquestes pareixen guardar propietats de transmissió de so inexplorades, l'estudi de les quals ha sigut impulsat pel descobriment de la Transmissió Òptica Extraordinària en làmines de metall perforades amb forats distribuïts periòdicament quan interactuen amb la llum.

En el present treball es mostra que les plaques perforades no sols presenten màxims de transmissió total ressonant i mínims de l'anomalia de Wood quan els forats estan distribuïts de forma periòdica, sinó també apantallament acústic extraordinari a causa del curtcircuit hidrodinàmic produït per l'acoplament entre la placa i el fluid.

També es detalla el rol dels paràmetres geomètrics de les plaques perforades en les característiques de transmissió, il·lustrant diferents estratègies per a modelar l'espectre de transmissió.

La transmissió acústica a través de plaques d'alumini amb perforacions regulars submergides en aigua presenta una alta complexitat tant a incidència normal com quan es modifica l'angle d'incidència del so. Apareixen ones de superfície radiants provinents de la vibració de la placa, fet que és demostrat usant un nou model teòric que inclou l'acoplament elastoacústic complet.

Gràcies a l'estudi complementari de la transmissió i la propagació en placa d'una placa fonónica sòlid-sòlid es retrata una perspectiva completa de l'efecte de l'acoplament. Com a conseqüència directa, s'observen fenòmens de plegament i bandes de propagació prohibida en modes tipus Scholte-Stoneley sense necessitat de corrugacions o de forats.

Finalment, es comparen les propietats de transmissió de forats individuals i xarxes de forats per a llum, electrons i so analitzant i comentant les seues diferències. S'ha

trobat que, encara que per a la llum la xarxa de forats en si mateixa porta a transmissions del 100 % i modes atrapats a la superfície, açò no es produeix ni per a electrons ni per a so. En conseqüència, les ressonàncies del forat constitueixen el mecanisme clau que possibilita l'existència de fenòmens exòtics en so. Els resultats principals ací mencionats són explicats de manera detallada i comentats sobre la base de dades teòriques i experimentals.

List of acronyms

PPP Periodically Perforated Plate

EOT Extraordinary Optical Transmission

ET Extraordinary Transmission

FPR Fabry-Pérot Resonance

FEAM Full Elasto-Acoustic Model

FEM Finite Element Method

IL Insertion Loss

NiPEM Nearfield in-Plate Excitation Measurement

PMMA Poly-methyl metacrylate

PVDF Polyvinylidene fluoride

PhP Phononic Plate

RSM Rigid-Solid Model

ST Subwavelength Transmission

TL Transmission Loss

Contents

1

Introduction

Nature provides very good examples of periodic organization at different scales. When the repeated element is an atom we are dealing with solids and more particularly with crystals. The understanding of how electrons behave in a periodic array of atoms was the keystone contribution of Felix Bloch in 1928. At the light of quantum theory [1], Bloch considered electrons as matter waves and was able to explain the conductivity phenomenon in metals, which subsequently led to the exploration of the electronic properties of semiconductors and constitutes the basis behind any electronic device.

Other structures found in nature that display periodicity, this time at a scale of hundreds of nanometers, are opals and peacock feathers [2] among others [3]. As can be seen in Fig. 1.1, both share fascinating optical properties. Although crystals, opals, and peacocks are known from very long time ago, the connection between the behavior of electrons in crystals and that of light in sub-micron periodic structures was not realized until nearly twenty years ago [4, 5].

Brillouin [6] already pointed out the similarities that electrons, electromagnetic waves, and sound waves share when propagating through periodic structures. His pioneering work describes the existence of pass and stop frequency bands and sets the principles for their analysis. In this spirit, phenomena found at atomic scales in ordered systems could be resembled by light and sound. From this development emerges the concept of phononic [7, 8] and photonic [9, 10] crystals. Briefly speaking, an ordered arrangement of one or more materials embedded in a host material constitutes a phononic or photonic crystal if the wave propagation properties of the constituent materials differ in a manner that enables the observation of wave propagation features more related with the periodicity than with the properties of the crystal building blocks.

(a)

(b)

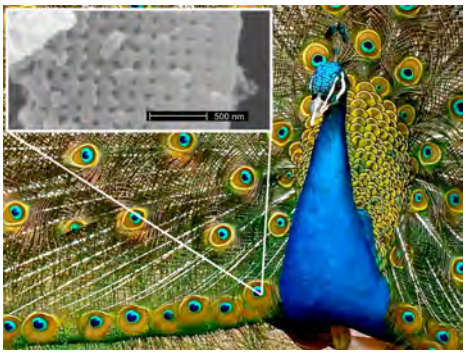

Figure 1.1: Examples of natural sub-micron-scale periodic structures. (a) An opal doublet from Andamooka South Australia (from CRPeters). (b) Peacock and scanning electron microscopic image of a peacock feather revealing the underlying periodic structure (from [2]).

Properties typically observed in solid-state physics overcame its natural boundaries and reached then larger scales. The importance of phononic and photonic crystals comes from the fact that the translated properties cannot be achieved by means of conventional materials, opening a new way for the control of waves. One important property of wave crystals is the existence of frequency regions where the wave propagation through the crystal is forbidden [5, 11]. These frequency regions are called band-gaps and their importance comes from the fact that they enable the localization of waves [4, 12] in crystal defects. Furthermore, when several crystal defects are coupled, waveguiding effects can be observed [13, 14] through the chain of defects. The complexity that the periodicity adds to the band structure can also enable negative refraction phenomena [15, 16], which can be further used to achieve strong focusing effects.

In addition, the development of acoustic metamaterials [17] brought into focus the wide range of possibilities of locally resonant structures. In contrast to phononic crystals, most features of acoustic metamaterials show up at wavelengths larger than the period of the array because their constituents exhibit low frequency resonances which are directly involved in the wave propagation phenomena.

Periodic structures can also be used in the long wavelength regime to change almost arbitrarily the effective elastic wave propagation constants of the medium. This additional degree of freedom makes more feasible the otherwise chimerical concept of cloaking [18, 19]. Objects can be detected by waves if they produce a significant distortion in the wave propagation behavior. Then, an object could be undetectable or even

invisible if it is covered by a medium (the cloak) which can minimize the wave field distortion.

Besides natural periodic structures, Periodically Perforated Plates (PPPs) or membranes are, nowadays, probably one of the most common man made structures and they are used in many different applications (see Fig. 1.2). Most applications take advantage of the rigidity of the solid and the permeability to air flow and light provided by the apertures. Its geometry is fairly simple, allowing their mass-production.

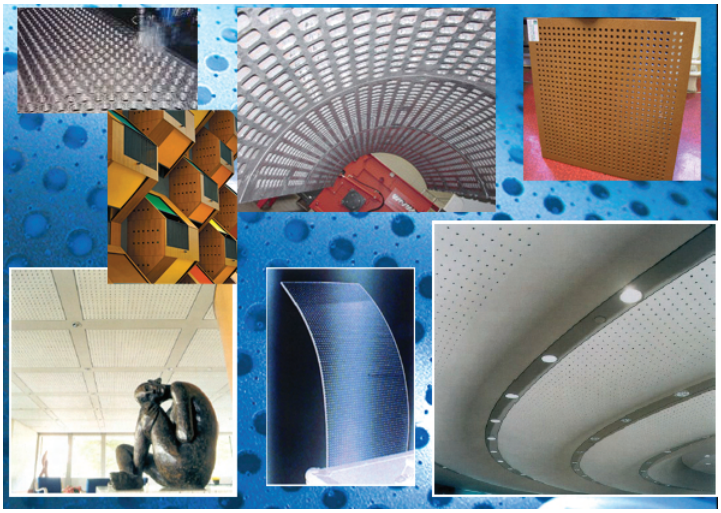

Figure 1.2: Perforated plates are everywhere

Moreover, PPPs and panels are an old ally of the acoustician. They constitute an important part in the toolbox of an acoustic engineer [20] and therefore, their acoustical properties are well known when the size of the aperture is many times smaller than the wavelength λ. In fact, one of the most common solutions used in architectural acoustics to achieve sound absorption and avoid unwanted reflections comprises a rigid wall, an air cavity, sound absorbing material, and a perforated panel. Further applications where perforated plates are involved also include exhaust pipe silencers for noise control purposes, widely used in either large industrial processes or in internal combustion engine vehicles.

Beyond the deep subwavelength regime in which PPPs are used and hence their properties known, the regime where the wavelength is of the same order of magnitude than the distance between the holes still remained unexplored. The motivation to further study the properties of PPPs in this unexplored regime comes after the experimental dis-

covery of Extraordinary Optical Transmission (EOT) through a periodically perforated metallic membrane [21] and the evidence of analogies between photonic and phononic crystals [11]. Ebbesen et al. [21] demonstrated experimentally that periodic arrays of subwavelength holes drilled on a metallic membrane transmit much more light per hole than expected from Bethe's theory [22] for a single opening (see Fig. 1.3). This effect occurred at specific wavelengths strongly correlated with the period of the hole array, which suggests a cooperative interaction between holes.

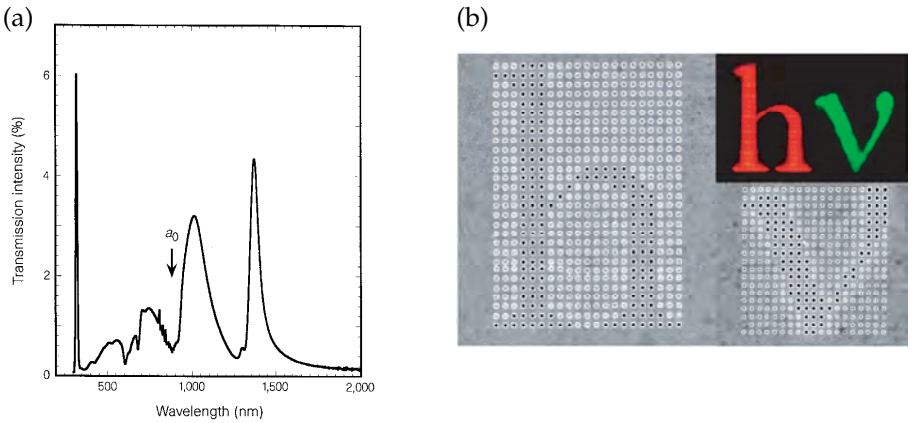

Figure 1.3: (a) First report on EOT on a metallic silver film decorated with a periodic distribution of holes (from [21]). (b) Further refinement of the structure using dimple arrays and white light illumination (from [23]).

EOT has been predicted theoretically and reported experimentally in slit arrays [24, 25, 26, 27] and hole arrays [21, 28, 29, 30] in numerous studies and over a wide range of wavelengths [31, 32, 33]. After a strong debate, several mechanisms have been identified to contribute to EOT, such as surface plasmon resonances [30, 34], cavity resonances [35], and dynamical diffraction [25], all of them describable using a simple analytical formulation [35]. A comprehensive review of EOT phenomena can be found in [36].

Although in the broad sense Brillouin's hypothesis on the similarity of wave phenomena can be regarded as correct, there are subtle fundamental details that make them different. An appropriate contextualization is required when comparing wave phenomena, otherwise the misunderstanding can be guaranteed. For instance, considering the simple case of an object travelling faster than the wave velocity and comparing what happens in the case of sound and light one arrives to very different scenarios. While for

sound it corresponds to supersonic displacement (perfectly plausible), for light it would imply a deep revision of Einstein's general relativity. Even though the previous example is very dramatic, it clearly represents the risk taken when optical phenomena are simply translated to acoustics.

Into PPPs converge several aspects that make them interesting and worth of being studied. One aspect is related with the possibility of finding interesting physics and phenomena which can be exotic in acoustics using a fairly common system. Another aspect is the opportunity to test how far holds the analogy between the different manifestations of wave phenomena (i.e. matter, electromagnetic, and sound waves) regarding sound transmission through PPPs. Finally, from a practical viewpoint, the exotic phenomena could be exploited in applications for which an old ally could still be full of surprises.

In the following section, the evolution and the state of the art regarding PPPs is presented from a global point of view. A more detailed exposition on specific themes is given in the different chapters.

1.1 State of the art

The study of sound interaction with periodic structures is rooted at the end of the XIX century with the work of Rayleigh [37], who studied the reflection coefficient of an one-dimensional grating. This study on scalar sound waves served as the basis in his attempt to explain the experimental observations done by Wood [38] while researching optical gratings. Wood reported anomalous sharp reflection spikes (nowadays known as Wood anomalies) which can be partially explained by Rayleigh's successive refinements to his theory of gratings.

Afterwards, most of the efforts concentrated in the study of PPPs and slits arrays at the deep subwavelength regime (i.e. the wavelengths at least two orders of magnitude bigger than the inter-hole distance) for airborne sound applications, where the air inside the holes can be simply considered as an acoustic mass moving back and forth with the impinging sound wave.

Nearly hundred years after Rayleigh, full reflection was reported by Norris and Luo [39] in 1987 for a two-dimensional array of circular holes of period a in a semi infinite rigid-solid when $\lambda = a$, in agreement with Rayleigh results.

Then, following the spirit of Brillouin and looking at an old ally with curious eyes, the wave nature of sound was exploited to study the same structures that give rise to EOT.

For example, sound collimation through a plate having one-dimensional corrugations on both sides with a central aperture was proposed by Christensen et al. [40, 41]

following some ideas from [42]. However, the first attempt of an experimental verification [43] in a two-dimensional bullseye structure showed lower transmission values than expected, probably due to the finite impedance mismatch between water and the brass plate employed in the experiments. More recently, Zhou et al. [44] reported the successful measurement of the collimation effect in airborne sound employing one-dimensional corrugations in a steel plate. In addition, the dispersion of non-leaky modes which participate in the beaming effect has been recently measured by He et al. [45].

The first steps to understand sound transmission through PPPs were mainly concerned with the prediction and observation of resonant full transmission and Wood anomaly transmission dips. Although a monolayer of cylinders arranged periodically is not exactly a PPP, Zhang [46] mimicked a slit array leaving a very narrow air-gap between the cylinders. Already in 2005 he was able to predict full resonant transmission of sound through the cylinder array. Zhou and Kriegsman [47] treated the PPP transmission problem by means of the scattering matrix technique and also predicted the appearance of full transmission peaks in very thick walls.

The experimental confirmation of complete transmission is reported by two groups [48, 49], for a perforated brass plate immersed in water and for a slit array made of steel in air respectively. This full transmission has been called Extraordinary Acoustical Transmission [49] in the same way as EOT.

On the other hand, Estrada et al. [50] studied theoretically and experimentally how geometrical parameters influence the transmission of ultrasound through PPPs. Christensen et al. [51, 41] reported theoretical results in the rigid-solid limit for one- and two-dimensional arrays of square holes, where the dispersion relation of leaky and bounded surface modes is derived. It has been pointed out the hybridization of these modes with the Fabry-Pérot Resonances (FPRs) in the holes.

Whereas for electromagnetic waves there is a big difference between the transmission through a slit or a hole due to the existence of a well defined cutoff in the subwavelength regime for the latter, this is not the case of sound. Transmission of transverse magnetic waves through a slit is dominated by FPRs [52] in similitude to sound in both slit and holes. This point is very well demonstrated in [48] by means of theoretical and experimental comparison of both, electromagnetic waves interacting with a slit array and sound waves interacting with a hole array. Some transmission maxima near the Wood anomaly were, however, erroneously linked to a structure factor resonance, as it has been pointed out by García de Abajo et al. [53].

The situation is complex, because diffractive surface-waves can produce significant deviation of the transmission peaks from the Fabry-Pérot resonant condition. Moreover, it has been argued [44] that the main contribution to the full transmission is due to

Figure 1.4: Pictures of a bone flute found in Hohle Fels, southwestern Germany, dating from 30,000 years ago. (from [54])

evanescent surface waves. It seems that not only the ideas and concepts from EOT have been translated to sound, but also the debate regarding the physical origin of the predicted and observed phenomena.

The differences between optical and acoustical transmission through hole arrays can be traced back to the case of wave transmission through an individual hole. Thus, EOT is extraordinary because the light transmission per hole unit area for an individual hole is much less than unity in the subwavelength regime. However, an individual hole can display sound transmission per hole unit area much larger than unity in the subwavelength regime because of hole resonances across the plate thickness.

The wave nature of sound is evident at a human scale and the same kind of resonances that are responsible for the hole transmission peaks are known from ancient times and are intimately linked with the cultural development of mankind. A recent discovery [54] dates the bone flute depicted in Fig. 1.4 from 30,000 years ago. Their constructors knew very well that the key aspect in its fabrication, in order to produce the desired tones, was the length of the tube. Now, at the beginning of the 21th century, we cannot forget that even if the aperture size is subwavelength, the thickness of the plate may not be subwavelength. Thus, the key ingredient behind all the interesting phenomena that takes place in the sound transmission through perforated plates of finite thickness are the same kind of resonances mankind has been playing with for ages.

Moreover, a diacritical theoretical study on electrons, light, and sound [53] puts the accent on the key role of FPRs in the acoustic phenomenon. It demonstrates, using an analytical method, that in the case of hole arrays pierced periodically in zero thickness films (no hole resonances across the plate thickness) one could still observe EOT, whereas for sound no transmission peak should be expected.

Besides how extraordinary can be a full transmission peak in the sound transmission through hole arrays, Estrada et al. [55] observed that periodically perforated aluminum plates immersed in water transmitted less sound than non perforated plates at certain ultrasonic frequencies near the Wood anomaly. This phenomenon, called extraordinary sound screening, has been numerically studied in more detail for slit arrays recently

[56]. The sound is blocked mainly due to the fluid-solid coupling, which produces an hydrodynamic short-circuit that prevents the forward sound radiation.

Beyond the basic study of the sound transmission through slit or hole arrays, more elaborated structures and possible applications are being considered in addition to different interpretations of the phenomena.

Wang [57, 58] obtained an impedance description of sound transmission through PPPs by assuming piston-like behavior at the hole apertures. In this way, the full transmission near to the Wood anomaly can be understood as induced by the singularity of the radiation impedance of the hole array.

Two layers of PPPs [59, 60] have also been proposed for sound blocking in the rigid solid limit. In addition, Liu and Jin [61] have predicted a suppression of the full transmission peaks due to phase resonances when the hole array basis is asymmetric. Compound arrays have also been considered theoretically in [62] reporting a complex interplay between hole resonance interference and the Wood anomaly.

Subwavelength imaging has been proposed [63, 64] using periodic hole arrays in thick slabs, and confirmed experimentally by Zhu et al. [65] in airborne sound.

Although phononic crystal research started studying bulk wave phenomena, other kind of elastic waves such as Lamb waves [66] have become a target for periodic structures. In fact, Lamb waves are guided waves that propagate through plates and, as demonstrated in [67, 68], they are definitely linked with perforated plates. Recent results on high transmission have been also observed by He et al. [69] for a corrugated brass plate immersed in water without the need of any opening. It has been explained as due to the fluid-solid resonant coupling attributed to a non-leaky elastic surface mode, corroborating the phononic-perforated plate connection. Theoretical [70, 71, 72] and experimental [73, 74, 75] studies dealt firstly with band gap and waveguiding phenomena for air-solid and solid-solid Phononic Plates (PhPs), whereas most recent studies also report negative refraction for flexural [76] and shear horizontal [77] waves.

The work done so far for PhPs is restricted to in-plate vibration, while that done gazing at an acoustic analogy of EOT has been limited to out-of-plate excitation. Whereas most studies on PhPs, particularly those performed towards micro-scale applications, only take into account the elastic wave propagation through the plate and neglect the effect of the surrounding air (which could be treated as vacuum), most of the work done on perforated plates transmission neglects the vibration of the solid and concentrates on wave propagation through the fluid. The same structure can only be analyzed from independent points of view when the coupling between the solid and the fluid is weak enough to be neglected. However, this is only a half of the whole picture and in the

present work the main results point towards the rich physics and complexity one can find when the fluid and the solid interact, leading to a unique scenario for sound waves.

1.2 Problem definition

What motivates this work has been already exposed in the previous sections. Here, the research frame followed in this investigation as well as its main objectives are defined.

The aim of this study is to elucidate by means of theory and experiments the physical phenomena involved in the acoustical transmission through Periodically Perforated Plates (PPPs).

In particular, this work deals with a longitudinal wave in a fluid which impinges on a plate decorated with cylindrical subwavelength holes. Emphasis is placed on the portion of the wave which is transmitted forward to the fluid. This scheme is used not only in the underwater ultrasonic experiments, but also in the theoretical and numerical models.

Several factors that could modify the behavior of PPPs are taken into account such as:

- The orientation of the incident wave with respect to the plate.
- Geometrical parameters including array symmetry, plate thickness, and hole filling fraction.
- Elastic parameters considering the effect of the impedance mismatch between the fluid and the solid.
- The material contained inside the holes studying not only fluid-solid PhPs, but also solid-solid PhPs.

For the particular case of the solid-solid PhP and additional experimental approach consisting in interrogating the plate directly at its surface is employed to complement the information given by the transmission experiments.

From the theoretical perspective, the problem has been tackled starting from different assumptions, which result in several models. The simplest model is derived considering just the effect of the fluid and neglecting its coupling to the solid (Rigid-Solid Model (RSM)) using modal expansion in the holes and Rayleigh expansion in the surrounding fluid. The Full Elasto-Acoustic Model (FEAM) takes into account the vibration of the solid and uses plane wave expansion to extract the eigenvalues of the two dimensional PhP and Rayleigh expansion to match them with the surrounding fluid. Finally, standard

Finite Element Method (FEM) is used to characterize slit arrays under strong fluid-solid coupling.

1.3 Outline

The contents of this work are organized as follows:

Chapter 2: Background

The basic principles and equations concerning mechanical wave propagation in solids and fluid are briefly derived and followed by an overview on the sound transmission problem.

Two classical problems in acoustics are explained in depth as they play a major role in the analysis of hole array results, namely the transmission of sound through homogeneous plates and the transmission of sound through a single hole in a perfectly rigid solid.

Chapter 3: Theory

This chapter describes in detail the theoretical models used in this work. First, geometrical facts and notation common to the analysis of periodic structures are given. Taking advantage of this basis, the RSM is derived. This model neglects the contribution of the solid plate, which is taken into account in the FEAM, which is derived next. In addition, to study the case of strong coupling in slit arrays, the Finite Element Method (FEM) is employed. The details on the numerical calculations performed are also given.

Chapter 4: Experiments

The complete description of the experiments performed for this work is presented here. The convenience of underwater ultrasonic measurements is discussed. Then, a description of the measurement instruments is followed by the definition of the two measurement techniques employed in this work, namely the classic ultrasonic transmission technique and the nearfield measure for in-plate excitation scheme. Finally, detailed information concerning the plate samples measured including their fabrication procedure is covered in this chapter.

Chapter 5: Results analysis

The chapter is devoted to present the experimental and theoretical results followed by data analysis and discussion. The different aspects of the physical phenomena observed in the results are firstly treated separately so that the following sections include complex interactions and hybridization of the phenomena previously described.

The experimental results on resonant transmission at normal incidence are reported and compared to RSM predictions. Wood anomalies are analyzed from the theoretical results for simple and compound arrays. Experimental results on hole array sound screening are analyzed together with numerical finite element results. The feasibility of hole and slit array sound screening applications in different scenarios is discussed. Then, the effect of fluid-solid coupling manifested in surface plate waves is analyzed considering experimental and theoretical data. Complementary experimental measurements for transmission and in-plate excitation are presented and compared with FEAM predictions for solid-solid PhPs.

Chapter 6: Concluding remarks

The interaction of hole arrays with different kinds of waves is discussed. Then, the main results of this work are summarized and an outlook of possible future research lines are sketched.

2

Background

2.1 General elastoacoustics

Acoustical wave phenomena can be well described using continuum mechanics formulations. Since this study requires waves propagating in both, solid and fluid media, a unified framework as that developed in [78] will be followed. Most of the fundamental equations are well known and some of them derived more than a century ago. Therefore, only a brief derivation starting from the fundamental equations up to the linear wave equations, which are valid for small amplitude waves, will be given. Unless explicitly addressed, Einstein's summation convention is employed through this document.

Geometrical considerations

Lets consider a point in the cartesian three-dimensional space plus the time coordinate be described by $\mathbf{r} = (x, y, z, t)$. Thus, the spatial coordinates constitute the independent variables and a spatial description (Eulerian coordinates) is adopted, ignoring the position of a particle in the continuum, which is used as independent variable in the material description (Lagrangian coordinates). Then, given the velocity $\mathbf{v} = v(x, y, z, t)$ in the spatial description, the acceleration (of crucial importance) in the same description yields

$$\frac{dv_n}{dt} = \partial_t v + v_j \partial_j v_n \,, \tag{2.1}$$

where d/dt is the material derivative, $v_j \partial_j$ is known as the convective term, and the subindices j and n run along the space coordinates.

Waves are known to deform the continuum as a function of time. A measure of that deformation is the displacement vector $\mathbf{u} = \mathbf{r} - \mathbf{o}(\mathbf{r}, t)$, where $\mathbf{o}(\mathbf{r}, t)$ identifies the particles position at the time t. The change in the relative positions of the material points in a continuum is called strain and is defined as

$$\epsilon_{jn} = \frac{1}{2}(\delta_{jn} - \partial_j o_k \partial_n o_k) = \frac{1}{2}(\partial_n u_j + \partial_j u_n - \partial_j u_k \partial_n u_k)\,, \tag{2.2}$$

where δ_{jn} denotes the Kronecker delta. In addition, the elongation tensor only takes the linear displacement gradients as

$$\varepsilon_{jn} = \frac{1}{2}(\partial_n u_j + \partial_j u_n)\,. \tag{2.3}$$

Mass and momentum balance

In absence of mass exchange, the mass conservation is given by the continuity equation

$$\partial_t \rho + \partial_n(\rho v_n) = 0\,, \tag{2.4}$$

where density of the continuum ρ is a scalar field.

According to Newton's second law of motion, the rate of change in the momentum must equal the resultant force. Using Eq. (2.1), the momentum equation in absence of body forces can be written as

$$\rho(\partial_t v_n + v_j \partial_j v_n) = \partial_j T_{jn}\,, \tag{2.5}$$

where T_{jn} is the stress tensor. It can be considered as symmetric ($T_{jn} = T_{nj}$) in non-polar materials and it is convenient to assume that it can be separated in a dissipative T'_{jn} and a non-dissipative σ_{jn} part. In absence of shear stresses, e.g. for ideal fluids, and subject to an hydrostatic pressure p, the stress can be written as $\sigma_{jn} = -p\delta_{jn}$.

Energy balance

Thermo-mechanical interactions must satisfy the energy balance, i.e. the increase of energy must equal the work done plus the heat and other non-mechanical energy. Ultimately, the energy balance gives the stress-deformation relation in the case of solids and the state equation for fluids. Considering a reversible isentropic (adiabatic) process in an elastic solid and small displacements as well as small displacement gradients, the stress-deformation relation yields

$$\sigma_{jn} = c_{jnkl}\varepsilon_{kl}\,, \tag{2.6}$$

which is known as Hooke's law, where the coefficients c_{njkl} are components of the stiffness tensor. This tensor can be reduced due to the symmetry of the stress tensor from 81 to 36 components using the Voigt notation of only two subscripts.

In the case of an ideal fluid under reversible isentropic assumptions, the equation of state yields

$$\frac{dp}{dt} = \left(\frac{\partial p}{\partial \rho}\right)_S \frac{d\rho}{dt} = c(\rho, S)\frac{d\rho}{dt}\,, \tag{2.7}$$

where $()_S$ stems for isentropic and c is the sound velocity depending on both, the fluid density and the entropy.

Wave equations

Combining Eqs. (2.4), (2.5), (2.6), neglecting higher order terms, and expressing the equation in terms of the displacement **u** for a locally isotropic solid yields

$$[\partial_j(\lambda\partial_n u_n) + \partial_n\left(\mu(\partial_n u_j + \partial_j u_n)\right)] = \rho\partial_t^2 u_j\,, \tag{2.8}$$

which is the inhomogeneous elastic wave equation where $\lambda = c_{12}$ and $\mu = 1/2(c_{11} - c_{12})$ are the Lamé coefficients valid for locally-isotropic solids. Now ρ is no more a variable but a constant which can be inhomogeneous through the space.

Similarly, the linear wave equation in fluids can be derived combining Eqs. (2.4), (2.5) (known as Euler equation for fluids) , (2.7), and disregarding higher order terms as

$$\partial_t\left(\frac{1}{\rho c^2}\partial_t p\right) = \partial_j\left(\frac{1}{\rho}\partial_j p\right)\,, \tag{2.9}$$

where ρ and c do not variate with the wave but can be inhomogeneous across the space. These two wave equations, namely Eqs. (2.8) and (2.9), are the basis for many studies which deal with sound wave propagation through periodic structures. Further derivations of the different kinds of waves and relations between elastic constants and sound velocities are given in appendix A.1.

2.2 Sound transmission

The transmission of sound through a medium is a very important phenomenon that gives us information about the medium itself and its coupling with a surrounding fluid. As shown in Fig. 2.1, a fluid-filled space $\mathcal{A}$ is divided into two regions separated by an infinite medium or structure $\mathcal{B}$, whose wave propagation characteristics are different from those of the host fluid. An incident wave with wavenumber $k_0 = 2\pi/\lambda_0$ and frequency ω impinges on $\mathcal{B}$ and generates reflected, transmitted, and guided components depending on wave propagation properties of $\mathcal{B}$.

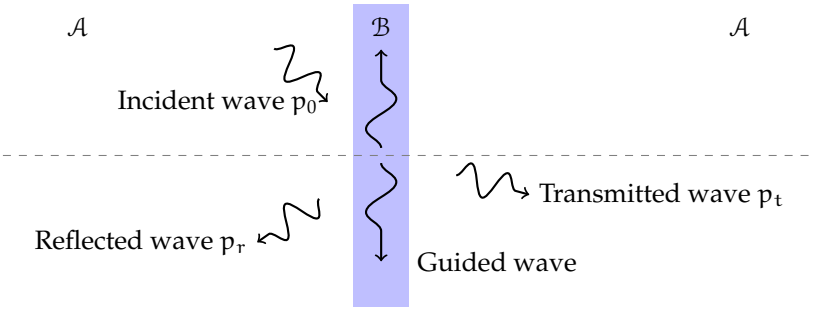

Figure 2.1: Diagram of general wave transmission phenomena. Two semi-infinite fluids $\mathcal{A}$ are separated by an infinite plate $\mathcal{B}$

Some general relations that hold for transmission and reflection problems are given as follows. The conservation of the integrated pulse [79] is given by

$$\int_{-\infty}^{\infty} (p_0 + p_r) dt = \int_{-\infty}^{\infty} p_t \, dt \,, \tag{2.10}$$

and it is valid not only regardless the shape of the incident pulse and the point in the space at which the integrals are taken, but also for finite time perturbations in a three dimensional inhomogeneous fluid. Another basic principle is that related to the symmetry of the wave path, also known as reciprocity principle [79]. This principle states the interchangeability between source and receiver. In terms of sound power, the most basic relation between incident, reflected, and transmitted sound power is the energy conservation law. However, this relation can be very complex and strongly dependent on the acoustical and geometrical properties of the materials involved. Therefore, a general expression cannot be formulated and each case must be analyzed separately.

To quantify the amount of sound energy transmitted through $\mathcal{B}$, the sound power transmission coefficient [80] is defined as $\tau = \Pi_T / \Pi_0$, where Π_0, Π_T correspond to the incident and transmitted sound power respectively. In the case of plane waves τ is related to the pressure transmission coefficient T by $\tau = |T|^2 = |p_T|^2 / |p_0|^2$, with p_0 (p_T) being the pressure amplitude of the incident (transmitted) wave.

If medium $\mathcal{B}$ is an homogeneous solid: flexural, Lamb, Rayleigh, and Scholte-Stoneley waves can propagate depending on the wavelength-to-thickness ratio and the impedance ratio between the solid and the fluid. More complex solid structures like double partitions or multilayer panels can also exhibit acousto-mechanical resonances together with viscous or thermal losses.

How these excited vibrations radiate the sound back and forward to the fluid cannot be answered in a general manner. Indeed, many different phenomena related with the

mechanical coupling between $\mathcal{A}$ and $\mathcal{B}$ and also with the radiation efficiency of the vibrations in $\mathcal{B}$ may take place. And that is just the case of sound transmission through PPPs. Different phenomena are mixed together giving rise to a complex scenario.

2.3 Sound transmission through homogeneous plates

The problem of sound transmission through an isotropic solid is well known and has been extensively studied [66, 81, 82]. Many textbooks about wave propagation in solids and ultrasound [83, 84] deal with this problem. Here is described the model given in [84] due to both its simplicity as well as the minimal assumptions involved in its derivation.

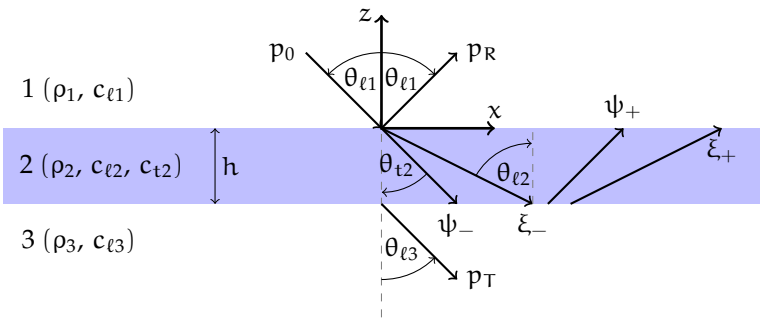

Figure 2.2: Diagram of the sound transmission through a solid plate of thickness h. The elasto-acoustic properties of the three media $j = 1, 2, 3$ are $(\rho_j, c_{\nu j})$ with $\nu = \{\ell, t\}$. As media 1 and 3 are inviscid fluids only $c_{\ell 1}$ and $c_{\ell 3}$ are retained.

The geometry and system of coordinates are depicted in Fig. 2.2. For simplicity, harmonic time excitation is assumed through this work, thus the time component $e^{-i\omega t}$ can be neglected.

The elasto-acoustic properties at each medium $j = 1, 2, 3$ are the density ρ_j and the wave velocity $c_{\nu j}$, where ν represents longitudinal (ℓ) or transverse (t) waves. In the case under study, media 1 and 3 are fluids and therefore only $c_{\ell 1}$ and $c_{\ell 3}$ are considered. Thus, the wavenumbers are $k_{\nu j} = \omega / c_{\nu j}$ and the wavevectors are given by $\mathbf{k}_{\nu j}^{\pm} = k_{\nu j} \left(\sin(\theta_{\nu j})\hat{\mathbf{x}} \pm \cos(\theta_{\nu j})\hat{\mathbf{z}}\right)$ where the $\pm$ sign indicates the propagation direction along the z axis and $\mathbf{r} = \hat{\mathbf{x}} + \hat{\mathbf{z}}$ are unit vectors. An incident sound pressure p_0 impinges on the plate giving rise to the reflected (p_R) and transmitted (p_T) sound pressure, which are characterized using plane waves. In the solid, Stokes-Helmholtz decomposition allows us to describe the sound field in terms of the wave potentials ξ_2 and ψ_2 (see appendix

A.4). The field in the three regions can be written as follows

$$p_1 = p_0 + p_R = e^{i\mathbf{k}_{\ell 1}^{-}\mathbf{r}} + Re^{i\mathbf{k}_{\ell 1}^{+}\mathbf{r}}, \tag{2.11a}$$

$$\xi_2 = \xi_+ + \xi_- = A^+ e^{i\mathbf{k}_{\ell 2}^{+}\mathbf{r}} + A^- e^{i\mathbf{k}_{\ell 2}^{-}\mathbf{r}}, \tag{2.11b}$$

$$\psi_2 = \psi_+ + \psi_- = B^+ e^{i\mathbf{k}_{t2}^{+}\mathbf{r}} + B^- e^{i\mathbf{k}_{t2}^{-}\mathbf{r}}, \tag{2.11c}$$

$$p_3 = p_T = Te^{i\mathbf{k}_{\ell 3}^{-}\mathbf{r}}, \tag{2.11d}$$

where R and T are the reflection and the transmission coefficients respectively and $A^{\pm}$, $B^{\pm}$ the coefficients for the upwards $(+)$ and downwards $(-)$ longitudinal and transverse potentials. The momentum must be conserved in the x direction, i.e. all $k_{\nu j}\sin(\theta_{\nu j})$ are equal and will be denoted simply as Q. Applying continuity of the normal displacement $u_{j,z}$ and stresses σ_2^{zz}, σ_2^{xz} at both interfaces yields

$$u_{1,z} = u_{2,z}, \qquad \sigma_2^{zz} = -p_1, \qquad \sigma_2^{xz} = 0, \qquad \text{at } z = 0\,, \tag{2.12}$$

$$u_{3,z} = u_{2,z}, \qquad \sigma_2^{zz} = -p_3, \qquad \sigma_2^{xz} = 0, \qquad \text{at } z = -h\,. \tag{2.13}$$

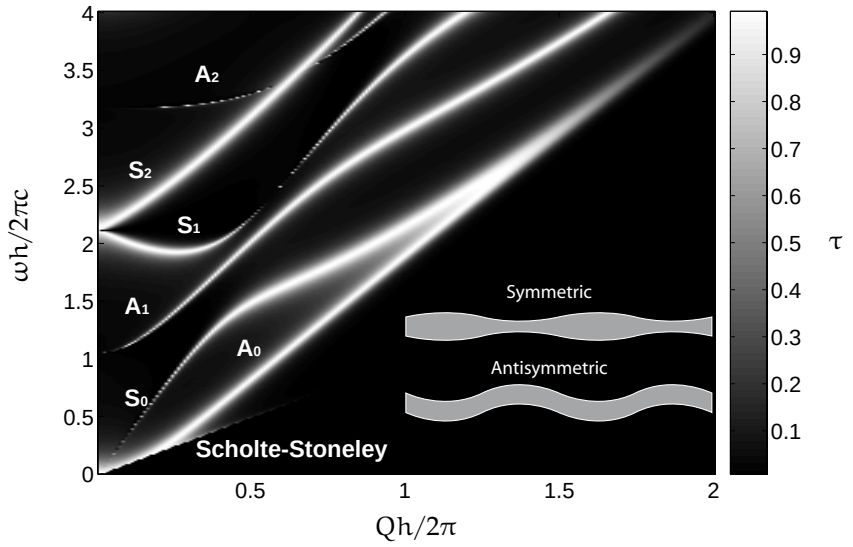

Figure 2.3: Transmitted sound power τ calculations (gray linear scale) for an homogeneous aluminum plate immersed in water as a function of the parallel wavenumber Q and the frequency ω, both of them normalized by the plate thickness value h. The different modes are labeled according to their shape as shown in the inset.

These six equations with six unknowns, namely R, A^+, A^-, B^+, B^-, and T form a linear system that needs to be solved for each $(\theta_{\ell 1}, \omega)$ pair. Explicit forms of the boundary conditions and of the system of equations can be found in the appendix A.4. Performing calculations for an aluminum plate ($\rho_2 = 2700$ kg/m^3, $c_{\ell 2} = 6500$ m/s, $c_{t2} = 3130$ m/s) immersed in water ($\rho_1 = 1000$ kg/m^3, $c_{\ell 1} = 1480$ m/s) the Fig. 2.3 is obtained, where $\tau = |T|^2$.

High transmission values can be observed revealing a complex dispersion in Fig. 2.3. For this case, three kinds of modes can be distinguished [85]: Scholte-Stoneley mode, symmetric leaky Lamb modes, and antisymmetric leaky Lamb modes.

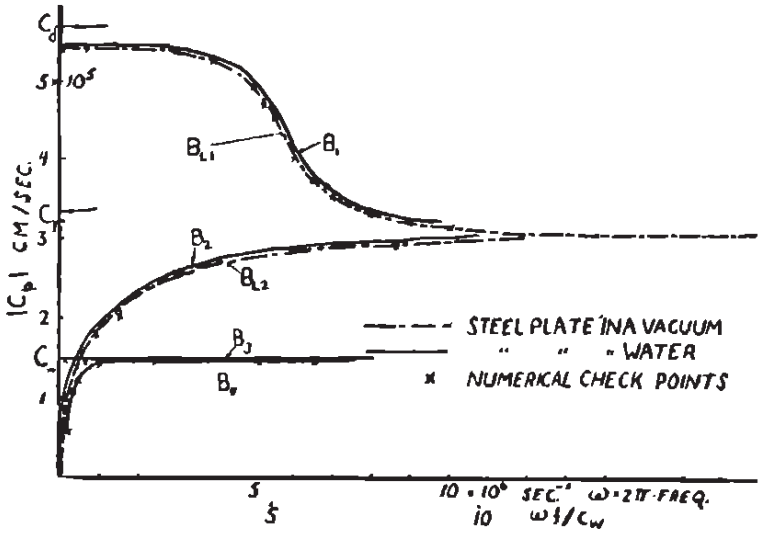

Figure 2.4: Excerpt from [85] showing the phase velocity of Lamb waves for an steel plate immersed in water as a function of the frequency. Top curve corresponds to S_0, middle curve to A_0, and lower curve to the Scholte-Stoneley mode.

The Scholte-Stoneley mode (see Fig. 2.4) propagates across the fluid-solid interface with a phase speed slightly slower than that of the water. At low frequencies, this mode is mixed with the A_0 mode and slowly converges to the sound line as ω increases.

Leaky Lamb modes are guided waves produced due to the multiple reflections of longitudinal and in-plane transverse modes at both plate-fluid interfaces. The inset in Fig. 2.3 shows the different shapes of the symmetric (S_n) and antisymmetric (A_n) modes. The two cutoff-free modes, A_0 and S_0, show different transmission properties. The first one has a broader transmission peak and smaller phase speed than the latter, but both converge at higher frequencies to Rayleigh waves phase speed. The higher order Lamb

modes show many interesting features like negative and zero group velocity (mode S_1), mode splitting (S_1 and S_2), and mode crossing (A_2 and S_2).

To obtain more information concerning the plate displacement, a traveling wave along the x axis can be assumed. Neglecting the incident wave and applying the boundary conditions, the dispersion relation can be obtained [82, 83, 84, 85]. The dispersion equations are quite complex and can be solved only using numerical methods for nonlinear systems. Thus, despite its simplicity, the transmission approach gives access to the leaky dispersion relation. The suitability of the transmission approach depends, however, strongly on the fluid.

Lamb waves are widely used for nondestructive evaluation at ultrasonic frequencies in plate type structures. Internal defects in large plates can be detected by means of Lamb waves. Not only isotropic plates, but also anisotropic or multilayered structures can be inspected. In addition, material characterization can be performed by means of Lamb waves because its propagation enables the extraction of the elastic constants of the plate [86]. Most applications use water-coupled Lamb wave excitation and detection, although some techniques make use of zero group velocity [87] for nondestructive testing of plates in air to increase the fluid-solid coupling.

Modes having negative group velocity are well known for Lamb waves [88] and other mechanical realizations [89]. In words of Horace Lamb [89]:

> "It is hardly to be expected that the notion of a negative group-velocity will have any very important physical application."

However, a recent realization of negative refraction focusing of Lamb waves has been reported [90] using an astonishingly simple approach consisting in nothing but an abrupt change in the plate thickness. Lamb waves are interesting because under fairly simple vibrations, a plethora of exotic phenomena is available without the need of any metamaterial or complicated structure.

The electromagnetic analogy of this phenomenon would be a dielectric plate having high refractive index, however, intrinsic differences separate light and sound in this kind of systems.

2.4 Single hole sound transmission

The problem of the sound transmission through a circular hole has been studied at different levels of detail and using several methods. At the end of the nineteenth century, Rayleigh [91, 92] started to work in this problem in the case of scalar waves (sound and electrons) for null thickness plates. An exact solution to this three-dimensional

diffraction problem was found by Bouwkamp [93] in 1941, who later, in 1954, wrote a review [94] comprising not only scalar, but also vectorial waves (light) for zero thickness screen, summarizing the knowledge of the problem at that moment.

Although the same equation must be satisfied for sound, electrons, and light, namely the Helmholtz wave equation $(\nabla^2+k^2)p = 0$, their different behavior lies in the boundary conditions. The screen needs to be perfectly rigid for sound, to have infinite potentials boundaries for electrons, and to be a perfect conductor for light. Sound and electrons show complementary behavior via Babinet's principle i.e. the diffraction of sound (electrons) by a disc is essentially identical to the diffraction by the complementary aperture for electrons (sound). However, a small hole in a perfect screen is quite permeable for sound while for electrons and light it is nearly opaque.

Concerning sound, for the finite thickness case Nomura and Inawashiro [95] developed an exact solution but difficult to implement. Afterwards, Wilson and Soroka [96] derived an approximated solution for normal incidence showing very good agreement with measurements. However, a more rigorous and exact method relying in modal expansions has been derived in [97]. More recently [98, 99] deal with diffuse field incidence and compare different methods theoretically and experimentally.

Here the modal expansion method described in [97] will be used to show the transmission properties through a circular aperture. A comparison between the flat piston approximation of [96] and the modal expansion method will also be given.

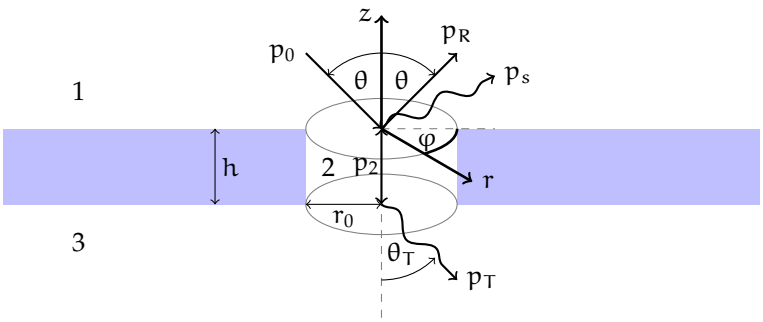

Figure 2.5: Diagram of the sound transmission through a circular hole of radius r_0 in a rigid plate of thickness h. As the sound field does not penetrates into the solid, the same fluid is used in the three regions $j = 1, 2, 3$. Cylindrical coordinates (r, φ, z) are used.

Following the method described in [97], the geometry of the problem is depicted in Fig. 2.5, where cylindrical coordinates are used to take advantage of the hole symmetry. The incident sound pressure p_0 and the specularly reflected sound pressure p_R are plane waves, whereas the backscattered (p_s) and the transmitted (p_T) sound pressure are

described using plane wave expansion. Under the rigid-solid assumption there is no field inside the solid, whereas the field inside the hole p_2 consists of circular eigenmodes in the polar plane together with backward and forward components in the z direction. Thus, the pressure field in the three regions can be written as follows:

$$\begin{aligned} p_1 = \left(e^{ik_0 z} + e^{-ik_0 z}\right) &\sum_{m=-\infty}^{\infty} i^m J_m(Q_0 r) e^{im\varphi} \\ &+ \sum_{m=-\infty}^{\infty} e^{im\varphi} \int_0^{\infty} \beta^+_{Qm} J_m(Qr) e^{iqz} Q \, dQ \,, \end{aligned} \tag{2.14a}$$

$$p_2 = \sum_{m=-\infty}^{\infty} \sum_{n=1}^{\infty} J_m(Q_{mn} r)\, e^{im\varphi}\, \Psi^+_{mn}(z) \,, \tag{2.14b}$$

$$p_3 = p_T = \sum_{m=-\infty}^{\infty} e^{im\varphi} \int_0^{\infty} \beta^-_{Qm} J_m(Qr) e^{-iq(z+h)} Q \, dQ \,, \tag{2.14c}$$

with

$$\Psi^{\pm}_{mn}(z) = \left[\alpha^+_{mn} e^{iq_{mn} z} \pm \alpha^-_{mn} e^{-iq_{mn} z}\right] , \tag{2.15}$$

where $Q_0 = k_0 \sin\theta$, $q_0 = k_0 \cos\theta$, $q = \sqrt{k_0^2 - Q^2}$, $q_{mn} = \sqrt{k_0^2 - Q_{mn}^2}$, and $J_m(x)$ is the Bessel function of the first kind and order m.

Note that $p_1 = p_0 + p_R + p_s$ and for both, incident and reflected plane waves, the Jacobi-Anger expansion is used for the parallel to the plate component (see appendix A.2). At both hole openings, the field must satisfy the continuity of pressure and normal velocity. However, at the solid surface, the normal particle velocity is zero. Therefore, at the hole walls $J'_m(Q_{mn} r_0) = 0$. The boundary conditions at $z = 0, -h$ are given by

$$\partial_z p_1|_{z=0} = \partial_z p_2|_{z=0} \qquad \text{if } r < r_0, \qquad \partial_z p_1|_{z=0} = 0 \qquad \text{if } r > r_0, \tag{2.16}$$

$$\partial_z p_3|_{z=-h} = \partial_z p_2|_{z=-h} \qquad \text{if } r < r_0, \qquad \partial_z p_3|_{z=-h} = 0 \qquad \text{if } r > r_0, \tag{2.17}$$

$$p_1|_{z=0} = p_2|_{z=0} \,, \qquad p_3|_{z=-h} = p_2|_{z=-h} \,, \qquad \text{if } r < r_0 \,. \tag{2.18}$$

Taking advantage of the orthogonality of the Bessel functions (see details in appendix A.2) by applying Hankel transforms in Eqs. (2.16) and (2.17) we get

$$\beta^+_{Qm} = \sum_{n=0}^{\infty} \frac{q_{mn}}{q} \Psi^-_{mn}(0) I(Q_{mn}, Q) \,, \tag{2.19}$$

$$\beta^-_{Qm} = -\sum_{n=0}^{\infty} \frac{q_{mn}}{q} \Psi^-_{mn}(-h) I(Q_{mn}, Q) \,, \tag{2.20}$$

where $I(k, k')$ is defined in Eq. (A.12). Similarly, substituting Eqs. (2.19) and (2.20) into Eq. (2.18), multiplying by $J_m(Q_{mn'} r) r$, and integrating with respect to r from 0 to r_0

yields

$$2i^m I(Q_0, Q_{mn'}) + \sum_{n=0}^{\infty} \Psi^-_{mn}(0)\mathbf{I}^m_{nn'} = \sum_{n=0}^{\infty} \Psi^+_{mn}(0) I(Q_{mn}, Q_{mn'}), \tag{2.21}$$

$$-\sum_{n=0}^{\infty} \Psi^-_{mn}(-h)\mathbf{I}^m_{nn'} = \sum_{n=0}^{\infty} \Psi^+_{mn}(-h) I(Q_{mn}, Q_{mn'}), \tag{2.22}$$

where $\mathbf{I}^m_{nn'}$ is an integral (see Eq. (A.14)) with respect to Q, which has to be calculated numerically. Truncating the sums in Eqs. (2.21) and (2.22) over n, n', and m up to N, N, and M respectively, a linear system of size $2(M+N) \times 2(M+N)$ involving $\alpha^{\pm}_{mn}$ is obtained. In matrix form it gives $\boldsymbol{\Lambda}\,\boldsymbol{\alpha} = \boldsymbol{\beta}$, where

$$\boldsymbol{\Lambda} = \begin{bmatrix} I(Q_{mn}, Q_{mn'}) - \mathbf{I}^m_{nn'} & I(Q_{mn}, Q_{mn'}) + \mathbf{I}^m_{nn'} \\ [I(Q_{mn}, Q_{mn'}) + \mathbf{I}^m_{nn'}]\, e^{-iq_{mn}h} & [I(Q_{mn}, Q_{mn'}) - \mathbf{I}^m_{nn'}]\, e^{iq_{mn}h} \end{bmatrix}, \tag{2.23}$$

$$\boldsymbol{\alpha} = \begin{bmatrix} \alpha^+_{mn} \\ \\ \alpha^-_{mn} \end{bmatrix}, \qquad \boldsymbol{\beta} = \begin{bmatrix} 2i^m I(Q_0, Q_{mn'}) \\ \\ 0 \end{bmatrix}. \tag{2.24}$$

However, β^-_{Qm} needs to be calculated from Eq. (2.20) to eventually evaluate the integral in Eq. (2.14c). In order to get the farfield and overcome the complexity of this integral, the stationary phase approximation [100] is used. The details for this particular case are given in appendix A.3. The final expression after applying the approximation is

$$p_3 \approx \Phi_3 = iq_T\, e^{-iq_T h}\, \frac{e^{-ik_0 R}}{R} \sum_m i^m \beta^-_{Q_T m}\, e^{im\varphi}, \tag{2.25}$$

where $r = R\sin\theta_T$, $z = R\cos\theta_T$, $Q_T = k_0 \sin\theta_T$, and $q_T = k_0\cos\theta_T$ due to the change to spherical coordinates.

Then, the transmitted sound power can be calculated as follows

$$\tau = \frac{\Pi_T(\omega, \theta)}{\Pi_0(\omega, \theta)}, \tag{2.26}$$

$$\Pi_0(\omega, \theta) = \frac{1}{2}\mathcal{R}e\left\{\int_0^{2\pi}\int_0^{r_0} p_0 \left(\frac{i\partial_z p_0}{\omega\rho}\right)^* r\, dr\, d\varphi\right\} = \frac{\pi r_0^2 \cos\theta}{2\rho c}, \tag{2.27}$$

where $()^*$ means complex conjugate and $\mathcal{R}e\{\}$ the real part. The expression (2.27) correspond to the time averaged intensity of the incident wave integrated through the aperture area. The radiated sound power can be calculated either following [97] as

$$\Pi_T(\omega, \theta) = \frac{1}{2}\mathcal{R}e\left\{\int_0^{2\pi}\int_0^{r_0} p_2|_{z=-h} \left(\frac{i\partial_z p_2|_{z=-h}}{\omega\rho}\right)^* r\, dr\, d\varphi\right\}, \tag{2.28}$$

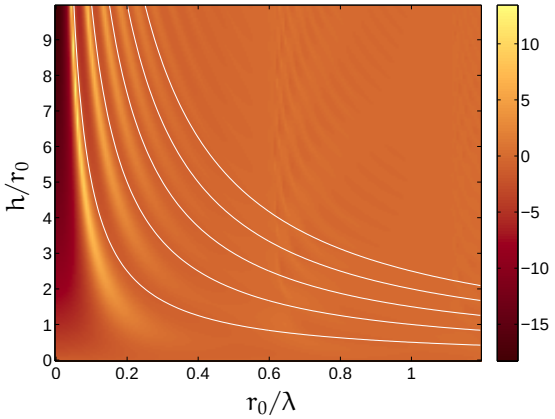

Figure 2.6: Transmitted sound power (color scale) $\tau/\pi r_0^2$ in (dB) through a circular hole as a function of r_0/λ and h/r_0 for normal incidence. The white dashed curves correspond to the $h = n\lambda/2$ FPR condition for an open tube.

or using the farfield pressure Φ_3 and performing numerical integration with respect to θ_T and φ_T as

$$\Pi_T(\omega,\theta) = \frac{1}{2\rho c}\int_0^{\pi/2}\int_0^{2\pi} |\Phi_3|^2 R^2 \sin(\theta_T)\, d\varphi_T\, d\theta_T\,. \tag{2.29}$$

Although numerical integration is involved, the last alternative has been chosen due to its simplicity. Under normal incidence only the $m = 0$ components contribute to the transmission. Thus, the integrand in Eq. (2.29) yields $q_T^2\,|\beta^-_{Q_T 0}|^2 \sin\theta_T$.

The results of this model under normal incidence are plotted in Fig. 2.6 for different h/r_0 proportions as function of r_0/λ. Looking carefully at the results of Fig. 2.6 one can see several high transmission peaks whose highest level increases as the h/r_0 ratio increases overcoming the full transmission level at 0 dB. This behavior is well known and was verified experimentally already in 1965 by Wilson and Soroka [96]. Not only the peak level but also the number of peaks increases with the h/r_0 ratio and penetrate deeper in the subwavelength area even for $r_0/\lambda < 0.2$. This behavior can be explained as due to the resonance that takes place into the hole along its length h. Following the nomenclature from optics, we are dealing with FPR, which in its simplest form for an open tube satisfies the condition $h = n\lambda/2$ ($n \in \mathbb{N}$), which is shown as white curves in Fig. 2.6. As the thickness increases, more resonances are found in the transmission spectrum. The resonances are always at larger wavelengths than those predicted by the open tube resonances. This discrepancy is usually corrected by means of an equivalent thickness or end correction [101]. When $h = 0$ the transmission converges to $8/\pi^2$ for very large wavelengths [93].

Figure 2.7 shows the comparison between the approximation of Wilson and Soroka [96] and the model derived here for normal incidence. For the three different h/r_0 ratios the agreement is excellent when $r_0/\lambda < 0.5$ and the differences for $r_0/\lambda > 0.5$ can be explained as due to the lack of the higher order circular modes in the approximation

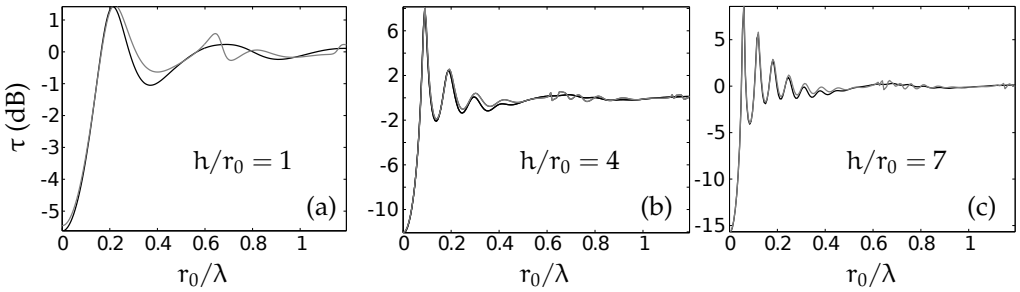

Figure 2.7: Comparison between the approximation of Wilson and Soroka [96] (black) and the model described here (gray) for three different h/r_0 values.

that assumes planar piston behavior at the hole openings. Therefore, the modal model method has been chosen because it provides an exact solution for a larger range of frequencies than the planar piston approximation.

3

Theory of periodically perforated plates

In the following pages will be presented the derivation of the different theoretical models developed to understand the experimental results and also to predict some interesting phenomena. First, some notation and geometrical facts regarding two-dimensional arrays will be given. Afterwards, the rigid-solid theory and the full elasto-acoustic theory are derived. Finally, the details of the finite element method calculations are given.

3.1 Geometry of two dimensional periodic structures

Holes drilled in a plate in a periodical manner form two-dimensional structures. To characterize two-dimensional periodic structures, some ideas and nomenclature from solid-state physics [102, 103] will be taken. Solid-state physics includes the study ordered structures at atomic scales. Because of that, some geometrical results obtained at that tiny scale are also useful for this study.

The key parameters to describe the arrays of holes are the radius of the hole r_0 and the distance a between them as shows Fig. 3.1. In addition, to characterize the plate we need the thickness h.

A more global parameter that involves not only the hole size, but also the array period is the filling fraction of holes f, which is defined as the ratio between the hole area and the unit cell area. Then, the filling fraction of holes of the square lattice is $f_\square = \pi r_0^2/a^2$ and in the case of the triangular lattice is $f_\triangle = 2\pi r_0^2/\sqrt{3}a^2$. Figure 3.2 shows

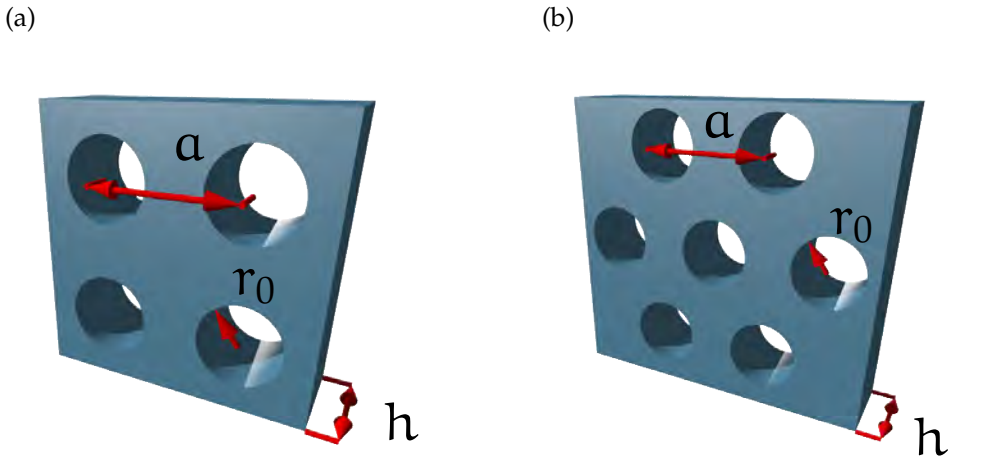

Figure 3.1: Diagram of the geometrical parameters of the PPP where r_0 is the hole radius, a the array periodicity, and h the plate thickness for (a) square and (b) triangular lattices.

the filling fraction of holes for both lattices depending on the geometrical proportions $2r_0/a = d/a$ and h/a of the perforated plate. This geometrical parameter space is very useful in the study of the transmission characteristics of the plate as it helps to retain a global picture of the phenomena. The main difference between both parameter spaces is the fact that $f_{\triangle}max > f_{\square}max$ as can be clearly seen in Fig. 3.2 comparing both colors at $d/a = 1$.

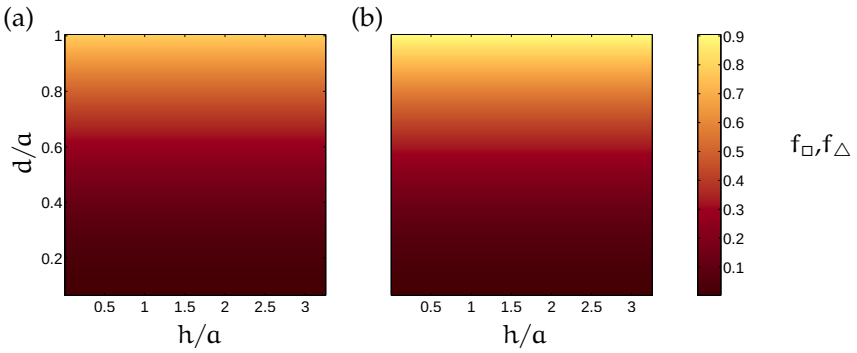

Figure 3.2: Parameter spaces of the PPP for (a) square and (b) triangular lattices. $d = 2r_0$ is the hole diameter, a the array periodicity, and h the plate thickness. The color scale corresponds to the filling fraction of holes.

The position of every hole can be written as $\mathbf{r_n} = n_1\mathbf{a}_1 + n_2\mathbf{a}_2$ where $\mathbf{a}_i$ are called

primitive cell vectors and n_i are integers. For the square lattice we get

$$\mathbf{a}_1 = a\hat{\mathbf{x}}\,, \qquad \mathbf{a}_2 = a\hat{\mathbf{y}}\,, \tag{3.1}$$

whereas for the triangular lattice yields

$$\mathbf{a}_1 = \frac{a}{2}(\hat{\mathbf{x}} + \sqrt{3}\,\hat{\mathbf{y}})\,, \qquad \mathbf{a}_2 = \frac{a}{2}(\hat{\mathbf{x}} - \sqrt{3}\,\hat{\mathbf{y}})\,. \tag{3.2}$$

The area S of the unit cell is $S = a^2$ for the square lattice and $S = \sqrt{3}a^2/4$ for the triangular lattice. The whole array can be seen as infinite series of periodically distributed Dirac-delta functions

$$\Delta(\mathbf{r_n}) = \sum_{\mathbf{n}=-\infty}^{\infty} \delta(\mathbf{r} - \mathbf{r_n})\,, \tag{3.3}$$

whose Fourier transform

$$\mathcal{F}_x\mathcal{F}_y\{\Delta(\mathbf{r_n})\} = \frac{4\pi^2}{S} \sum_{\mathbf{m}=-\infty}^{\infty} \delta(\mathbf{k} - \mathbf{G})\,, \tag{3.4}$$

is also an infinite set of periodically distributed delta functions but in the reciprocal space instead of the real space ($\mathcal{F}_x\{\}$ and $\mathcal{F}_y\{\}$ denotes the Fourier transform in x and y respectively). This gives rise to the reciprocal lattice where

$$\mathbf{G} = m_1\mathbf{b}_1 + m_2\mathbf{b}_2 \tag{3.5}$$

denotes the reciprocal lattice vector where $\mathbf{b}_i$ are the primitive vectors of the reciprocal lattice and the integers m_i are called Miller indices. For the square array we have

$$\mathbf{b}_1 = \frac{2\pi}{a}\hat{\mathbf{x}}\,, \quad \mathbf{b}_2 = \frac{2\pi}{a}\hat{\mathbf{y}}\,, \tag{3.6}$$

and for the triangular array

$$\mathbf{b}_1 = \frac{2\pi}{a}(\hat{\mathbf{x}} + \frac{\hat{\mathbf{y}}}{\sqrt{3}})\,, \quad \mathbf{b}_2 = \frac{2\pi}{a}(\hat{\mathbf{x}} - \frac{\hat{\mathbf{y}}}{\sqrt{3}})\,. \tag{3.7}$$

Due to this periodicity in the reciprocal space some physical quantities can be redundant if they are studied along a large area. To avoid this redundancy the analysis is performed inside the first Brillouin zone [6] which is depicted in Fig. 3.3 (a) for the square lattice and in Fig. 3.3 (b) for the triangular lattice. Moreover, as the Brillouin zone is symmetric, one can restrict further the region of study to the irreducible Brillouin zone, showed in dark blue in Fig. 3.3.

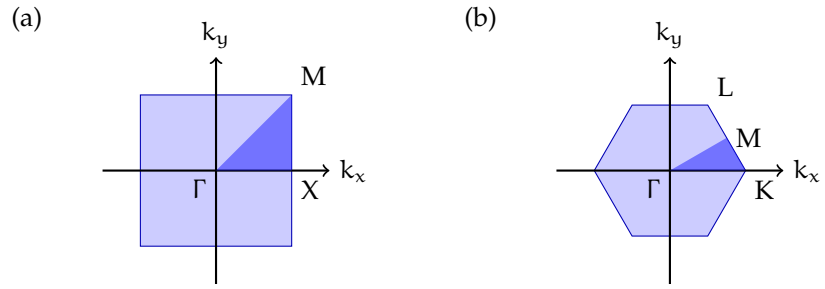

Figure 3.3: Diagram of the first Brillouin zone in the reciprocal space for a) square and b) triangular lattices. Irreducible Brillouin zone is depicted in dark blue.

3.2 Rigid-solid theory

In a similar manner to the case of a single hole, the sound transmission through periodically distributed holes can be studied under the rigid-solid assumption taking advantage of the periodicity of the apertures. The problem also started with Rayleigh's work, who in the second edition (1896) of his book "The Theory of Sound" [37] includes the problem of plane wave scattering on a periodic surface using a rigorous approach called then Rayleigh's hypothesis. Later [104] he extended his study to electromagnetic waves trying to explain the Wood anomaly [38]. In words of Wood [105]:

> "Lord Rayleigh showed that, in the case of sound waves passing, at normal incidence, through very narrow parallel slits, the passage of energy through any slit might be prevented by the cooperative action of the other slits, under the condition that the distance between the slits was an integral multiple of the wave-length"

Nearly a century after, this result was also found by Norris and Luo [39] dealing with a two-dimensional semi-infinite perforated rigid solid. The same method used by Norris was further completed to the case of a two-dimensional periodically perforated slab by Zhou and Kriegsman [47] ten years after Norris. They found complete transmission through narrow holes using only the cutoff-free mode inside the hole. Very recently, several groups have also found similar full transmission peaks in PPPs [48, 49, 51].

To calculate the sound transmission, the Rayleigh's hypothesis is used, extending Takakura's model [26] for light in a slit array. The validity of this hypothesis for gratings remained under discussion until now [106] for the electromagnetic case. The diagram with the description of the geometry is shown in Fig. 3.4. An incident plane pressure wave p_0 impinges in the perforated plate. The reflected pressure field p_R is plane-wave

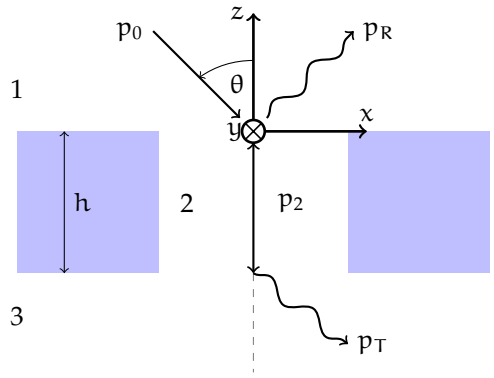

Figure 3.4: Diagram of the unit-cell cross-section of the periodically perforated plate. Due to the circular symmetry of the holes also polar coordinates (r, φ) are used together with the cartesian coordinates. Dimensions of the holes and plate have been defined in Fig. 3.1. The sound field is divided into three fluid regions $j = 1, 2, 3$.

expanded, as well as the transmitted sound pressure p_T. The pressure field inside the cavity is described by guided waves in the same manner than the single hole case (see Eq. (2.14b)).

Splitting the space in three regions we can write the pressure field as

$$p_1 = e^{i(\mathbf{Q}_0 \mathbf{r}_\parallel - q_0 z)} + \iint_{-\infty}^{\infty} \beta^+(\mathbf{Q})\, e^{i(\mathbf{Q} \mathbf{r}_\parallel + q z)} d^2\mathbf{Q}\,, \tag{3.8a}$$

$$p_2 = \sum_{m=-\infty}^{\infty} \sum_{n=1}^{\infty} J_m(Q_{mn} r)\, e^{im\varphi}\, \Psi^+_{mn}(z)\,, \tag{3.8b}$$

$$p_3 = \iint_{-\infty}^{\infty} \beta^-(\mathbf{Q})\, e^{i(\mathbf{Q} \mathbf{r}_\parallel - q(z+h))} d^2\mathbf{Q}\,, \tag{3.8c}$$

with

$$\Psi^\pm_{mn}(z) = \left[\alpha^+_{mn} e^{iq_{mn}(z+h)} \pm \alpha^-_{mn} e^{-iq_{mn} z} \right], \tag{3.9}$$

where $\mathbf{k}_0 = (\mathbf{Q}_0, q_0)$, $\mathbf{r}_\parallel = (x, y) = (r, \varphi)$, $q = \sqrt{\mathbf{k}_0^2 - \mathbf{Q}^2}$, $q_{mn} = \sqrt{\mathbf{k}_0^2 - Q_{mn}^2}$, and $\beta^+(\mathbf{Q})$, $\beta^-(\mathbf{Q})$ are the coupling coefficients between the holes and the semi-infinite space. As the sound does not penetrates into the solid the polar eigenfunctions inside the hole must satisfy $J'_m(Q_{mn} r_0) = 0$, which is equivalent to assume zero normal velocity at the hole walls.

Due to the plane wave expansion, $\beta^\pm(\mathbf{Q})$ are related to the particle velocity at both sides of the plate. As the particle velocity is then periodic and based on the Rayleigh hypothesis one can perform Fourier series expansion on either side of the film yielding

$$\beta^+(\mathbf{Q}) = \delta(\mathbf{Q} - \mathbf{Q}_0) + \sum_{\mathbf{G}} \beta^+_{\mathbf{G}}\, \delta(\mathbf{Q} - \mathbf{Q}_{\mathbf{G}})\,, \tag{3.10}$$

$$\beta^-(\mathbf{Q}) = \sum_{\mathbf{G}} \beta^-_{\mathbf{G}}\, \delta(\mathbf{Q} - \mathbf{Q}_{\mathbf{G}})\,, \tag{3.11}$$

where $\mathbf{Q_G} = \mathbf{Q}_0 + \mathbf{G}$, and $\mathbf{G}$ is the reciprocal lattice vector defined in Eq. (3.5). Thus Eqs. (3.8a) and (3.8c) can be rewritten as

$$p_1 = 2e^{i\mathbf{Q}_0 \mathbf{r}_\parallel} \cos(q_0 z) + \sum_{\mathbf{G}} \beta_{\mathbf{G}}^+ e^{i(\mathbf{Q_G} \mathbf{r}_\parallel + q_G z)}\,, \tag{3.12}$$

$$p_3 = \sum_{\mathbf{G}} \beta_{\mathbf{G}}^- e^{i(\mathbf{Q_G} \mathbf{r}_\parallel - q_G (z+h))}\,. \tag{3.13}$$

Imposing the continuity of the particle velocity at both hole openings, multiplying by $e^{-i\mathbf{Q_G} \mathbf{r}_\parallel}$ and integrating along a unit cell yields

$$\beta_{\mathbf{G}}^+ = \frac{1}{S} \sum_{mn} \frac{q_{mn}}{q_G} \Psi_{mn}^-(0) I_n^m(\mathbf{Q_G})\,, \tag{3.14}$$

$$\beta_{\mathbf{G}}^- = -\frac{1}{S} \sum_{mn} \frac{q_{mn}}{q_G} \Psi_{mn}^-(-h) I_n^m(\mathbf{Q_G})\,, \tag{3.15}$$

where S refers to the unit-cell area and the term $I_n^m(\mathbf{Q_G})$ corresponds to the the following integral

$$I_n^m(\mathbf{Q_G}) = \int_0^{2\pi} \int_0^{r_0} J_m(Q_{mn} r) e^{im\varphi} e^{-i\mathbf{Q_G} \mathbf{r}_\parallel}\, r\, dr\, d\varphi =$$

$$2\pi i^{-m} e^{im\varphi_G} \begin{cases} \dfrac{|\mathbf{Q_G}| r_0}{|\mathbf{Q_G}|^2 - Q_{mn}^2} J_m(Q_{mn} r_0) J_m'(|\mathbf{Q_G}| r_0) & \text{if } Q_{mn} \neq |\mathbf{Q_G}|\,, \\ \dfrac{r_0^2}{2} J_m^2(Q_{mn} r_0) \left[1 - \dfrac{m^2}{(Q_{mn} r_0)^2}\right] & \text{if } Q_{mn} = |\mathbf{Q_G}|\,, \end{cases} \tag{3.16}$$

where $\varphi_G = \arcsin(\mathbf{Q_{G_y}} / \mathbf{Q_{G_x}})$. The continuity of the sound pressure at the hole openings requires

$$2e^{i\mathbf{Q}_0 \mathbf{r}_\parallel} + \sum_{\mathbf{G}} \beta_{\mathbf{G}}^+ e^{i\mathbf{Q_G} \mathbf{r}_\parallel} = \sum_{mn} J_m(Q_{mn} r)\, e^{im\varphi}\, \Psi_{mn}^+(0)\,, \tag{3.17}$$

$$\sum_{\mathbf{G}} \beta_{\mathbf{G}}^- e^{i\mathbf{Q_G} \mathbf{r}_\parallel} = \sum_{mn} J_m(Q_{mn} r)\, e^{im\varphi}\, \Psi_{mn}^+(-h)\,. \tag{3.18}$$

Substituting Eqs. (3.14) and (3.15) into Eqs. (3.17) and (3.18) respectively, then multiplying by $r J_m(Q_{mn'} r) e^{-im'\varphi}$ and integrating over the hole area yields

$$2\left(I_{n'}^{m'}(\mathbf{Q}_0)\right)^* + \frac{1}{S} \sum_{mn} q_{mn} \Psi_{mn}^-(0) \sum_{\mathbf{G}} \frac{I_n^m(\mathbf{Q_G}) \left(I_{n'}^{m'}(\mathbf{Q_G})\right)^*}{q_G} = \delta_{mm'} \Psi_{mn}^+(0) I(Q_{mn}, Q_{mn'})\,, \tag{3.19}$$

$$-\frac{1}{S} \sum_{mn} q_{mn} \Psi_{mn}^-(-h) \sum_{\mathbf{G}} \frac{I_n^m(\mathbf{Q_G}) \left(I_{n'}^{m'}(\mathbf{Q_G})\right)^*}{q_G} = \delta_{mm'} \Psi_{mn}^+(-h) I(Q_{mn}, Q_{mn'})\,. \tag{3.20}$$

A set of linear equations involving only $\alpha^{\pm}_{mn}$ is then obtained truncating the sums for a finite number of hole modes and reciprocal lattice vectors. In matrix form, Eqs. (3.19) and (3.20) can be written as

$$\begin{bmatrix} \mathbf{D}_{11} & \mathbf{D}_{12} \\ \mathbf{D}_{21} & \mathbf{D}_{22} \end{bmatrix} \begin{bmatrix} \alpha^{+}_{mn} \\ \alpha^{-}_{mn} \end{bmatrix} = \begin{bmatrix} 2\left(I^{m'}_{n'}(\mathbf{Q}_0)\right)^* \\ 0 \end{bmatrix}, \tag{3.21}$$

where

$$\mathbf{D}_{11} = \left[\delta_{mm'} I(Q_{mn}, Q_{mn'}) - \frac{1}{S} q_{mn} \mathbf{M}^{mm'}_{nn'}(\mathbf{Q_G})\right] e^{iq_{mn}h}, \tag{3.22}$$

$$\mathbf{D}_{12} = \delta_{mm'} I(Q_{mn}, Q_{mn'}) + \frac{1}{S} q_{mn} \mathbf{M}^{mm'}_{nn'}(\mathbf{Q_G}), \tag{3.23}$$

$$\mathbf{D}_{21} = \delta_{mm'} I(Q_{mn}, Q_{mn'}) + \frac{1}{S} q_{mn} \mathbf{M}^{mm'}_{nn'}(\mathbf{Q_G}), \tag{3.24}$$

$$\mathbf{D}_{22} = \left[\delta_{mm'} I(Q_{mn}, Q_{mn'}) - \frac{1}{S} q_{mn} \mathbf{M}^{mm'}_{nn'}(\mathbf{Q_G})\right] e^{iq_{mn}h}, \tag{3.25}$$

and

$$\mathbf{M}^{mm'}_{nn'}(\mathbf{Q_G}) = \sum_{\mathbf{G}} \frac{I^{m}_{n}(\mathbf{Q_G})\left(I^{m'}_{n'}(\mathbf{Q_G})\right)^*}{q_{\mathbf{G}}}. \tag{3.26}$$

At this point, we calculated the $\alpha^{\pm}_{mn}$ coefficients and the $\beta^{\pm}_{\mathbf{G}}$ coefficients can be easily obtained evaluating back Eqs. (3.14) and (3.15).

As the perforated plate is assumed to have an infinite extension in the $\mathbf{r}_{\parallel}$ plane, the radiated sound power [100] is given by

$$\Pi(\omega) = \frac{\rho c k_0}{8\pi^2} \mathcal{R}e\left\{\iint_{-\infty}^{\infty} \frac{|V(\mathbf{Q})|^2}{\sqrt{k_0^2 - \mathbf{Q}^2}} \, d^2\mathbf{Q}\right\}, \qquad V(\mathbf{Q}) = \mathcal{F}_x \mathcal{F}_y \left\{\frac{i\partial_z p}{\omega\rho}|_{z=0,-h}\right\}, \tag{3.27}$$

which applied to the incident and radiated sound power yields

$$\tau = \frac{\Pi_T(\omega)}{\Pi_0(\omega, \theta, \varphi)} = \sum_{\mathbf{G}} \mathcal{R}e\left\{\frac{q_{\mathbf{G}}}{q_0}\right\} |\beta^{-}_{\mathbf{G}}|^2. \tag{3.28}$$

The converged numerical results presented here are obtained considering 100 evanescent diffraction orders and 11 holes modes. In addition, a reduced version of this model for the study of slit arrays has been also developed and used to test the convergence of the finite element approximation in the rigid-solid limit. Further extensions of this model implemented to deal with compound hole arrays can be found in [62].

3.3 Full elasto-acoustic theory

The beginning of the research in the field of phononic crystals and metamaterials was devoted to the understanding of bulk wave phenomena. It was after the seminal paper of Sainidou et al. [107] on a mono layer of solids spheres embedded in a polyester slab that Lamb waves became a target for phononic and metamaterials research.

In other context, Maysenhölder [108, 109] theoretically studied the transmission behavior of inhomogeneous walls. These models are devised to deal with airborne sound insulation problems. In fact, it is predicted [108] the appearance of a high Transmission Loss (TL) spike followed by full transmission peak.

The first theoretical works on PhPs [70, 110, 111, 71] predicted the existence of band-gaps in solid-solid PhPs. Zhang et al. [73] comes up with the first experimental evidence of Lamb gaps for air-aluminum and air-brass two-dimensional PhPs. This work was followed by more experimental [74, 75] and theoretical studies [112, 113, 114, 72] centered in band-gap and waveguiding phenomena. After that, different geometrical arrangements and materials have been thoroughly studied. Within the different geometrical possibilities for controlling Lamb waves one can find thin solid-solid phononic film on a plate [115], stubs on thin plates forming phononic structures [116, 117, 118] including locally resonant stubs [119, 120], air-solid PhPs with a membrane [121], air-solid PhP strips [122], and Lamb wave resonators with PhP reflectors [123].

On the other hand, not only plates made of conventional isotropic or anisotropic solids have been subject of research, but also piezoelectric [124] and ferroelectric [125] materials including temperature variation issues of the latter [126].

For applications in the high MHz range, i.e. at small scales for Microelectromechanical systems (MEMS), most practical realizations need a substrate to be implemented. The effect of a solid substrate on the PhP is considered for band-gap formation and waveguiding in [124, 127, 128, 129, 130, 131, 132, 133].

Recent developments comprise negative refraction of shear horizontal (SH) waves [77], Lamb wave band gap optimization [134], and Lamb wave focusing using gradient index PhPs [135].

In addition, in the thin plate limit, flexural waves can also show interesting phenomena such as band gaps due to locally resonant inclusions [136] and negative refraction focusing effects [137, 138, 76].

While most of the aforementioned works only take into account in-plate elastic vibrations, this study additionally brings into focus the coupling of the surrounding fluid to the PhP, which is of crucial importance when considering sound transmission through PhPs.

If the sound penetrates into the plate, which is periodically perforated, one has to consider the elastic movement of the plate coupled with the surrounding fluid not only at the plate free surface but also inside the apertures. This case is more complex than those explained before because one has to deal with the following processes: a) solid-fluid coupling, b) hole scattering, and c) the interference between waves scattered at the periodic distribution of holes. The method used will be first briefly summarized, concisely derived, and finally some results will be discussed. For more information concerning elastic wave propagation in homogeneous medium see appendix A.1.

The method of solution involves the following steps:

- The displacement field **u**, the plate density ρ, and the Lamé coefficients λ, μ, are Fourier-expanded along directions parallel to the periodic plate.

- The eigenstates of a two-dimensional crystal formed by infinitely-long holes with the same periodicity as the plate are obtained when solving the inhomogeneous elastic wave equation (see Eq. (A.1)) leading to a quadratic eigenvalue problem.

- Rayleigh expansions are used for the pressure in the water outside the plate, whereas the displacement field inside the plate is expanded in terms of its eigenstates calculated previously from the inhomogeneous elastic wave equation.

- The continuity of the displacement and the stress in the plate boundaries leads to a set of linear equations that are solved to yield the coefficients of these expansions. This method of solution gives a rigorous expansion for finite plates, in which the thickness enters through the boundary conditions matching the internal two-dimensional modes to the Rayleigh expansions outside the film.

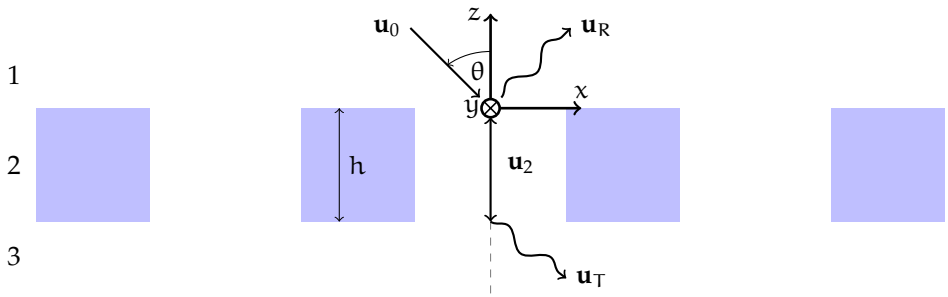

Figure 3.5: Diagram of the coordinate system to be used with the FEAM theory. The sound field is divided into three regions: 1 and 3 correspond to semi-infinite fluids and 2 being a solid plate with a two-dimensional array of holes.

To model the perforated plate, the Plane Wave Expansion (PWE) for a two-dimensional array of cylinders in solid host is used in a similar way to [139] for a given frequency and parallel wavevector. Therefore, one needs to solve the inhomogeneous elastic wave equation for harmonic displacement given by

$$[\partial_j(\lambda\partial_n u_n) + \partial_n\left(\mu(\partial_n u_j + \partial_j u_n)\right)] + \rho\omega^2 u_j = 0\,, \tag{3.29}$$

with j and n running over the cartesian coordinates (x, y, z) and $\mathbf{u} = (u_x, u_y, u_z)$ being the displacement vector. The elastic properties of the solid are given by the density ρ and the Lamé coefficients λ, μ, which in this case depend on $\mathbf{r}_\parallel$ in a periodic manner. Using the periodicity we can expand ρ_2, λ_2, and μ_2 in Fourier series as

$$g(\mathbf{r}_\parallel) = \sum_{\mathbf{G}} g_{\mathbf{G}}\, e^{i\mathbf{G}\mathbf{r}_\parallel}\,, \tag{3.30}$$

where the Fourier coefficients $g_{\mathbf{G}}$ for a square array of cylinders are calculated as

$$g_{\mathbf{G}} = \big(g_B + f_\square(g_A - g_B)\big)\delta_{\mathbf{G}0} + (g_A - g_B)\frac{2\pi r}{GS}J_1(Gr)\,, \tag{3.31}$$

where $G = |\mathbf{G}|$ and the subscripts A and B refers to the properties of the host and inclusion homogeneous material respectively. The displacement can be expanded using the Bloch theorem [102] as

$$\mathbf{u} = \sum_{\mathbf{G},j}\left[u_{\mathbf{G}j}e^{iqz}\right]e^{i\mathbf{Q}_\mathbf{G}\mathbf{r}_\parallel} = \sum_{\mathbf{G},j} u_{\mathbf{G}j}(z)\,e^{i\mathbf{Q}_\mathbf{G}\mathbf{r}_\parallel}\,, \tag{3.32}$$

where $\mathbf{Q}_\mathbf{G} = \mathbf{Q}_0 + \mathbf{G}$ and the subscript j runs over the cartesian coordinates. Replacing the before defined expansions in the Eq. (3.29), multiplying by $e^{-i\mathbf{Q}_{\mathbf{G}'}\mathbf{r}_\parallel}$, and integrating along the unit cell yields

$$\sum_{\mathbf{G}'} A^j_{\mathbf{G}\mathbf{G}'}\,\partial_z^2 u_{\mathbf{G}'j}(z) + \sum_{\mathbf{G}'j'} B^{jj'}_{\mathbf{G}\mathbf{G}'}\,\partial_z u_{\mathbf{G}'j'}(z) + \sum_{\mathbf{G}'j'} C^{jj'}_{\mathbf{G}\mathbf{G}'}\,u_{\mathbf{G}'j'}(z) = 0\,. \tag{3.33}$$

Truncating the sums over $\mathbf{G}$, $\mathbf{G}'$ we get the following quadratic eigenvalue problem

$$\begin{bmatrix} C^{xx}_{\mathbf{G}\mathbf{G}'} - q^2A^x_{\mathbf{G}\mathbf{G}'} & C^{xy}_{\mathbf{G}\mathbf{G}'} & -qB^{xz}_{\mathbf{G}\mathbf{G}'} \\ C^{yx}_{\mathbf{G}\mathbf{G}'} & C^{yy}_{\mathbf{G}\mathbf{G}'} - q^2A^y_{\mathbf{G}\mathbf{G}'} & -qB^{yz}_{\mathbf{G}\mathbf{G}'} \\ -qB^{zx}_{\mathbf{G}\mathbf{G}'} & -qB^{zy}_{\mathbf{G}\mathbf{G}'} & C^{zz}_{\mathbf{G}\mathbf{G}'} - q^2A^z_{\mathbf{G}\mathbf{G}'} \end{bmatrix}\begin{bmatrix} u_{\mathbf{G}'x} \\ u_{\mathbf{G}'y} \\ u_{\mathbf{G}'z} \end{bmatrix} = 0\,, \tag{3.34}$$

where

$$A^x_{\mathbf{G}\mathbf{G}'} = \mu_{\mathbf{G}-\mathbf{G}'}\,, \qquad A^y_{\mathbf{G}\mathbf{G}'} = \mu_{\mathbf{G}-\mathbf{G}'}\,, \qquad A^z_{\mathbf{G}\mathbf{G}'} = \lambda_{\mathbf{G}-\mathbf{G}'} + 2\mu_{\mathbf{G}-\mathbf{G}'}\,, \tag{3.35}$$

$$B^{xz}_{GG'} = Q_{Gx}\lambda_{G-G'} + Q_{G'x}\mu_{G-G'}\,, \qquad B^{yz}_{GG'} = Q_{Gy}\lambda_{G-G'} + Q_{G'y}\mu_{G-G'}\,, \tag{3.36}$$

$$B^{zx}_{GG'} = Q_{G'x}\lambda_{G-G'} + Q_{Gx}\mu_{G-G'}\,, \qquad B^{zy}_{GG'} = Q_{G'y}\lambda_{G-G'} + Q_{Gy}\mu_{G-G'}\,, \tag{3.37}$$

$$C^{xx}_{GG'} = \omega^2\rho_{G-G'} - Q_{Gx}Q_{G'x}\left(\lambda_{G-G'} + 2\mu_{G-G'}\right) - Q_{Gy}Q_{G'y}\mu_{G-G'}\,, \tag{3.38}$$

$$C^{xy}_{GG'} = -Q_{Gx}Q_{G'y}\lambda_{G-G'} - Q_{Gy}Q_{G'x}\mu_{G-G'}\,, \tag{3.39}$$

$$C^{yx}_{GG'} = -Q_{Gy}Q_{G'x}\lambda_{G-G'} - Q_{Gx}Q_{G'y}\mu_{G-G'}\,, \tag{3.40}$$

$$C^{yy}_{GG'} = \omega^2\rho_{G-G'} - Q_{Gy}Q_{G'y}\left(\lambda_{G-G'} + 2\mu_{G-G'}\right) - Q_{Gx}Q_{G'x}\mu_{G-G'}\,, \tag{3.41}$$

$$C^{zz}_{GG'} = \omega^2\rho_{G-G'} - \left(Q_{Gx}Q_{G'x} + Q_{Gy}Q_{G'y}\right)\mu_{G-G'}\,. \tag{3.42}$$

This system has been solved using standard numerical routines [1] and gives us the eigenvalues q_n and the eigenvectors $u^{\pm}_{Gn}$. Then, the n-eigensolution can be expressed as

$$\mathbf{u}_n = \sum_{\mathbf{G}} \mathbf{u}_{Gn}\, e^{i\mathbf{Q}_G\mathbf{r}_\parallel + iq_n z}\,. \tag{3.43}$$

At this point, the Rayleigh expansion can be performed as before by splitting the space in three regions and writing the displacement as

$$\mathbf{u}_1 = \hat{\mathbf{u}}_0\, e^{i(\mathbf{Q}_0\mathbf{r}_\parallel - q_0 z)} + \sum_{\mathbf{G},\nu} \beta^{+}_{G\nu}\hat{\mathbf{u}}^{\nu+}_{\mathbf{G}}\, e^{i(\mathbf{Q}_G\mathbf{r}_\parallel + q_{G,\nu} z)}\,, \tag{3.44a}$$

$$\mathbf{u}_2 = \sum_{\mathbf{G},n} \left[\alpha^{+}_n\mathbf{u}^{+}_{Gn}\, e^{iq_n(z+h)} + \alpha^{-}_n\mathbf{u}^{-}_{Gn}\, e^{-iq_n z}\right] e^{i\mathbf{Q}_G\mathbf{r}_\parallel}\,, \tag{3.44b}$$

$$\mathbf{u}_3 = \sum_{\mathbf{G},\nu} \beta^{-}_{G\nu}\hat{\mathbf{u}}^{\nu-}_{\mathbf{G}}\, e^{i(\mathbf{Q}_G\mathbf{r}_\parallel - q_{G,\nu}(z+h))}\,, \tag{3.44c}$$

where $\mathbf{k}_0 = (\mathbf{Q}_0, q_0)$ and corresponds to the incident longitudinal wavevector, $\mathbf{k}^{\pm}_{G\nu} = (\mathbf{Q}_G, \pm q_{G,\nu})$ such that $q_{G,\nu} = \sqrt{\mathbf{k}^2_\nu - |\mathbf{Q}_G|^2}$) with $\nu = \{\ell, p, s\}$ that implies the longitudinal $k_\ell = \omega/c_\ell$ and transverse wavenumber $k_p = k_s = \omega/c_t$ for isotropic solids.

Therefore, the unitary vectors $\hat{\mathbf{u}}^{\nu\pm}_{\mathbf{G}}$ with the displacement direction of the waves are defined as $\hat{\mathbf{u}}^{\ell\pm}_{\mathbf{G}} = \hat{\mathbf{k}}^{\pm}_{G\ell}$, $\hat{\mathbf{u}}^{p\pm}_{\mathbf{G}} = \pm\hat{\boldsymbol{\theta}}^{\pm}_{\mathbf{G}}$, and $\hat{\mathbf{u}}^{s\pm}_{\mathbf{G}} = \hat{\boldsymbol{\varphi}}^{\pm}_{\mathbf{G}}$ (see Figure A.1).

Using the orthogonality of the exponential functions within the unit cell one can write the continuity of the displacement at $z = 0$ and $z = -h$ as

$$\sum_{\nu'} \beta^{+}_{G\nu'}\, N^{\nu\nu'+}_{\mathbf{G}} = \sum_{n} \left[\alpha^{+}_n\tilde{M}^{\nu+}_{Gn}\, e^{iq_{G,\nu}h} + \alpha^{-}_n\tilde{M}^{\nu-}_{Gn}\right] - \left(\hat{\mathbf{u}}^{\nu+}_{\mathbf{G}}\right)^{*}\cdot\hat{\mathbf{u}}_0\delta_{G0}\,, \tag{3.45}$$

$$\sum_{\nu'} \beta^{-}_{G\nu'}\, N^{\nu\nu'-}_{\mathbf{G}} = \sum_{n} \left[\alpha^{+}_n\tilde{M}^{\nu+}_{Gn} + \alpha^{-}_n\tilde{M}^{\nu-}_{Gn}\, e^{iq_{G,\nu}h}\right]\,, \tag{3.46}$$

[1] `ZGEEV` from the `LAPACK` library

where

$$N_{\mathbf{G}}^{\nu\nu'\pm} = (\hat{\mathbf{u}}_{\mathbf{G}}^{\nu+})^* \cdot \hat{\mathbf{u}}_{\mathbf{G}}^{\nu'\pm}\,, \tag{3.47}$$

$$\tilde{M}_{\mathbf{G}n}^{\nu\pm} = \frac{1}{S}\iint_S (\hat{\mathbf{u}}_{\mathbf{G}}^{\nu+})^* \cdot \mathbf{u}_{\mathbf{G}n}^{\pm}\, d^2\mathbf{r}_\parallel\,. \tag{3.48}$$

Defining $L_{\mathbf{G}}^{\nu\nu'\pm}$ such that

$$\sum_{\nu''} L_{\mathbf{G}}^{\nu\nu''\pm} N_{\mathbf{G}}^{\nu''\nu'\pm} = \delta_{\nu\nu'}\,, \tag{3.49}$$

then

$$M_{\mathbf{G}n}^{\nu\pm\pm} = \sum_{\nu'} L_{\mathbf{G}}^{\nu\nu'\pm} \tilde{M}_{\mathbf{G}n}^{\nu\pm}\,. \tag{3.50}$$

Applying Eqs. (3.49) and (3.50) to both Eqs. (3.45) and (3.46) yields

$$\beta_{\mathbf{G}\nu}^{+} = \sum_n \left[\alpha_n^+ M_{\mathbf{G}n}^{\nu++}\, e^{iq_{\mathbf{G},\nu}h} + \alpha_n^- M_{\mathbf{G}n}^{\nu+-}\right] + \beta_\nu^0 \delta_{\mathbf{G}0}\,, \tag{3.51}$$

$$\beta_{\mathbf{G}\nu}^{-} = \sum_n \left[\alpha_n^+ M_{\mathbf{G}n}^{\nu-+} + \alpha_n^- M_{\mathbf{G}n}^{\nu--}\, e^{iq_{\mathbf{G},\nu}h}\right]\,, \tag{3.52}$$

where

$$\beta_\nu^0 = -\sum_{\nu'} L_{\mathbf{G}=0}^{\nu\nu'+} \hat{\mathbf{u}}_{\mathbf{G}=0}^{\nu'+} \cdot \hat{\mathbf{u}}_0\,. \tag{3.53}$$

The stress for a locally-isotropic solid can be explicitly written in terms of the strain as

$$\sigma_{nj} = \lambda\varepsilon\delta_{nj} + 2\mu\varepsilon_{nj}\,, \tag{3.54}$$

which yields for the stress in the z direction

$$\sigma_{xz} = \mu(\partial_x u_z + \partial_z u_x)\,, \quad \sigma_{yz} = \mu(\partial_y u_z + \partial_z u_y)\,, \quad \sigma_{zz} = \lambda\nabla\cdot\mathbf{u} + 2\mu\partial_z u_z\,. \tag{3.55}$$

Thus, the stress in the z direction at each region of the space can be calculated as

$$\sigma_{\parallel z}^1 = i\mu_1(\mathbf{Q}_0 u_{0z} - q_0 \mathbf{u}_{0\parallel})e^{i\mathbf{k}_0\mathbf{r}} + i\sum_{\mathbf{G},\nu} \beta_{\mathbf{G}\nu}^+ \mu_1 \left(\mathbf{Q}_{\mathbf{G}} u_{\mathbf{G}z}^{\nu+} + q_{\mathbf{G},\nu}\mathbf{u}_{\mathbf{G}\parallel}^{\nu+}\right) e^{i\mathbf{k}_{\mathbf{G}\nu}^+\mathbf{r}}\,, \tag{3.56}$$

$$\sigma_{zz}^1 = i(\lambda_1 \mathbf{k}_0\hat{u}_0 - 2\mu_1 q_0 u_{0z})e^{i\mathbf{k}_0\mathbf{r}} + i\sum_{\mathbf{G},\nu} \beta_{\mathbf{G}\nu}^+ \left(\lambda_1 k_{\mathbf{G},\ell}^+ \delta_{\nu\ell} + 2\mu_1 q_{\mathbf{G},\nu} u_{\mathbf{G}z}^{\nu+}\right) e^{i\mathbf{k}_{\mathbf{G}\nu}^+\mathbf{r}}\,, \tag{3.57}$$

$$\sigma_{\parallel z}^2 = i\sum_{\mathbf{G},n} \mu_2 \Big[\alpha_n^+ e^{iq_n(z+h)}(q_n \mathbf{u}_{\mathbf{G}n\parallel}^+ + \mathbf{Q}_{\mathbf{G}} u_{\mathbf{G}nz}^+) + \alpha_n^- e^{-iq_n z}(-q_n \mathbf{u}_{\mathbf{G}n\parallel}^- + \mathbf{Q}_{\mathbf{G}} u_{\mathbf{G}nz}^-)\Big] e^{i\mathbf{Q}_{\mathbf{G}}\mathbf{r}_\parallel}\,, \tag{3.58}$$

$$\sigma^2_{zz} = i\sum_{\mathbf{G},n}\Big[\alpha^+_n e^{iq_n(z+h)}\left(\lambda_2(\mathbf{Q}_\mathbf{G}\mathbf{u}^+_{\mathbf{G}n\parallel} + q_n u^+_{\mathbf{G}nz}) + 2\mu_2 q_n u^+_{\mathbf{G}nz}\right) + \alpha^-_n e^{-iq_n z}\left(\lambda_2(\mathbf{Q}_\mathbf{G}\mathbf{u}^-_{\mathbf{G}n\parallel} - q_n u^-_{\mathbf{G}nz}) - 2\mu_2 q_n u^-_{\mathbf{G}nz}\right)\Big] e^{i\mathbf{Q}_\mathbf{G}\mathbf{r}_\parallel}, \quad (3.59)$$

$$\sigma^3_{\parallel z} = i\sum_{\mathbf{G},\nu}\beta^-_{\mathbf{G}\nu}\,\mu_3\left(\mathbf{Q}_\mathbf{G}u^{\nu-}_{\mathbf{G}z} - q_{\mathbf{G},\nu}\mathbf{u}^{\nu-}_{\mathbf{G}\parallel}\right)e^{i\mathbf{k}^-_{\mathbf{G}\nu}(\mathbf{r}-i\mathbf{h})}, \quad (3.60)$$

$$\sigma^3_{zz} = i\sum_{\mathbf{G},\nu}\beta^-_{\mathbf{G}\nu}\left(\lambda_3 k^-_{\mathbf{G},\ell}\delta_{\nu\ell} - 2\mu_3 q_{\mathbf{G},\nu}u^{\nu-}_{\mathbf{G}z}\right)e^{i\mathbf{k}^-_{\mathbf{G}\nu}(\mathbf{r}-i\mathbf{h})}, \quad (3.61)$$

where $\mathbf{r} = (\mathbf{r}_\parallel, z) = (x, y, z)$, $\parallel$ denotes the (x, y) components, and $\mathbf{h} = (0, 0, h)$. Applying continuity of the stress at both sides of the plate and projecting over the unit cell area yields

$$\sum_{\mathbf{G}\nu}\beta^+_{\mathbf{G}\nu}\,B^{\nu+}_{\mathbf{G}n} = \sum_{n'}\left[A^+_{nn'}\,\alpha^+_{n'}\,e^{iq_{n'}h} + A^-_{nn'}\,\alpha^-_{n'}\right] + \sigma^{0n}_{\mathbf{r}z}, \quad (3.62)$$

$$\sum_{\mathbf{G}\nu}\beta^-_{\mathbf{G}\nu}\,B^{\nu-}_{\mathbf{G}n} = \sum_{n'}\left[A^+_{nn'}\,\alpha^+_{n'} + A^-_{nn'}\,\alpha^-_{n'}\,e^{iq_{n'}h}\right], \quad (3.63)$$

where $B^\pm_{\mathbf{G}\nu}$, $A^\pm_{nn'}$, and $\sigma^{0n}_{\mathbf{r}z}$ are defined as

$$B^{\nu+}_{\mathbf{G}n} = \mu_1\left(\mathbf{Q}_\mathbf{G}u^{\nu+}_{\mathbf{G}z} + q_{\mathbf{G},\nu}\mathbf{u}^{\nu+}_{\mathbf{G}\parallel}\right)\mathbf{u}^{+*}_{\mathbf{G}n\parallel} + \left(\lambda_1 k_\ell\delta_{\nu\ell} + 2\mu_1 q_{\mathbf{G},\nu}u^{\nu+}_{\mathbf{G}z}\right)u^{+*}_{\mathbf{G}nz}, \quad (3.64)$$

$$B^{\nu-}_{\mathbf{G}n} = \mu_3\left(-\mathbf{Q}_\mathbf{G}u^{\nu+}_{\mathbf{G}z} - q_{\mathbf{G},\nu}\mathbf{u}^{\nu+}_{\mathbf{G}\parallel}\right)\mathbf{u}^{+*}_{\mathbf{G}n\parallel} + \left(\lambda_3 k_\ell\delta_{\nu\ell} + 2\mu_3 q_{\mathbf{G},\nu}u^{\nu+}_{\mathbf{G}z}\right)u^{+*}_{\mathbf{G}nz}, \quad (3.65)$$

$$A^+_{nn'} = \sum_{\mathbf{G},\mathbf{G}'}\Big[\mu_{\mathbf{G}-\mathbf{G}'}\left(\mathbf{Q}_{\mathbf{G}'}u^+_{\mathbf{G}'n'z} + q_{n'}\mathbf{u}^+_{\mathbf{G}'n'\parallel}\right)\mathbf{u}^{+*}_{\mathbf{G}n\parallel} + \left(\lambda_{\mathbf{G}-\mathbf{G}'}(\mathbf{Q}_{\mathbf{G}'}\mathbf{u}^+_{\mathbf{G}'n'\parallel} + q_{n'}u^+_{\mathbf{G}'n'z}) + 2\mu_{\mathbf{G}-\mathbf{G}'}q_{n'}u^+_{\mathbf{G}'n'z}\right)u^{+*}_{\mathbf{G}nz}\Big], \quad (3.66)$$

$$A^-_{nn'} = \sum_{\mathbf{G},\mathbf{G}'}\Big[\mu_{\mathbf{G}-\mathbf{G}'}\left(-\mathbf{Q}_{\mathbf{G}'}u^+_{\mathbf{G}'n'z} - q_{n'}\mathbf{u}^+_{\mathbf{G}'n'\parallel}\right)\mathbf{u}^{+*}_{\mathbf{G}n\parallel} + \left(\lambda_{\mathbf{G}-\mathbf{G}'}(\mathbf{Q}_{\mathbf{G}'}\mathbf{u}^+_{\mathbf{G}'n'\parallel} + q_{n'}u^+_{\mathbf{G}'n'z}) + 2\mu_{\mathbf{G}-\mathbf{G}'}q_{n'}u^+_{\mathbf{G}'n'z}\right)u^{+*}_{\mathbf{G}nz}\Big], \quad (3.67)$$

$$\sigma^{0n}_{\mathbf{r}z} = iu^{+*}_{0n}\sigma^0_{\mathbf{r}z} = iu^{+*}_{0n}\left(\mu_1(\mathbf{Q}_0u_{0z} - q_0\mathbf{u}_{0\parallel}) + (\lambda_1\mathbf{k}_0\hat{u}_0 - 2\mu_1 q_0 u_{0z})\right). \quad (3.68)$$

Combining this two equations with Eqs. (3.51) and (3.52) one arrives to the following system depending only on $\alpha^\pm_n$

$$\sum_{n',s'}\Lambda^{ss'}_{nn'}\,\alpha^{s'}_{n'} = b^s_n, \quad (3.69)$$

with

$$\Lambda^{++}_{nn'} = \sum_{G\nu} \left[M^{\nu++}_{Gn'} B^{\nu+}_{Gn} - A^{+}_{nn'} \right] e^{iq_{n'}h}, \qquad \Lambda^{+-}_{nn'} = \sum_{G\nu} M^{\nu+-}_{Gn'} B^{\nu+}_{Gn} - A^{-}_{nn'}, \tag{3.70}$$

$$\Lambda^{--}_{nn'} = \sum_{G\nu} \left[M^{\nu--}_{Gn'} B^{\nu-}_{Gn} - A^{-}_{nn'} \right] e^{iq_{n'}h}, \qquad \Lambda^{-+}_{nn'} = \sum_{G\nu} M^{\nu-+}_{Gn'} B^{\nu-}_{Gn} - A^{+}_{nn'}, \tag{3.71}$$

$$b^{+}_{n} = -\sum_{\nu} \beta^{0}_{\nu} B^{\nu+}_{0n} + \sigma^{0n}_{rz}, \qquad b^{-}_{n} = 0. \tag{3.72}$$

Solving this system and replacing the solutions $\alpha^{\pm}_{n}$ back into Eqs. (3.51) and (3.52) let us calculate the transmitted sound power τ using Eq. (3.28) as in the rigid-solid case. Then, for solving the transmission problem a finite number reciprocal lattice vectors N_G and a finite number of phononic plate eigenmodes N_n is needed. The influence of the plate vibration leads to a much more complex equations than that of the naïve rigid-solid theory.

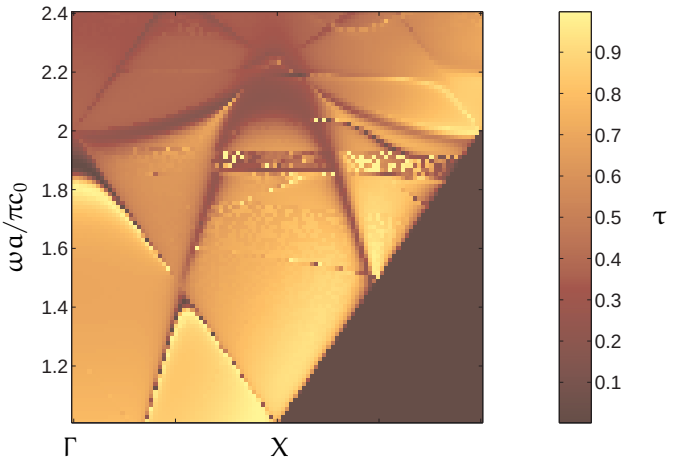

Figure 3.6: Transmitted sound power spectra obtained using the FEAM for a $d/a = 0.6$, $h/a = 0.2$ aluminum plate with a square hole array immersed in water in the ΓX direction of the irreducible Brillouin zone.

Figure 3.6 shows some spurious modes appearing ($N_G \sim 100$) which similar to those observed in [140]. These modes are mainly localized in the water-aluminum interface and originate in unphysical values of the Fourier-expanded Lamé coefficients because of the lack of shear modulus in the fluid medium. Spurious modes produce noise that can be partially removed by eliminating them from the expansion of the displacement **u**, although part of their effects are still discernible and increase with h. More detailed

discussion about the results obtained with this model will be discussed together with the experimental part in chapter 5.

Besides the aforementioned problem, the model is exact when the physical system consists in a solid-solid PhP immersed in a fluid and it is expected that it also could give accurate predictions when the semi-infinite fluid media are replaced by solid media.

Some solids, in particular polymers, show certain degree of sound attenuation at ultrasonic frequencies, e.g. [141] reports on PMMA attenuation in the MHz range. Following some simple phenomenological approximations from the lossy Helmholtz equation [101] the sound attenuation enters through a complex phase speed c'_ν defined as

$$c'_\nu = \frac{c_\nu}{1 + i\beta_\nu}\,, \tag{3.73}$$

such that the complex wavenumber yields

$$k'_\nu = \frac{\omega}{c_\nu}(1 + i\beta_\nu)\,, \tag{3.74}$$

from which is clear the frequency dependent behavior of the attenuation given by β_ν. As in the previous derivations, $\nu = \{\ell, t\}$ represents longitudinal and transverse waves.

3.4 Finite Element Approximation

Linear elasto-acoustic problems can also be solved using the so called Finite Element Method (FEM). This numerical method, which has been developing for more than half a century, is particularly well suited to solve problems having a geometry which is not readily accessible by means of analytic methods. With the explosive increase of computation capabilities in recent years, FEM is widely used to solve practical engineering problems. As a consequence, several commercial and open-source implementations are available.

For elasto-acoustic problems, the method can be understood in terms of a discretization of a particular version of the Helmholtz equation (A.8) and the wave equation in solids (A.2) (see [142] for more details and a general overview) considering both boundary conditions and fluid-solid coupling.

Although in this study the geometry is fairly simple, FEM not only provides a starting point to conduct further modeling of more complicated designs, but also constitutes a powerful tool to avoid the rise of spurious modes when using PWE for solid-fluid phononic crystals. However, due to constrains in the computational power only two-dimensional simulations are performed. Therefore, instead of two-dimensional hole arrays only one-dimensional slit arrays are studied with this method.

The transmission problem has been solved numerically by means of finite elements implemented in Comsol Multyphysics software for frequency domain, which by default uses $e^{i\omega t}$ time dependence. A unit cell of the slit array (see Fig. 3.7) having a period a, a slab thickness $h = 0.6a$, and an aperture of size $d = 0.28a$ constitutes the geometry of the problem. The slab is modeled as an elastic domain having zero out-of-plane components of the strain ($\partial_z \mathbf{u} = 0$) to keep the problem in two dimensions and neglecting transverse waves having out-of-plane polarization ($u_z = 0$).

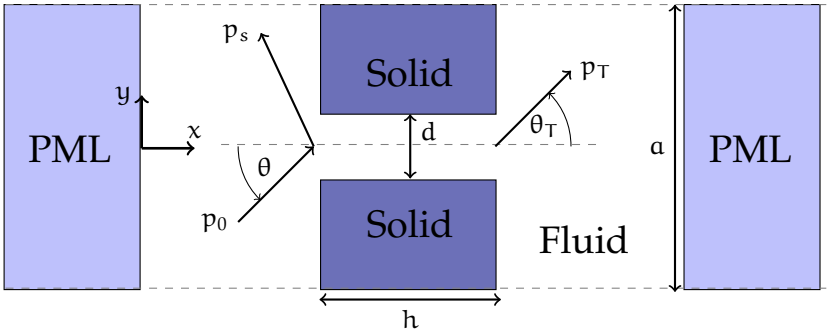

Figure 3.7: Scheme depicting the unit cell geometry used in the FEM simulation. Perfectly Matched Layer (PML) is an absorbing artificial medium useful to simulate free field conditions.

A fluid domain is used to model the slit and the surrounding media. The pressure p in the fluid is decomposed as the sum of incident p_0 (known) and scattered p_s (unknown) pressures, the first being a plane wave

$$p_0 = p_i e^{-ik_0(\sin(\theta)y - \cos(\theta)x)} . \tag{3.75}$$

The fluid-structure interaction is ensured by imposing continuity of both, the normal acceleration $\partial_t^2 \mathbf{u} = -\nabla p/\rho$ and the normal stress $\sigma_{ij} = -p\delta_{ij}$ at the fluid-solid interfaces. The periodicity enters through the lateral limits of the unit-cell via periodic boundary conditions as

$$p(x, -a/2) = p(x, a/2) e^{ik_0 \sin(\theta) a} , \tag{3.76}$$

in the fluid and as

$$\mathbf{u}(x, -a/2) = \mathbf{u}(x, a/2) e^{ik_0 \sin(\theta) a} , \tag{3.77}$$

in the solid. Finally, to satisfy the Sommerfeld radiation condition at infinity, Perfectly Matched Layers (PML) [143] are used at left and the right of the unit-cell. Wavelength-dependent scaling is applied to the mesh, the thickness of the PML, and the vertical size of the unit-cell. The transmitted and reflected sound power is calculated by integrating

the x sound intensity component along the unit-cell width right at the interface between the fluid domain and the PML as

$$\Pi_0 = \frac{1}{2}\frac{p_0^2 a\cos(\theta)}{\rho c}\,, \tag{3.78}$$

$$\Pi_t = \frac{1}{2}\int_{-a/2}^{a/2} \mathcal{R}e\{p v_x^*\}\,dy\,, \tag{3.79}$$

$$\Pi_r = \frac{1}{2}\int_{-a/2}^{a/2} \mathcal{R}e\{p_s v_{sx}^*\}\,dy\,. \tag{3.80}$$

Convergence is achieved for a mesh element size around $\lambda/15$ and has been tested through the balance of the total sound power and by comparison with a two-dimensional rigid-solid model.

4

Experiments

4.1 Experimental setup

In order to measure the acoustic transmission through a perforated plate and the wave propagation in the plate itself, underwater ultrasound has been chosen due to its advantages:

- As the plate is immersed in water, plate samples of the size of an A4 paper sheet can be used at ultrasonic frequencies.
- The acoustic impedance ($z_0 = \rho_0 c_0$) of the water is relatively high. Therefore, it makes possible to vary the impedance contrast between the plate and the water using common solid materials.

Two different techniques have been employed to measure wave properties of periodically perforates plates. Both rely on accurate alignment and positioning provided by an automated positioning system (Artitecnic DS4) built around a water tank as depicted in Fig. 4.1(a). This system consists in three motorized cartesian axes, one rotational motorized axis, and three manual cartesian axes.

Depending on the measurement technique, two different kind of transducers are used: a Polyvinylidene fluoride (PVDF) needle hydrophone (see Fig. 4.1(b)) and a piston underwater piezoelectric transducer (see Fig. 4.1(c)), which can be employed as a receiver and emitter.

On the one hand, the couple of piston transducers (Imasonic) are centered at a frequency of 250 kHz, have an active diameter of 32 mm, and its nearfield distance reaches up to 43 mm. On the other hand, the needle hydrophone (Precision Acoustics

Ltd.) model HPM1/1 has a sensor diameter of 1 mm and its ±4 dB bandwidth spans from 200 kHz to 15 MHz.

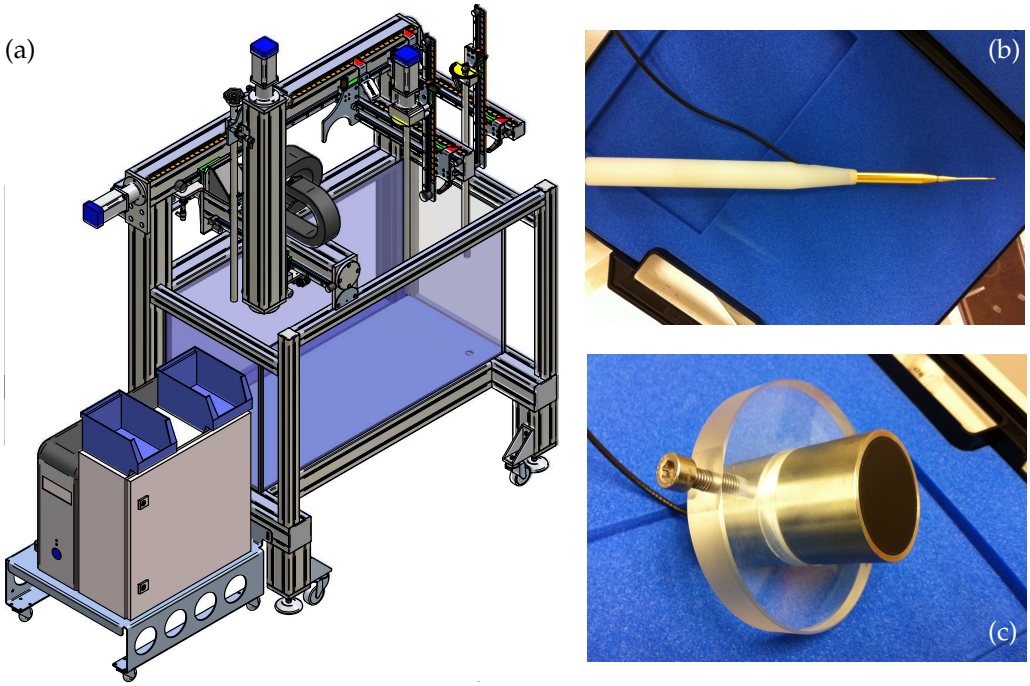

Figure 4.1: (a) Automated scanning system and water tank (from Artitecnic DS4 Operation Manual). (b) Needle hydrophone with mounting piece. (c) Immersion ultrasonic transducer with mounting piece.

Further equipment and software is required to synchronize the source, the receiver, the positioning stage, and eventually to register the measured data. This equipment is rather standard and will be briefly described as follows. A pulser/receiver generator (Panametrics model 5077PR) produces a pulse which is applied to the emitter transducer that launches the signal through the system under study. Then, the signal is detected by the receiving transducer, acquired by the pulser/receiver, post amplified, and digitized by a digital oscilloscope (Picoscope model 3224). This process is repeated and controlled from a computer which synchronizes via software (3DreamsUltra) the data acquisition from the oscilloscope and the automated positioning from the Motion Control card (National Instruments model 7344). The sampling frequency is limited ultimately by

the oscilloscope and reaches 10 MHz, which is at least ten times higher than the frequency range under study.

4.2 Underwater measurement techniques

4.2.1 Transmission measurements

The experimental setup is based on the well known ultrasonic immersion transmission technique (Fig. 4.2). This technique makes use of a couple of transmitter/receiver ultrasonic transducers (see Fig. 4.1(c)). Each transducer was located at a distance larger than that of its nearfield distance from the plate and aligned with respect to the plate.

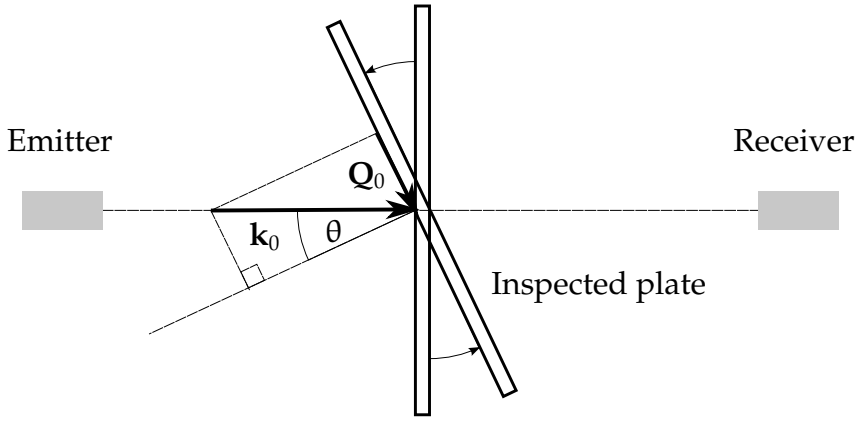

Figure 4.2: Diagram of the experimental setup. This setup makes possible to explore the transmission coefficient at different angles of incidence. $\mathbf{Q}_0$ corresponds to the component of the incident wavevector $\mathbf{k}_0$ which is parallel to the plate.

A pulse is launched by the emitter piston transducer through the inspected plate. Then, the signal is detected by the receiving piston transducer and acquired. Time domain data is finally analyzed after averaging 100 different measures and deleting unwanted reflections by means of a time window. Also the reverberation of the tank must be considered as it restricts the use of high Pulse Repetition Frequency (PRF). For the present setup, a PRF= 20 Hz satisfied the requirements of leaving the reverberation below the noise level. The signal-to-noise ratio can be increased by averaging different measurements under the same experimental conditions. The noise is then reduced as $10\log(I)$, where I is the number of signals included in the average, so that 100 averaged signals increase the signal-to-noise ratio in ≈ 20 dB.

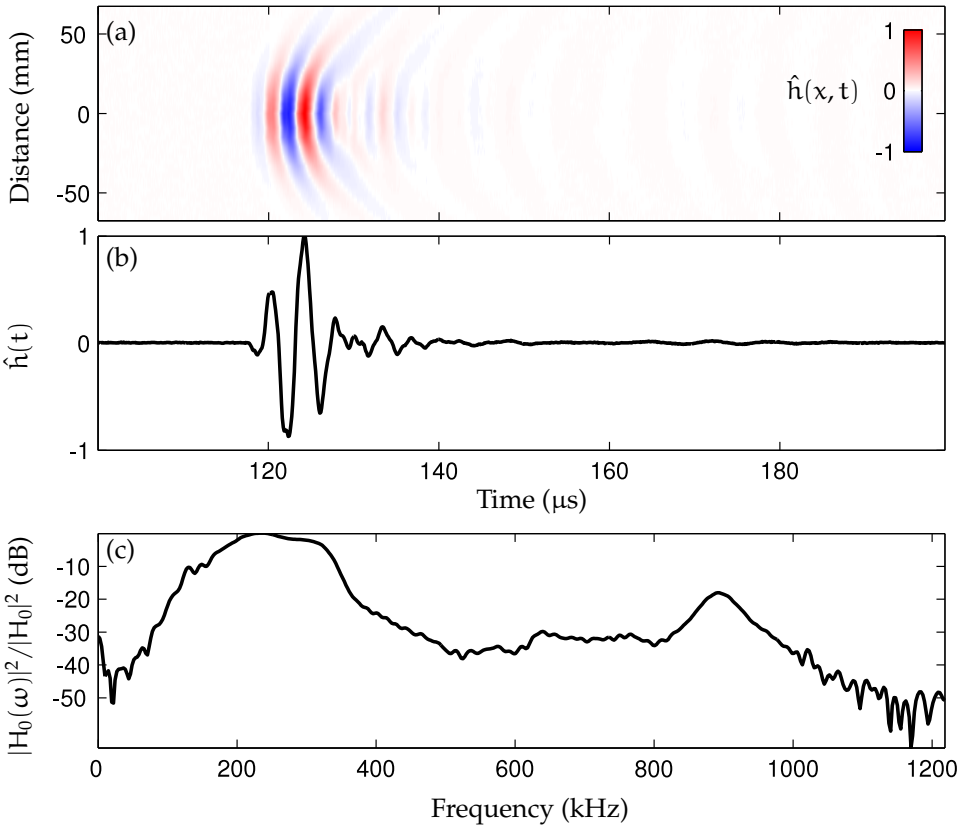

Figure 4.3: (a) Normalized amplitude of signals after averaging 100 pulses (color scale) as a function of the distance and the time of flight of the pulse measured with the 250 kHz transducer couple (emitter and receiver). (b) Slice of the previous plot showing the normalized amplitude against the time of flight. (c) Normalized frequency response of the previous pulse.

The normalized pulse amplitude $\hat{h}(t)$ launched and measured by the piston transducer couple in the water tank is depicted in color scale in Fig. 4.3(a) as a function of the time of flight and the off-axis distance. The transducers are placed at a distance around 180 mm from each other. Both the beam spreading and the low frequency tail are visible from the plot. A slice for $x = 0$ mm is plotted in Fig. 4.3(b), where it is clear that most of the energy is condensed in around 20 μs. Employing the Fourier transform to obtain the pulse power spectrum $|H_0(\omega)|^2$ in absence of any obstacle and normalizing by its maximum $|H_0|^2$, $|H_0(\omega)|^2/|H_0|^2$ is obtained (see Fig. 4.3(c)). The main broad peak is placed around 250 kHz , with a -6 dB frequency range from 155 kHz to 350 kHz.

Given the power spectrum $|H(\omega)|^2$ measured with a sample plate between the trans-

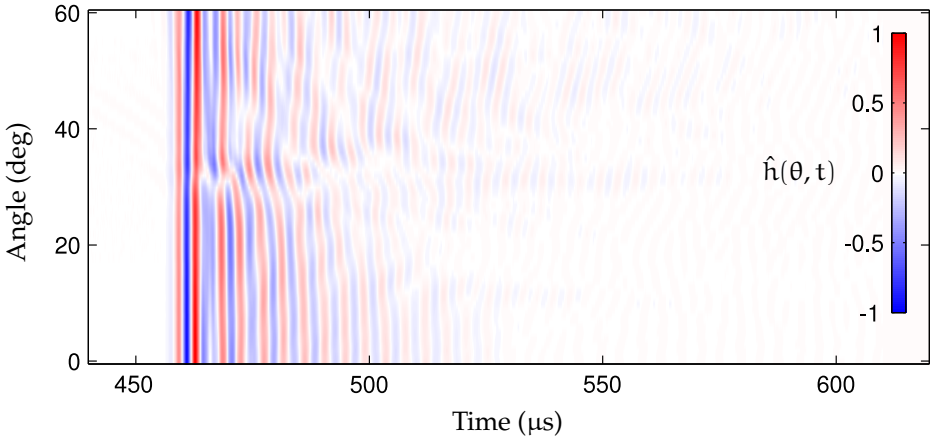

Figure 4.4: Normalized amplitude of signals after averaging 100 pulses measured by the 250 kHz transducer couple (emitter and receiver) with a plate placed between them as a function of the rotation angle and the time of flight.

ducers, the transmission spectrum is then calculated as

$$|T(\omega)|^2 = \frac{|H(\omega)|^2}{|H_0(\omega)|^2}\,. \tag{4.1}$$

If the plate is rotated, $h(\theta, t)$ can be measured as shows Fig. 4.4. Then,

$$|T(\theta, \omega)|^2 = \frac{|H(\theta, \omega)|^2}{|H_0(\omega)|^2}\,. \tag{4.2}$$

as $Q_0 = k_0 \sin(\theta)$ (see Fig. 4.2) and assuming that $k_0 c = \omega$, where c is the wave velocity in water, a simple mapping lead us to $|T(\omega \sin(\theta)/c, \omega)|^2 = |T(Q_0, \omega)|^2 \approx \tau(Q_0, \omega)$. Then, the direction in which Q_0 is varied is perpendicular to the rotation axis and is bounded to the plate.

Normalization leads to transmission values slightly above 100% in some cases, which we attribute to the finite size of the incident wave so that the wave front generated by the transducer is not perfectly plane. Similarly, finite size effects can appear in the measurements if the number of holes is small. Actually, these effects can be minimized using large arrays (39 holes $\times$ 39 holes).

Typically, angle dependent measurements were done in angle steps of $\Delta\theta = 1^o$ and comprising $0^o \leqslant \theta \leqslant 60^o$. Some of the features found in perforated plates attracted our attention and measurements using a higher angular resolution were performed. However, from the results, it turned out that the main limitation is not the angular

resolution of the plate rotation but the beam aperture of the flat transducers. Then, $\Delta\theta = 1^o$ has been found to be adequate to accomplish this study.

4.2.2 Nearfield in-plate excitation measurement

A very interesting feature of plates immersed in the fluid is the existence of guided modes which are confined onto the fluid-solid interfaces and the plate. Scholte-Stoneley modes lie within this category. As they develop just at the sound line and even with lower velocities than the sound velocity in the fluid at low frequencies, they cannot be measured using transmission techniques. As the source beam in the transmission setup solely excites the leaky part of the dispersion, only the direct excitation of the plate can trigger the propagation of non leaky modes. Furthermore, as these modes, in principle do not leak energy to the far field, the receiver transducer must be placed as close to the plate as possible, but causing minimum field distortion. This is the reason why a needle hydrophone is used as the receiver and a small piezoelectric transducer is bonded to the plate and employed as a source (see Fig. 4.5).

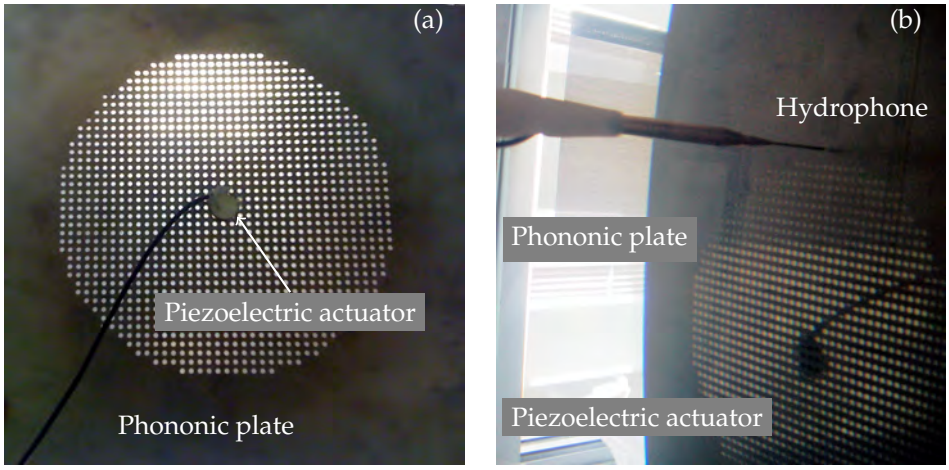

Figure 4.5: (a) Phononic plate having the piezoelectric actuator bonded at the center of the array. (b) Measurement setup including the needle hydrophone and the piezoelectric actuator attached to the inspected plate.

The electrical signal measured by the hydrophone is proportional to the dynamic pressure in the fluid. Thus, the pressure measured by the hydrophone when it is placed close to the plate ($\sim$ 1 mm in our case) provides a good approximation to the stress component normal to the plate surface.

The needle hydrophone is depicted in (see Fig. 4.1(b)). The actuator correspond to a piezoceramic disc (Steiner&Martins Inc. model SMD15T09S411, 15 mm in diameter and 1 mm thick) bonded to the plate by means of cyanoacrylate based adhesive and covered with a thin silicone layer to avoid electrical short circuit. The electronic and acquisition module is the same described before with the addition of a preamplifier just before the hydrophone to stabilize the signal.

Common techniques use liquid [144] and solid [145] wedges attached to the transducers to excite Lamb waves. However, considering the geometry of the array, a simple piezoceramic disc at its center is found to be more appropriate to our purposes.

The dispersion of the plate modes can be then measured performing a linear spatial scan with the hydrophone on the inspected plate surface, taking into account the array symmetry when choosing the scanning path. Then, performing two-dimensional Fourier transform [146] on both temporal and spatial domain, the dispersion map as a function of both the frequency and the parallel to the plate wavevector can be obtained.

A total scanned length of 220 mm covering the array diameter in steps $\Delta x = 0.25$ mm is measured using an automated positioning system (see Fig.4.1(a)). Defining x as the distance from the hydrophone to the piezoelectric disk source and selecting the measurement path passing through the source on the opposite plate face one can obtain the electric tension amplitude h in (V) given by the hydrophone as a function of x and the time t. As an example, Fig. 4.6 depicts $h(x,t)$ after averaging 128 pulses at each measurement position. The color scale clearly saturates when the hydrophone

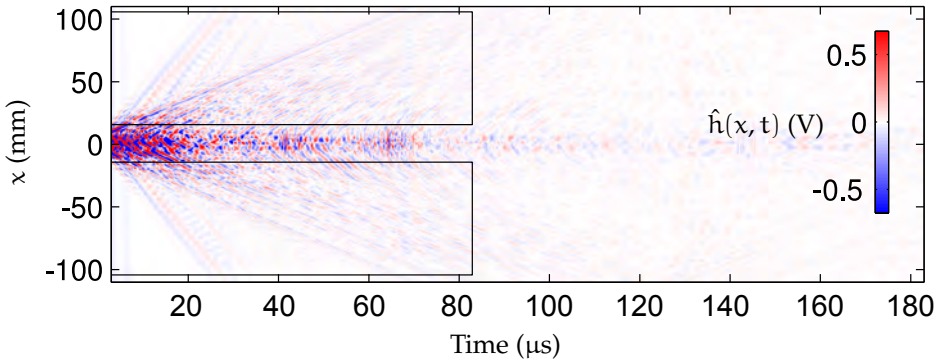

Figure 4.6: Electric tension signal (color scale) given by the hydrophone as a function of time t and the distance x relative to the source. The regions delimited by the rectangle are those on which Fourier transform is calculated.

passes near the source position. However, this region contains information regarding the source coupling to the plate, which is not of interest in this study. Indeed, the

regions delimited by the rectangles at the upper and lower parts of the plot comprise the information related with the propagation of waves in the plate. The harmonic analysis is then performed over these regions.

The two-dimensional Fourier transform of $h(x,t)$, denoted as $H(Q,\omega)$ is symmetric with respect to ω but it is non-symmetric with respect to Q. This behavior can be easily understood by the simple fact that while the waves do not propagate backwards in time they do propagate backwards in space relative to a given direction. Moreover, waves having negative group velocity, i.e. $d\omega/dQ < 0$, will appear having positive group velocity $d\omega/dQ > 0$ but negative phase speed $\omega/Q < 0$, which necessarily implies that $Q < 0$. Thus, some information related with negative group velocity propagation and with wave reflections appears at the side of the Fourier transform having $Q < 0$. In order to compare our results with the theory, we would need to represent both sides of the dispersion in just one side for $|Q|$. Taking modulus of the Fourier transform $|H(\pm Q,\omega)|$ and defining Λ as

$$\Lambda(|Q|,\omega) = \frac{1}{2}\left(|H(Q,\omega)| + |H(-Q,\omega)|\right) , \tag{4.3}$$

will allow the observation of all the dispersion properties in a single measurement shot.

4.3 Perforated plates

The measurements were made using aluminum plates (see Fig. 4.7) having around 200 mm in width and 350 mm in length ($\rho = 2700$ kg/m^3, $c_l = 6467$ m/s, $c_t = 3120$ m/s) immersed in water ($\rho = 1000$ kg/m^3, $c_l = 1480$ m/s). Also brass ($\rho = 8560$ kg/m^3, $c_l = 4280$ m/s, $c_t = 2030$ m/s) and PMMA ($\rho = 1270$ kg/m^3, $c_l = 2770$ m/s, $c_t = 1430$ m/s) plates were measured.

If the hole size is too small compared with the wavelength, viscous effects cannot be neglected. One approach to account viscous effects in the holes is to calculate the viscous boundary layer thickness d_v, which for liquids takes the form [147]

$$d_v = \sqrt{\frac{2\mu'}{\rho\omega}} , \tag{4.4}$$

where μ' is the (shear) viscosity coefficient. For water at 25 ^{o}C, $\mu' = 8.9$ mPa s [148] yielding $d_v \approx 10$ μm in the kHz range. Thus, viscous effects can safely be neglected as the hole size is at least two orders of magnitude above the viscous boundary layer thickness.

One step forward starting from the perforated plate is the fabrication of a solid-solid phononic plate by filling the holes with a polymer. PMMA and epoxy resin have

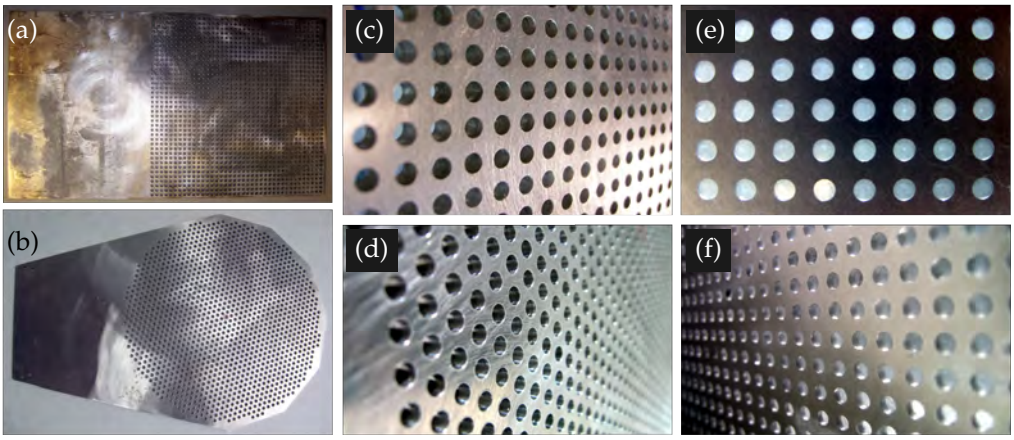

Figure 4.7: Some of the aluminum perforated plates used in the experiments having (a), (c) a square lattice and (b), (d) a triangular lattice. (e) Aluminum-epoxy phononic plate and (f) aluminum-PMMA phononic plate.

been used due to its elastic constants, which are close to that of water, and provide an acceptable impedance mismatch with the aluminum.

Of course, the presence of air bubbles inside the resin or PMMA-filled holes constitutes a major drawback and has been successfully avoided. However, if the plate is thin ($h < 2\,\text{mm}$) the polymer excess layer could deform the plate producing a bias strain. In this case, the polymer excess must be carefully removed because small cracks inside the holes could appear as a result of the back action of the plate trying to recover its original shape.

4.3.1 Al-Epoxy phononic plates

The resin filling process was performed by the Mechanical and Materials Engineering Department of the UPV. The epoxy resin Prime 20LV (Gurit Ltd.) is used in 100:26 proportion with a slow hardener. After 20 minutes at rest to allow small bubbles to leave the mixture, the resin is poured into the mold, which contains the perforated plate, until the holes brim with resin. The plate lies above a plastic film to make the unmolding process easier. Eventually, after 72 hours curing, the plate is unmolded and sanded to remove the resin excess from both sides of the plate. This last process is critical in the sense that small parts of resin can be taken off when the plate is sanded, thus leaving a

small hole defect particularly near to the aluminum-resin interface. An example of these aluminum plates with epoxy resin inclusions can be observed in Fig. 4.7(e).

4.3.2 Al-PMMA phononic plates

Methyl methacrylate monomer is polymerized by means of benzoyl peroxide as a catalyst. Also a small proportion of PMMA powder can be used to both accelerate the polymerization and reduce the amount of monomer involved in the process. The plate and the monomer are placed inside a chemically-resistant plastic bag under the radiation of two infrared bulbs to control the temperature. Once the polymer is cured, the plate is ground to remove the unwanted PMMA from the surface. A photograph of one of these plates can be seen in Fig. 4.7(f).

It has been observed that some aluminum particles got stuck in the PMMA surface presumably due to the high temperature reached while grinding the plate. It is worthwhile to mention that also the flatness of the phononic plate is affected by the grinding process. In fact, deviations of the plate thickness reached values as large as 0.5 mm.

4.3.3 Random arrays

In addition to the periodic lattices, pseudo-random lattices have been studied. As can be seen in Fig. 4.8(b) and (d), the array is not perfectly random, firstly because of its finite size and secondly, because it was designed to have the same global filling fraction than the periodic array. This strategy was conceived to properly address the effect of the translation invariance. Thus, as shows the spatial Fourier transform in Fig. 4.8(d), there is a broad annular maxima having a radius similar to that of the periodic transform (Fig. 4.8(c)) first order discrete maxima.

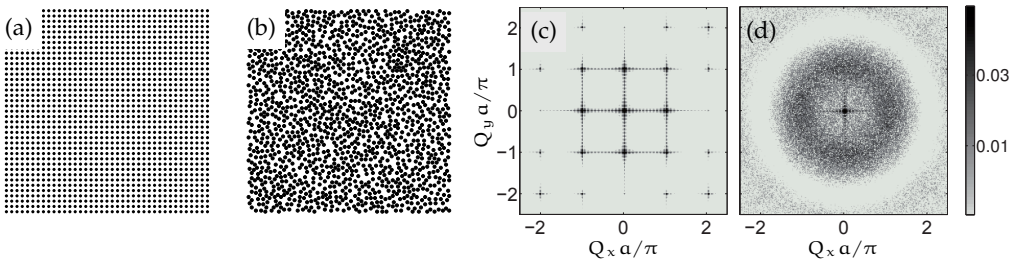

Figure 4.8: Position of the holes for the (a) periodic and (b) random array. Magnitude of the spatial Fourier transform (gray scale) of the (a) periodic and (b)s random hole distribution respectively.

5

Results analysis

In this chapter, experimental results obtained by means of the described techniques are presented and discussed in the light of the theoretical models.

5.1 Resonant transmission

When sound impinges onto a hole of finite depth, transmission peaks will arise due to the FPRs even if the hole size is subwavelength because it is the hole depth and not the hole cross-section what governs these resonances. Increasing the number of holes could lead to interesting results, as showed in Fig. 5.1.

Three aluminum plates of the same thickness, $h = 2\,\text{mm}$, are measured at normal incidence. Two of them have around 1500 holes of diameter $d = 3\,\text{mm}$ arranged periodically ($a = 5\,\text{mm}$, $f_\square = 0.28$) and pseudo-randomly ($\bar{f} = 0.28$), whereas the third plate has no holes. Figure 5.1(a) shows the transmitted sound power coefficient τ of the three plates as a function of the wavelength in water. Nearly full transmission can be observed when the holes are distributed periodically (Fig. 5.1(a)), which does not occur neither for the homogeneous plate nor for the randomly perforated one. The homogeneous plate response is feature less, characterized by a monotonic increase of the transmission as the wavelength becomes longer. On the other hand, the spectrum of the random array resembles that of the periodic one, particularly at the minimum between 5 mm$< \lambda <$6 mm. However, when the periodic hole distribution reaches almost full transmission, the random hole array only reaches $\tau = 0.5$. At $\lambda >$8 mm both spectra are very close. Moreover, one could expect both spectra to be equal in the deep subwavelength regime as they share almost the same global filling fraction.

The experimental evidence thus suggest that the periodicity of ordered arrays facilitates a cooperative effect in the holes transmission. This coherent phenomenon relies on the translational invariance of the array, which guarantees a single resonance for each direction of sound incidence. Once the translational invariance is broken, different resonant wavelengths for different hole environments appear, thus leading to a transmission spectrum with lower values of the transmission.

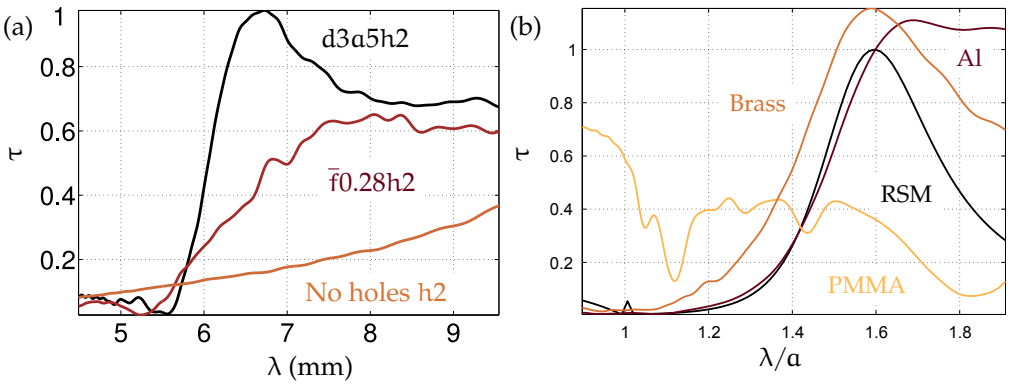

Figure 5.1: Measured transmission spectra of perforated plates immersed in water at normal incidence. (a) Transmittance spectra of 2 mm thick aluminum plates pierced by holes of 3 mm in diameter, distributed periodically with $a = 5$ mm (d3a5h2) and randomly with an average filling fraction $\bar{f} = 0.28$ ($\bar{f}$0.28h2). The transmission of the homogeneous plate is shown for comparison. (b) Comparison between measurements and rigid-solid model (RSM). The perforated plates are made of different materials (brass, aluminum (Al), and PMMA) but share the same geometrical parameters, namely $d = 3$ mm, $a = 5$ mm, $h = 3$ mm, and 11×11 holes.

The characteristic acoustic impedance z_0 is given by the product between the fluid density ρ_0 and the phase velocity c_0. The impedance mismatch between a solid and a fluid will be simply considered as $K = z_s/z_0 = \rho c_l/\rho_0 c_0$, where ρ is the solid density and c_l is the longitudinal wave velocity in the solid. This ratio controls the sound transmission through a fluid-solid interface at normal incidence. On the other hand, the c_t/c_0 ratio determines whether the wave motion of a homogeneous plate is governed by leaky Lamb waves and one Scholte-Stoneley mode ($c_t/c_0 > 1$) [149] or mainly by Scholte-Stoneley waves as it occurs in a fluid-solid interface ($c_t/c_0 < 1$) [150].

The crucial role of the impedance mismatch in the resonant transmission peaks can be observed in Fig. 5.1(b), where the transmitted sound power is plotted against the normalized wavelength (λ/a). The transmission spectra of PPPs made of different materials but having the same square lattice are compared with the RSM for normal

incidence. The impedance ratio relative to water is 25 for brass, 11.8 for aluminum, and 2.1 for PMMA. The transmission curve for brass follows quite closely the prediction of the RSM. In the case of aluminum, it also agrees rather well with the theory except at long wavelengths, where the transmission is still being large after the resonance compared with the theory and the brass. This step-like behavior found for perforated aluminum plates can be attributed to the lower impedance mismatch. A completely different picture from those of the brass and the aluminum plates is observed for the PMMA plate. The very strong coupling of the PMMA and the water results in a larger amount of energy passing through the bulk plate. Moreover, 60% transmission is obtained instead of the dip when $\lambda \approx a$ observable in the other two spectra.

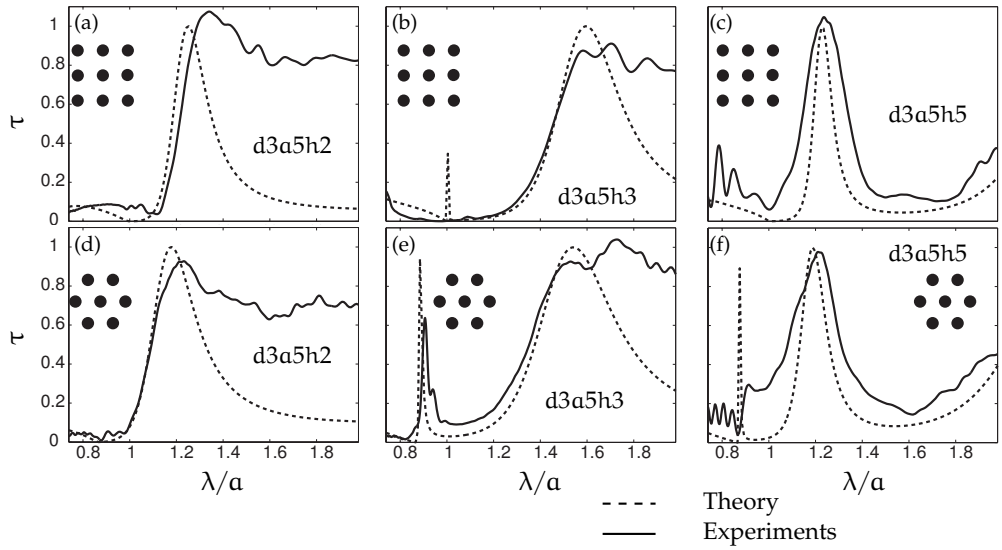

Figure 5.2: Comparison between measured and calculated sound power transmission of PPPs at normal incidence. Different plate thicknesses and lattice geometries are shown keeping d and a constant as indicated by the labels. The measurements correspond to perforated aluminum plates immersed in water, whereas the calculations were performed with the rigid-solid model.

An extended comparison between the RSM and the measurements is shown in Figs. 5.2 (a)-(f) for different plate proportions and lattices. Good agreement can be observed between measurements for aluminum plates and the RSM. The main differences can be explained by the finite impedance mismatch between aluminum and water, in particular the high transmission values after the resonance in Figs. 5.2 (a), (b), (d), and (e) which are not predicted by the theory as mentioned before. Transmission values slightly above unity in the resonances can be attributed to finite-size effects of both, transducers and perforated plates. The transmission minima is placed in a different po-

sition depending on the lattice geometry. Instead of the $\lambda/a = 1$ position for the square lattice, it appears at $\lambda/a = \sqrt{3}/2 \approx 0.87$ for the triangular lattice. This difference implies a direct relationship between the transmission dip and the array pitch in a similar way to what takes place in optical diffraction gratings [38] which is called Wood anomaly.

The increase in the plate thickness h shifts the transmission peak towards larger wavelength values for both lattices. Although this statement could seem to be invalid when $h = 5$ mm, this peak is actually related to the first-order FPR instead of the zero-order FPR, which is out of the measurement range. Both, zero and first-order resonance-related peaks appear together for Fig. 5.2 (e), where the very narrow peak near to the Wood anomaly is related to the first-order resonance. A similar case should be observed in Fig. 5.2 (b) as predicted by the theory but in this case the peak is so narrow that it could not be resolved in the measurements. Small losses from the water and in the holes could complicate the detection of these very narrow peaks.

The dependence of the transmission coefficient τ on the geometrical parameters of the plate and the hole array under normal incidence was calculated using the rigid-solid model and is shown in Fig. 5.3. Each contour plot corresponds to one line in the parameter space of Fig. 5.3 (a) related to four different d/h ratios. The filling fraction is then varied through a retaining d/h constant.

A first sight in Fig. 5.3 shows full transmission in all cases. The number of peaks is directly related to the thickness as they depend on the FPRs inside the hole. However, the position of the peaks is highly influenced by the array periodicity. For an open tube, the FPRs appear at $\lambda/h = 2/j$ (with j being integer) which is very near to the full transmission for high filling fraction values, but the transmission peak for an individual hole is actually placed at larger wavelengths as show the white vertical dashed lines in Figs. 5.3 (b)-(e). Thus, the resonant peak can be tuned only within the open tube resonance position and the single hole transmission resonance position.

As the filling fraction decreases, the peak moves to larger wavelength values following the $\lambda = a$ minima and becomes narrower. While for a single hole the transmission peak is higher for the lower order Fabry-Pérot modes (see Fig. 2.7), in the periodic case each Fabry-Pérot mode reaches nearly full transmission. The influence of the filling fraction of holes [50] via periodicity variation shows a high interaction, which is translated into peak narrowing when the filling fraction decreases together with a shift in the peak position towards longer wavelengths.

Until now, the arrays under consideration have all the holes of the same size. By considering a compound array consisting in two different arrays having different hole size one could expect to observe some degree of interaction between the hole resonances. Two different perforated plates are studied. Plate A has a plate thickness $h = 0.375a$

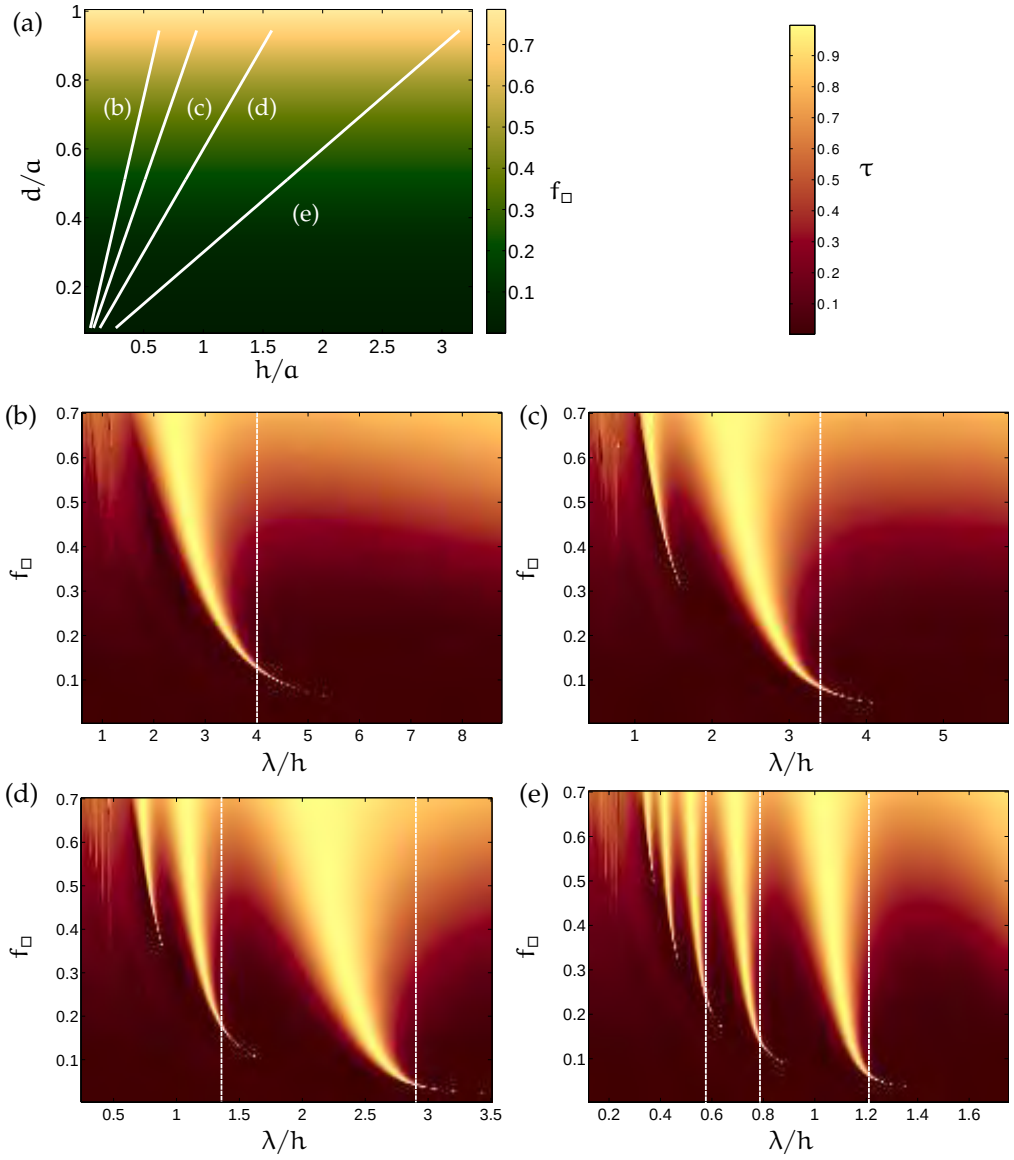

Figure 5.3: Transmitted sound power τ (color scale) through PPPs as a function of λ/h and the filling fraction for a square array $f_\square$ calculated with the rigid-solid model for normal incidence. The parameter space (a) shows the possible proportions of the perforated plate and their corresponding $f_\square$ value (color scale). Each contour plot represents a line in (a) for (b) $d/h = 1.5$, (c) $d/h = 1$, (d) $d/h = 0.6$, and (e) $d/h = 0.3$. The vertical white dashed lines correspond to the position of the resonances calculated for an individual hole.

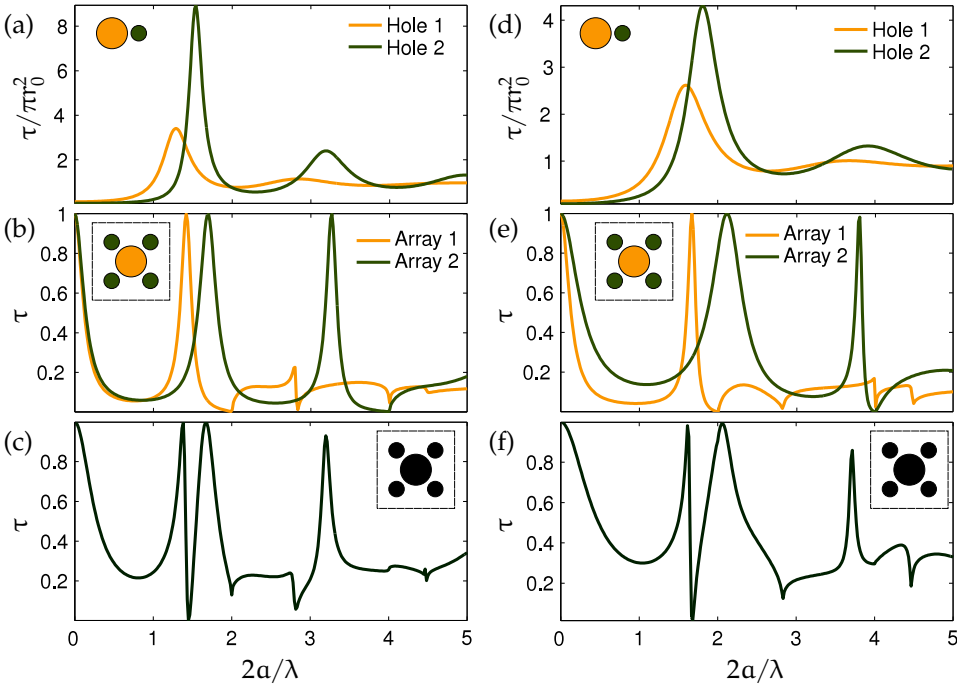

Figure 5.4: Sound transmission through single hole (top row), simple hole array (medium row), and compound hole array (bottom row). The left column corresponds to the A plate whereas the right column to the plate B.

and hole diameters $d_1 = 0.375a$, $d_2 = 0.25a$. On the other hand, plate B has $h = 0.5a$, $d_1 = 0.4a$, and $d_2 = 0.2a$. The transmitted sound power coefficient τ is shown as a function of the normalized incident wavenumber for normal incidence in Fig. 5.4. The inset in each panel sketches the geometry used in the calculations. In addition to the compound hole array curves (Figs. 5.4(c) and (f)) the normalized sound transmitted power for the individual holes (Figs. 5.4(a) and (d)) and τ for the simple square arrays that form the compound array (Figs. 5.4(b) and (e)) are also depicted for plate A (left column) and plate B (right column).

It can be clearly seen from the single hole spectra, that the resonances of the two hole sizes are slightly different, even though they share the same thickness. This difference in the resonance frequency is enough to be seen in the spectra of the simple hole arrays. Then, the same resonant transmission peaks can be seen in the compound array spectra with some differences. A new minimum arising probably from the interference [61]

between both arrays can be observed between the two peaks located at $1 < 2a/\lambda < 2$. The base transmission contour is higher, presumably due to the higher filling fraction of the compound array. This effect is clearer at very large wavelengths. Although the first resonant transmission peak of the small array (array 2) is very near to the Wood anomaly of the array 1 it is not quenched and nearly full transmission prevails. A similar behavior can be observed for the second peak of the array 2, which is well beyond the diffraction limit if the compound array period a is considered.

5.2 Wood anomalies

The dips found at normal incidence measurements are related to Wood anomalies. In the following section the geometrical nature of these anomalies is clearly set in the light of the transmission dispersion.

Figure 5.5 shows results of four different plates, whose geometrical parameters are shown in the lower side corners of the panels. The transmission τ is in linear color scale as function of the normalized frequency $\omega a/\pi c_0$ and the parallel-to-plate wavevector $\mathbf{Q}_0$ along the MΓ and ΓX directions of the irreducible Brillouin zone. The effect of the filling fraction ($f_\square$) is reflected in the transmission dispersion, where it is clear that the smaller the filling fraction, the narrower the peaks. It is remarkable the fact that all spectra share the same position of the minima when the axes are normalized by the array period a. This give us another evidence of its geometrical nature. These minima were also observed by Wood in terms of sharp reflection maxima when light impinges in a diffraction grating [38]. As predicted by Rayleigh the minimum is produced by the coherent interference between holes. The Wood anomaly is given by the following condition:

$$k_0 = |\mathbf{Q}_0 + \mathbf{G}|\,, \tag{5.1}$$

e.g. when a diffracted beam becomes grazing to the array plane. Therefore, it only depends on the array symmetry. Equation (5.1) can be explicitly written for a square array as

$$\frac{\omega}{c} = |\mathbf{Q}_0 + \mathbf{G}| = \sqrt{\left(Q_{0x} + \frac{2\pi}{a}m_1\right)^2 + \left(Q_{0y} + \frac{2\pi}{a}m_2\right)^2}, \tag{5.2}$$

and for a triangular array as

$$\frac{\omega}{c} = |\mathbf{Q}_0 + \mathbf{G}| = \sqrt{\left(Q_{0x} + \frac{2\pi}{a}(m_1 + m_2)\right)^2 + \left(Q_{0y} + \frac{2\pi}{a\sqrt{3}}(m_1 - m_2)\right)^2}. \tag{5.3}$$

The transmission vanishes right when this condition is satisfied. Different values of the Miller indices (m_1, m_2) produce the several minimum curves. Like in the optical case,

these transmission dips are driven by lattice-sum singularities originating in cumulative in-phase scattering among the holes of the array.

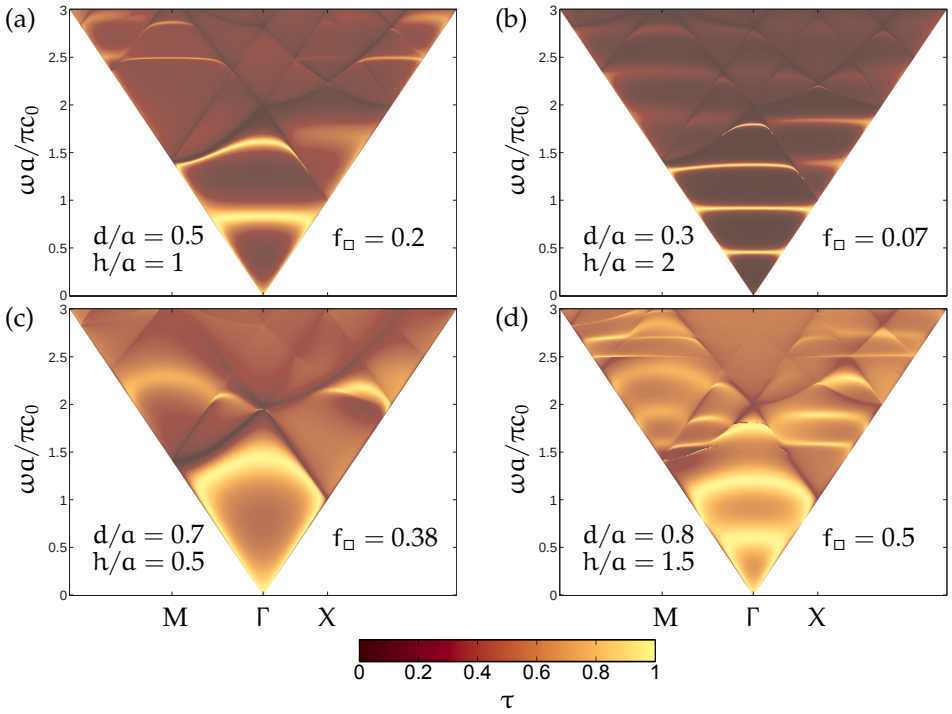

Figure 5.5: Transmitted sound power τ (color scale) through plates with a square array of holes as a function of the normalized frequency $\omega a/\pi c_0$ and the wavevector $\mathbf{Q}_0$ along the MΓX directions of the irreducible Brillouin zone (see Fig. 3.3(a)). Four different cases are shown with their proportions placed below the sound cone.

The number of transmission peaks is given by the plate thickness but also depends on the periodicity due to their interaction with the Wood anomaly modes. One remarkable fact is the existence of full transmission peaks that are independent of the angle of incidence. This can be seen in Figs. 5.5 (a), (b), and (d).

In addition, we can explore the transmission properties of square and rectangular compound arrays [62] as shown in Fig. 5.6. The compound hole arrangement consists in a primary square array which is decorated with a larger secondary array that can be square (Fig. 5.6(a)) or rectangular (Fig. 5.6(b)). The symmetry of the resulting structure is given by the symmetry of the secondary array. Thus, three different samples are defined

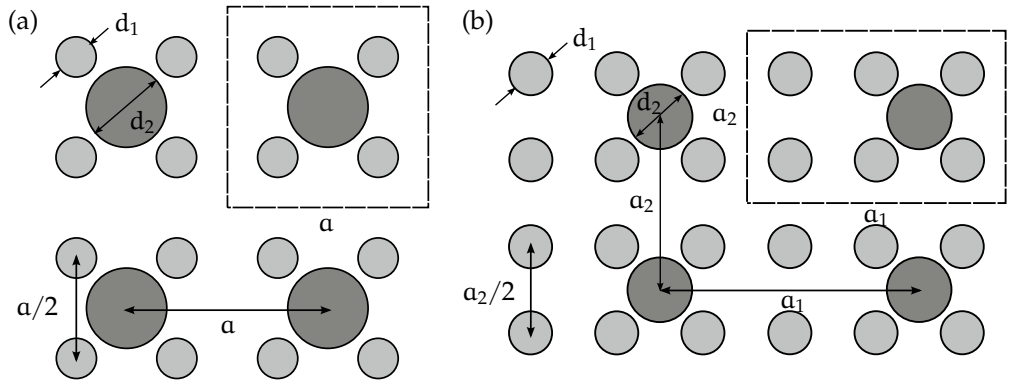

Figure 5.6: Diagram showing compound hole arrays. The region inside the dashed line corresponds to the compound hole array unit cell. A primary square array (light gray) is combined with a larger secondary array (dark gray) having (a) square and (b) rectangular symmetry.

and their geometrical parameters summarized in Tab. 5.1, namely sample A and B being square (see Fig. 5.6(a)) and sample C (see Fig. 5.6(b)) being rectangular.

Table 5.1: Geometrical parameters of compound hole arrays according to diagrams in Fig. 5.6

Sample label	d_1/a_2	d_2/a_2	h/a_2	a_1/a_2
A	0.25	0.375	0.375	1 (square)
B	0.2	0.4	0.5	1 (square)
C	0.25	0.375	0.375	1.5 (rectangular)

Calculating τ as a function of the normalized frequency $\omega a/\pi c_0$ and the parallel-to-plate wavevector $\mathbf{Q}_0$, Figs. 5.7 and 5.8 are obtained. In contrast to the simplicity found in [61] when studying the angular dependency of τ, a complex interplay between Wood anomaly minima, resonant interference minima and resonant full transmission is observed in the transmission dispersion plots from Figs. 5.7 and 5.8. Identifying the contribution of each array (primary and secondary) to the Wood anomalies is not an easy task. Therefore, the right side plots of Figs. 5.7 and 5.8 are the same than those at the left side with the inclusion of Wood anomaly curves of the primary (white) and secondary array (black). This redundant information is, however, helpful to distinguish resonant interference minima from common Wood anomalies.

In agreement with the normal incidence observation from Fig. 5.4, the prevalence of the transmission peaks over the Wood anomaly minima is evident also when the

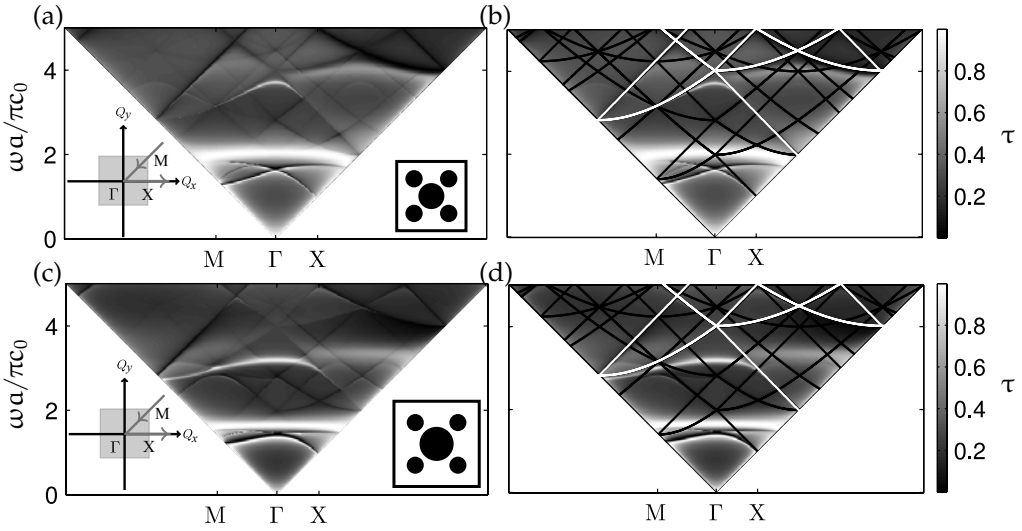

Figure 5.7: Transmitted sound power coefficient τ as a function of the normalized frequency $\omega a/\pi c_0$ and the parallel-to-plate wavevector $\mathbf{Q}_0$ along the directions of the first Brillouin zone showed in the left insets of (a) and (c) for samples A and B respectively. In (b) and (d) Wood anomaly curves of the primary (white) and secondary (black) arrays are added to the plots (a) and (c).

incidence angle is varied. The interaction of the first order Fabry-Perot full transmission peaks can be observed when $\omega a/\pi c_0 < 2$. For samples A and B (Fig. 5.7), the transmission maxima originated by the secondary array (first order Fabry-Perot) are flanked by the secondary array Wood minima (black curves), whereas the first order transmission peak provided by the primary array is nearly flat, is located a slightly higher frequencies, and clearly overcomes the secondary array Wood minima (black curves). This can explain the angle dependence of the resonance interference which is different from that reported in [61] because the case analyzed here involves the Wood minima as well.

The secondary array Wood minima (black curves) have only little influence in the second order transmission peaks coming from the primary array, which are still flanked by primary Wood minima. From the point of view of the reciprocal space, the primary array is just a subset of the secondary array, thus the Wood anomaly minima of the primary array are also a subset of that of the secondary array. These features remain even when the secondary array is rectangular, as shows Fig. 5.8. The transmission dispersion for sample C is calculated following the path in the reciprocal space depicted in the insets of Fig. 5.8(a) and (c). When the Wood minima curves are added to the

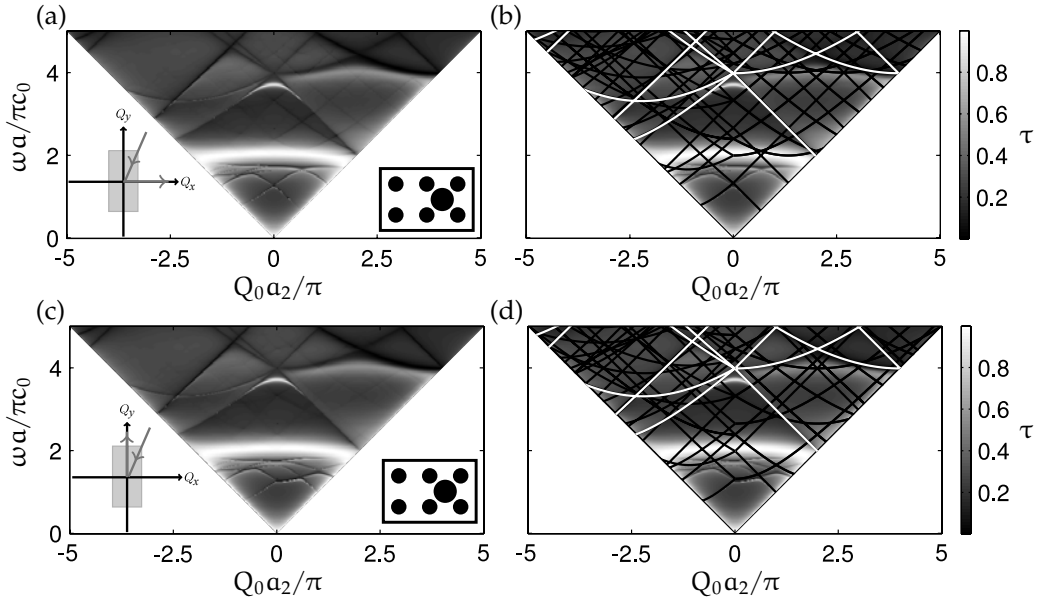

Figure 5.8: Transmitted sound power coefficient τ as a function of the normalized frequency $\omega a/\pi c_0$ and the parallel-to-plate wavevector $\mathbf{Q}_0$ along the M and X directions of the irreducible Brillouin zone. In (b) and (d) Wood anomaly minima are added to the plot for the primary (white) and secondary (black) arrays.

plot (Fig. 5.8(b) and (d)) it is clear that the interplay between Wood minima, resonance interference, and transmission peaks is more complex than for samples A or B.

5.3 Extraordinary sound screening

5.3.1 Perforated plate in water medium

When no holes are drilled, the sound transmission for normal incidence at low frequencies can be approximated using the mass-law [80] given by

$$\tau \approx \left(\frac{2\rho c}{m'' \omega} \right)^2 , \tag{5.4}$$

where $m'' = \rho_s h$ is the mass per unit area of the plate. This law states that heavier walls shield sound better than lighter ones. Thus, an increase in the plate mass produces a decrease in the sound transmission. However, in opposite to the common sense and the mass law, PPPs can transmit less sound than homogeneous plates having less mass. Figure 5.9 shows the transmission spectra of several aluminum plates perforated with square arrangements of holes immersed into water having different geometrical parameters (diameter d, period a, and thickness h in millimeters) under normal incidence. Perforated plates shield sound much better than non perforated ones when $\lambda \approx a$. For wavelengths larger than the periodicity, hole resonance appears leading to high transmission values. The transmission dip is located at the same place for both plates with $a = 5$ mm, while the plate with $a = 6$ mm shows the dip at larger wavelengths.

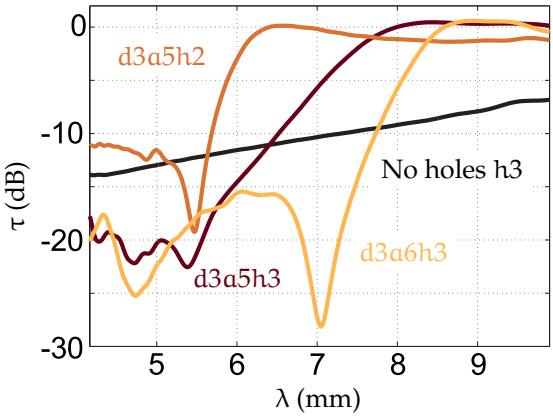

Figure 5.9: Measured transmission spectra of PPPs having square lattice symmetry immersed in water at normal incidence for aluminum plates with different geometrical parameters, as indicated by labels (in millimeters).

5.3.2 The role of the fluid-solid impedance mismatch K. Hydrodynamic short-circuit

When first reported [55], extraordinary sound screening was thought to exclusively rely on the Wood anomaly minima. Then, it could have been easily scaled up or down due to the purely geometric nature of Wood anomalies. However, it has been recently shown [56] that the phenomenon is more complicated and could be even more impressive due to the crucial role that plays the impedance mismatch K in the fluid-solid coupling.

Figure 5.10 reveals the key role of K for slit arrays compared to homogeneous plates. The sound power transmission coefficient τ in (dB) has been calculated as a function of the normalized frequency fa/c_0 at normal incidence. The features described in several papers [46, 48, 49, 47, 51, 55] assuming a perfectly rigid-solid ($K \to \infty$) appear almost unchanged for $K = 15$. Resonant full transmission and the Wood anomaly can be observed for $K = 15$ and $K \to \infty$ at $fa/c_0 = 0.6$, 0.99 and $fa/c_0 = 1$ respectively. However, when $K = 8$, huge unexpected transmission dips appear. In order to retain a more global picture of the effect of K, it has been varied between $2 \leqslant K \leqslant 15$ following five different slopes $m = (c_l/c_0)/(\rho/\rho_0)$ (see appendix B.1 for more details).

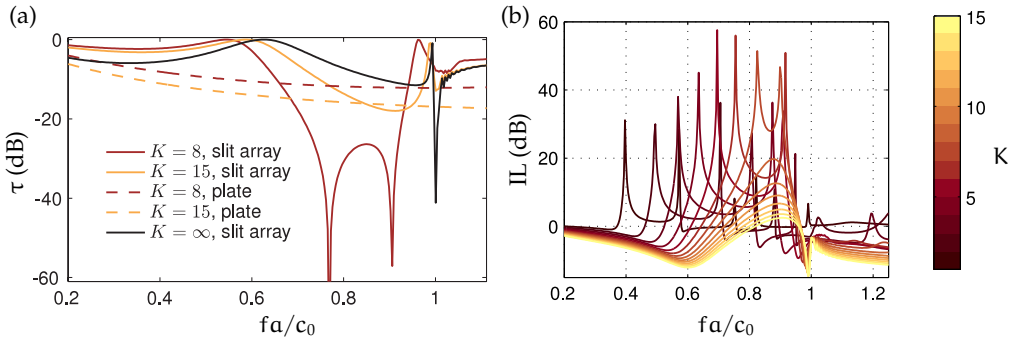

Figure 5.10: (a) Transmitted sound power coefficient τ in dB as a function of the normalized frequency fa/c_0 for slit arrays and homogeneous plates having different K. (b) Insertion loss in dB of slit arrays in a homogeneous plate as a function of the normalized frequency and different K for $m = 1.00$.

In addition to ρ and c_ℓ, which define the characteristic impedance z_0, also the transverse wave velocity c_t in the solid needs to be taken into account. In these calculations it is chosen as $c_t = 0.7c_l/\sqrt{2}$, thus satisfying $c_l^2 - 2c_t^2 > 0$.

The transmission features in Fig. 5.10(b) evolve with the decrease of K in agreement with what is reported here for aluminum perforated plates immersed in water ($K \approx$

11.8, $c_t/c_0 \approx 2$) and the theoretical prediction in [151] for PMMA perforated plates in water (K $\approx$ 1.8, $c_t/c_0 \approx 0.7$) (see appendix B.1 for more details).

The physical origin of this phenomena can be understood by comparing the pressure and displacement fields for finite and infinite K values, as it is shown in Fig. 5.11 when a plane wave coming from the left side impinges on the slit array.

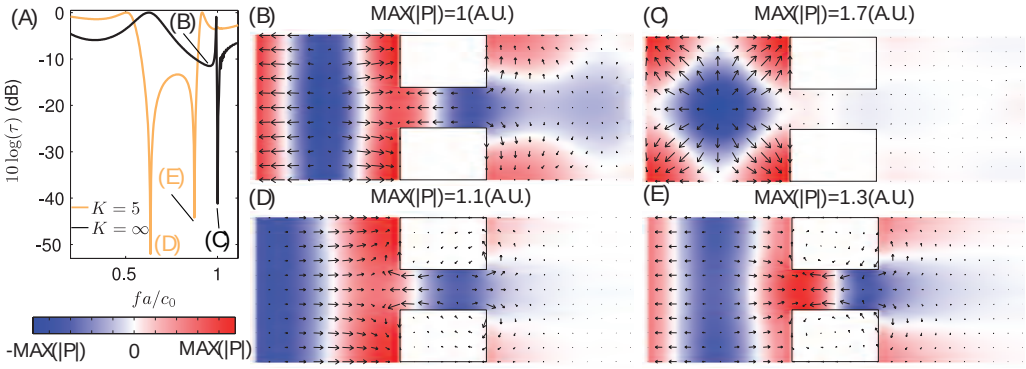

Figure 5.11: (a) Transmitted sound power coefficient in (dB) for slit arrays of different K as a function of the normalized frequency at normal incidence. For each peak indicated by the labels (b)-(e), the pressure (color scale) and displacement (arrows) fields are shown at the slit-array unit-cell. The incident wave travels from left to right having the same amplitude in all cases. Differences in the range of the color scale arise due to the existence of constructive interference in the pressure field. Arrow scaling is also different for each plot.

Two points for each transmission curve in Fig. 5.11(a) corresponding to K $= 5$ (light curve) and K $\to \infty$ (black curve) are shown and labeled in Figs. 5.11(d)-(e). The moderate transmission of -12 dB obtained for K $\to \infty$ at $fa/c_0 = 0.95$ is distinguishable from Fig. 5.11(b). Some portion of the incident wave coming from the left passes through the slit and is transmitted to the right. The interfaces at the right side of the solid cannot move, i.e. they act as a rigid baffle. This behavior differs from that of the Wood anomaly minimum at $fa/c_0 = 1$ (see Fig. 5.11(c)). As expected, the incident wave is almost completely reflected at the left side of the array, precluding the wave to enter into the slit. Thus, even if the plate thickness is enlarged up to infinity [39], the same phenomena occurs. On the other hand, when K $= 5$ the solid can vibrate and it couples to the fluid. How this coupling contributes to decrease the transmission through the slit array can be inferred from Figs. 5.11(d) and 5.11(e), which correspond to the minima in Fig. 5.11(a) at $fa/c_0 = 0.64$ and $fa/c_0 = 0.87$ respectively. At first glance, the fields for K $= 5$ are more similar to those of Fig. 5.11(b) than to the Wood anomaly ones. However,

in these cases the incoming wave penetrates not only into the slit, but also into the solid in such a way that the outward displacement at the slit right side is compensated by the inward displacement of the solid right face. Thus, an evanescent wave appears at the transmitted side of the slit array, yielding sharp dips beyond -40 dB in transmission.

This phenomena, is well known in the sound radiation of structures and it is called hydrodynamic short-circuit [100]. Also the field inside the slit is affected by the solid deformation. Small gradients in the vertical direction distort the otherwise straight displacement field.

To further understand the differences between both transmission minima for $K = 5$, we can analyze time averaged quantities related with the sound radiation as the sound intensity normal to the aperture at the right side of the slit array unit cell (see Fig. 5.12 (a)).

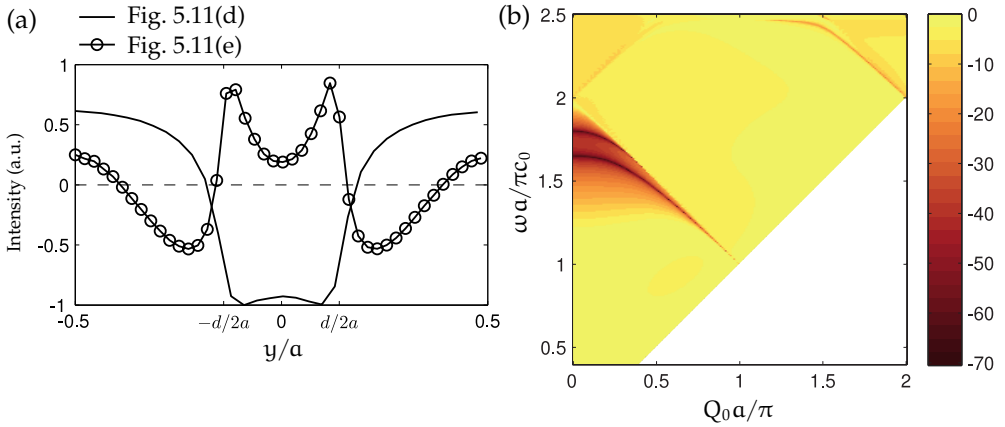

Figure 5.12: (a) Time averaged intensity normal to the aperture at the right side of the slit array referred to Fig. 5.11(d),(e) as a function of the normalized vertical coordinate y/a. The slit is centered at $y/a = 0$ and the positive side of the intensity point outwards the slit. (b) Transmitted sound power coefficient τ dispersion of a slit array for $K = 8$ (color scale in (dB)) as a function of the parallel wavevector $\mathbf{Q}_0 a/\pi$ and the normalized frequency $\omega a/\pi c_0$.

Surprisingly, at the first minimum (regarding Fig. 5.11(d)) the solid is attempting to transmit energy to the fluid, but the fluid within the slit inhibits it, resulting in a overall sound blocking effect, as shown at the minimum (d) of the Fig. 5.11(a). The intensity at the second minima (regarding Fig. 5.11(e)) behaves in the opposite way, mainly concentrated at the edges of the slit. This shape is presumably induced by the solid deformation because the cavity sustains a standing wave and little energy is carried

through the slit. In addition, the intensity at the solid presents more gradients due to the shorter wavelength of the incoming wave.

Previous results for normal incidence can be broadened considering non zero parallel to the array wavenumber Q_0. The sound power transmission coefficient τ is shown in Fig. 5.12 (b) for $K = 8$ as a function of Q_0 and k_0. Dark regions below the Wood anomaly given by $k_0 = 2\pi/a - Q_0$ correspond to low transmission zones where both dips can be distinguished. Thus, an acceptable angular window of low transmission is provided.

The non-trivial behavior presented here is even more outstanding than the already counterintuitive possibility of screening sound with slit (hole) arrays. The lowest transmission is not achievable with the highest impedance ratio, but with an optimum K. This results are consistent through the whole set of parameters included in this study (see appendix B.1).

As the impedance ratio for most solids in air is at least three orders of magnitude larger than those considered for this study, slit array sound screening is not suitable for airborne sound [56]. The physical mechanism involved in the transmission dips differs from the Wood anomaly. The solid vibrations allow normal intensity oscillation at the transmission face of the array, which produces very low radiated sound power.

The existence of an optimum impedance ratio to obtain TLs up to 60 dB using slit arrays opens the door for a wide range of possible applications mainly in underwater acoustics and underwater ultrasound. For sonar applications it could be used as a reflector either to block signals coming from unwanted sources or for redirecting the launched sonar signal. In this aspect, a slit array can be a better option over a solid surface or a holey plate because of its hydrodynamic characteristics. Some similar applications, but at a smaller scale, could be thought as well for underwater ultrasound.

5.3.3 Sound screening for airborne sound

One key issue in hole-array sound screening is whether it can be applied for the case of airborne sound at audible frequencies [152, 153, 154]. Other approaches using periodic structures having air resonant cavities have been proposed [155, 151, 59, 60]. Hannink et al. [155] attempted to build a thin shell structure for airborne sound insulation purposes by means of $\lambda/4$ resonator (hole closed at one end). The flexural coupling was as important as the random incidence and the high TL obtained in Kundt tube experiments could not be repeated in transmission chamber ones. The theoretical predictions under the rigid-solid assumption [151, 59, 60] propose a double layer of periodically perforated structures, although no realistic comparison neither with single wall nor with double homogeneous wall are given.

To illustrate the difficulties one could face when translating underwater ultrasound phenomena to audible airborne sound, a simple numerical example calculated with the FEM is given. Suppose a concrete wall ($\rho = 2400$ kg/m^3, $c_l = 2996$ m/s) in air ($\rho_0 = 1.12$ kg/m^3, $c_0 = 343$ m/s) whose impedance mismatch yields $K = 1.7 \times 10^4$. Lets now calculate if drilling holes or slits in the wall could produce an improvement in the TL (TL$= -10\log(\tau)$).

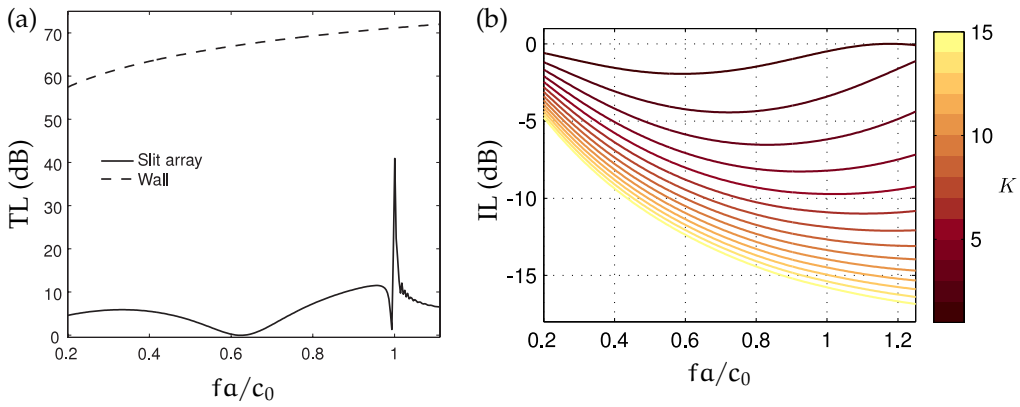

Figure 5.13: (a) Transmission loss in dB for a slit array (solid curve) and a homogeneous wall (dashed curve) both made of concrete in air as a function of the normalized frequency at normal incidence. (b) Insertion loss in dB of slit arrays in a fluid layer as a function of the normalized frequency for the different values of K.

The results of this high impedance mismatch in the TL of the slit array compared with the homogeneous wall of the same thickness and material are shown in Fig. 5.13(a) as a function of the normalized frequency fa/c_0 at normal incidence. Resonant full transmission peaks and the Wood anomaly are present in the slit array spectrum, as expected from previous results using rigid-solid assumption [46, 48, 49, 47, 51, 55]. It is clear that the slit array does not provide any advantage at any frequency in terms of TL over the homogeneous wall as its TL (dark solid curve) is nearly 55 dB below than that of the homogeneous wall (dashed curve in Fig. 5.13(a)). The previous results preclude the use of the slit array sound screening in airborne conditions due to the huge impedance mismatch between the air and most solids ($K > 10^3$) and this restriction is almost certainly valid also for hole arrays.

The possibility of overcoming the homogeneous plate TL by inserting slits in a low impedance material is unfortunately not realistic for airborne sound because no conventional solid has such a low acoustic impedance to reach $K = 8$. Replacing the

solid by a fluid , i.e. another gas, could be more feasible in the practice to achieve the low K required to obtain high TLs. Following the FEM calculation scheme used for a slit array in a solid slab, the Insertion Loss (IL) of a slit array in a fluid layer is calculated for different K values as a function of the normalized frequency fa/c_0 and shown in Fig. 5.13(b). It can be clearly observed that the IL is almost always negative. Then, as our calculation predicts, it would be useless to replace the solid by a fluid in order to attain high TL in airborne sound.

These encouraging results seemed to block not the sound but the previous naïve assumption of easy translation between waterborne and airborne sound phenomena. There are, however, porous materials capable of showing low impedance and certain amount of sound absorption as well. This kind of materials could be suitable candidates to show interesting properties when they are arranged periodically, as several authors have reported in previous studies for airborne sound [156, 157]. Porous materials are, however, more complex and are out of the scope of this study. Also low impedance metamaterials [158] working in the effective media regime could be appropriate to provide the low impedance mismatch required but further research is required to address this question.

5.4 Surface waves

A more global picture is obtained when the angle of incidence is varied. Although for normal incidence one could simply rely on the RSM prediction plus a few considerations as the step-like behavior, the angle dependent measurements clearly depict a different scenario for which RSM does not provide a convincing explanation.

Figure 5.14 shows the results of angle dependent measurements for two different lattices (square and triangular). The color scale corresponds to τ in (dB) as function of the parallel wavevector within the irreducible Brillouin zone and the normalized incident frequency $\omega a/2\pi c_0$. Three different plate thicknesses were measured for square and triangular arrays drilled in aluminum plates immersed in water.

Complex interaction between minima and maxima is present in the spectra and it makes clear that the symmetry of the array results in a high angular dependence of the spectra [67]. In Figs. 5.14 (a)-(f), Wood anomalies are depicted in the transmission dispersion as white dashed curves. There is a very good agreement between the measured position of the minima and the prediction of Eqs. (5.2) and (5.3) when the thickness of the plates is small. However, the dips appearing from the bottom of the figures are not predicted by the Wood anomaly and can be related to leaky surface modes, whose phase velocity can be measured. This surface modes resemble leaky Lamb modes observed in the homogeneous plate (see Fig. 2.3) arising from the plate vibration and the solid-fluid

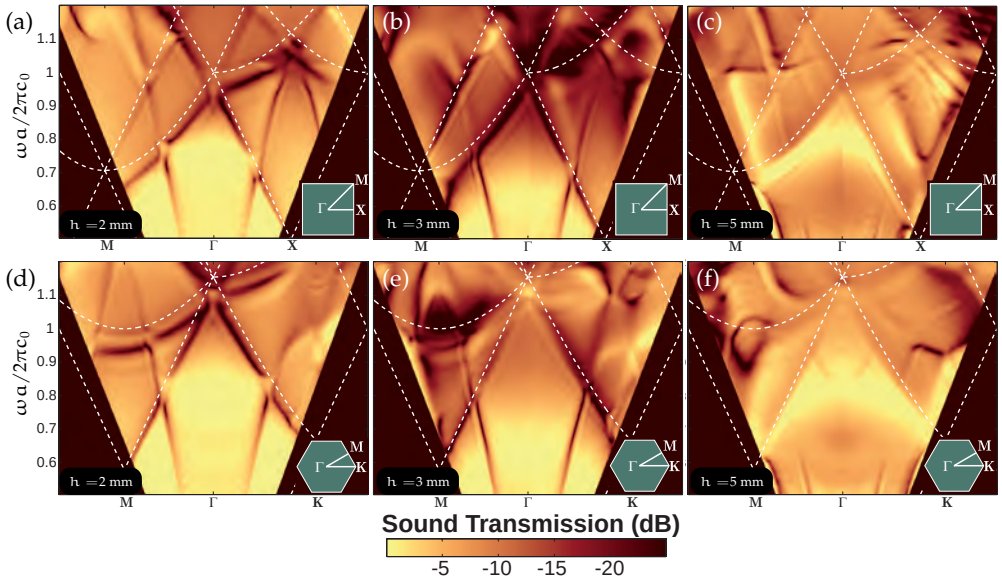

Figure 5.14: Measured sound transmission as a function of the parallel wavevector $\mathbf{Q}_0$ and the normalized frequency $\omega a/2\pi c_0$ for periodically perforated aluminum plates with square (a)-(c) and triangular (d)-(f) lattice symmetry (see insets), and for different plate thicknesses h. The period is $a = 5$ mm and the hole diameter is $d = 3$ mm for all cases. White dashed curves correspond to Wood anomaly modes. Around 720 measurements are condensed in this figure.

coupling. Indeed, it has been found that the geometrical anisotropy of the arrays leads to anisotropy of the modes phase-velocity [68] even if the solid is isotropic (aluminum in this case).

One can actually extract the phase velocity c_S of the S_0-like mode below the crossing with the Wood anomaly by fitting a linear dispersion at low frequencies. The results (see Tab. 5.2) reveal the importance of plate thickness and orientation of $\mathbf{Q}_0$. For both types of lattices, the phase velocity decreases when the thickness increases from 2 to 3 mm. Moreover, the S_0-like mode travels faster through the ΓX direction with square lattices, and through the ΓM with triangular lattices. For thicker plates, the bands evolve in a complex way which prevents us from extracting accurate values for the group velocity within the frequency range of our measurements.

Considering the RSM results in Fig. 5.5 one should conclude that this model does not predict the existence of leaky surface modes because in its derivation it is assumed that $K \to \infty$ neglecting the plate vibration and the fluid-solid coupling, both essential for the observation of leaky Lamb waves in homogeneous plates. A theory that takes into

Table 5.2: Phase speed c_S for the S_0-like mode below the crossing with the Wood anomaly for both square and triangular lattices.

h (mm)	Lattice	Direction	c_S (m/s)
2	square	ΓX	3495 ± 33
		ΓM	3020 ± 27
2	triangular	ΓK	2994 ± 22
		ΓM	3521 ± 9
3	square	ΓX	3150 ± 48
		ΓM	2748 ± 23
3	triangular	ΓK	2747 ± 22
		ΓM	3217 ± 35

account the plate vibrations and the solid-fluid coupling is then needed. One option is the use of the FEAM, which has been derived before. Comparing the results of the three theories, namely the homogeneous plate, the rigid-solid, and the FEAM, with the experimental results we obtain Fig. 5.15. The sound power transmission τ is depicted in color scale as a function of the parallel wavevector along the ΓX direction and the normalized frequency $\omega a/\pi c_0$. Plates having three different h/a ratios but sharing the same filling fraction ($f_\square = 0.28$) are shown.

In the homogeneous-plate calculations, the normalization by the lattice period a in both axis is only used to have the same scale as the other contour plots. The first row shows the transmission dispersion for the homogeneous plate, dominated by the cutoff-free symmetric and antisymmetric leaky Lamb modes, the latter mixed with the Scholte-Stoneley mode for $h/a = 0.2$, 0.4 near the $\omega = c_0 Q_0$ line (c_0 is the sound phase velocity in water). Each of this three images represents a magnified version of the complete behavior of aluminum plates immersed in water given in Fig. 2.3, which is valid for plates of any thickness. Higher order modes enter in the frequency range when the plate thickness is increased (see $h/a = 1.0$).

The second row contains the sound transmission dispersion calculations of PPPs under the rigid-solid assumption. Full transmission peaks arising from the hole resonances and hybridized with the Wood anomaly dips are observed. The peak is quite narrow when $h/a = 0.2$ and is placed immediately below the Wood anomaly. The transmission peak is then moved to lower frequencies by increasing the h/a ratio and higher order FPRs enter into the frequency range.

The third row shows the calculations obtained with the FEAM, which includes the

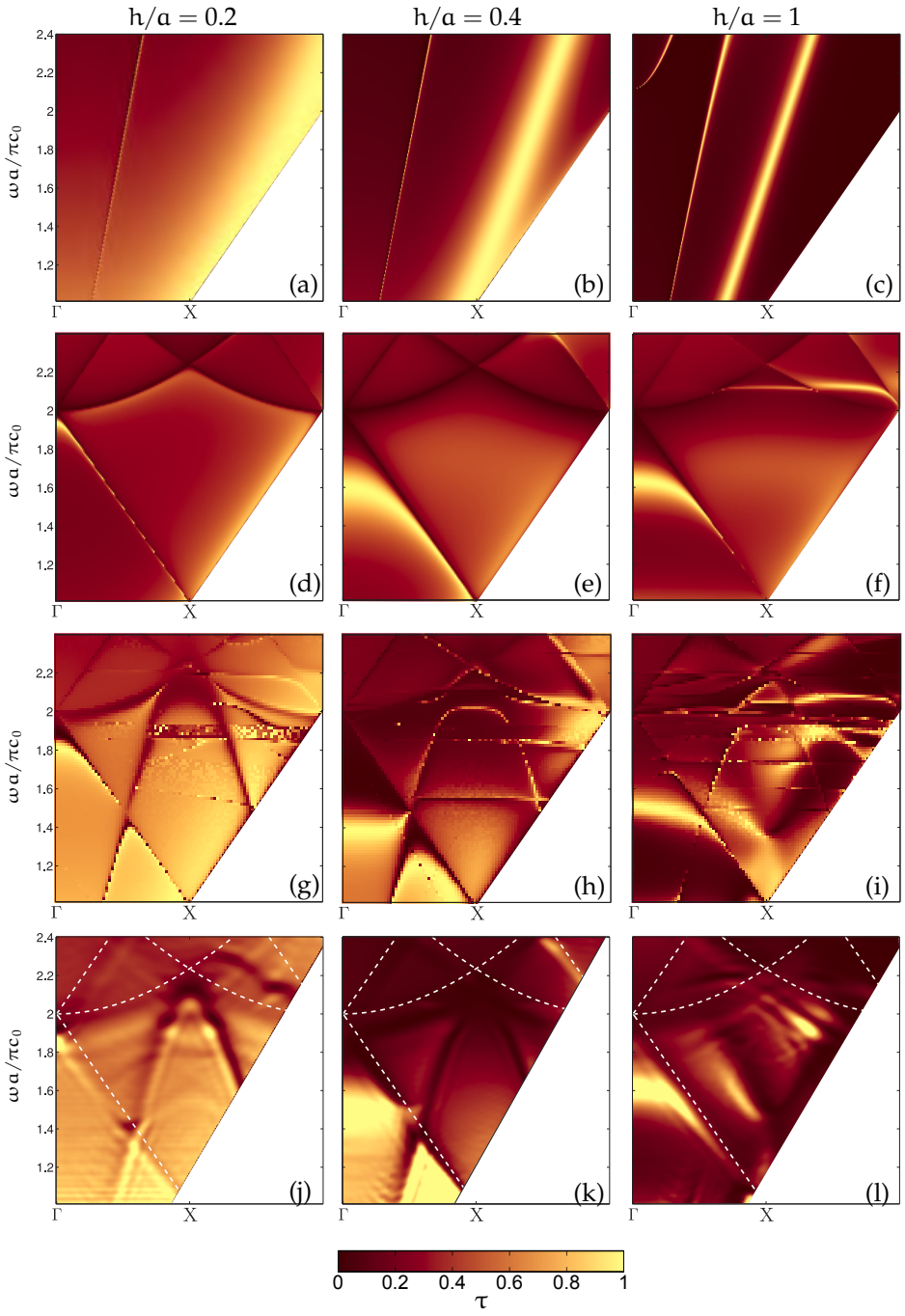

Figure 5.15: Comparison of the transmitted sound power τ between the different theoretical models and the measurements for square arrays ($f_\square = 0.28$) in the ΓX direction as a function of the normalized frequency $\omega a/\pi c_0$. Top row corresponds to homogeneous plate calculations, followed by the rigid-solid prediction row and the FEAM prediction row. Finally, the bottom row shows the experiments. Wood anomalies are depicted as white dashed curves in the measurements row.

hole resonances, coherent scattering due to the hole array, and the elastic vibrations of the plate. These three phenomena are responsible of the complex transmission dispersion obtained in the measurements (see fourth row of Fig. 5.15). In spite of the numerical instabilities observed in the results of the FEAM, the main features regarding the finite impedance mismatch between solid and fluid can be properly resolved. When $h/a = 0.2$, the FEAM correctly predicts a dip arising from the bottom of the dispersion plot reaching zero group velocity at the X point and falling down again due to symmetry around X. Adding the rigid-solid results to the comparison enable us to infer that this dip corresponds to a surface mode similar to Lamb modes, i.e. caused by the plate vibrations. The high transmission region measured at low frequencies, which is delimited by the leaky surface mode and a Wood anomaly, is also properly predicted by the FEAM, in opposite to the RSM.

A similar landscape is obtained for $h/a = 0.4$. The crossing between the Wood anomaly and the surface mode can be clearly seen in both, the experiment and the FEAM results. This crossing is particularly interesting because there coexist the leaky surface mode, the Wood anomaly, and the transmission peak, all of them hybridized. The high transmission found below this crossing is connected with the step-like behavior observed at normal incidence (see Figs. 5.2 (a), (b), (d), and (e)). This behavior has been correctly attributed to the effect of the finite impedance mismatch K, which is taken into account in the FEAM. The full transmission peak is also affected by the plate vibration with a small shift towards lower frequencies. For thicker plates ($h/a = 1.0$) the interaction between surface modes, coherent scattering among holes, and hole resonances is stronger, producing a rich and complex scenario, and further investigation is needed to unveil the complex interplay. These results show clearly how the fluid-solid coupling mixes two phenomena that had been studied separately, namely sound transmission through perforated plates and elastic wave propagation through phononic plates.

Slits and holes produce a different behavior when light is transmitted through them. However, in the case of sound they behave in the same way unless the fluid-solid coupling reaches finite values. Calculating numerically the transmission dispersion for a slit array, we arrive to Fig. 5.16. Three different models are depicted for three slit arrays of the same filling fraction $d = 0.28a$ and three slab thicknesses (from top to bottom $h = 0.6a\,, a\,, 1.6a$). The left columns shows the results of the two-dimensional RSM ($K \to \infty$) followed by the central column showing the FEM results for $K = 8$, and $m = 1$. Finally, the transmission dispersion of the homogeneous plate having the same thickness and material as the FEM simulated slit arrays is also provided for comparison at the right column.

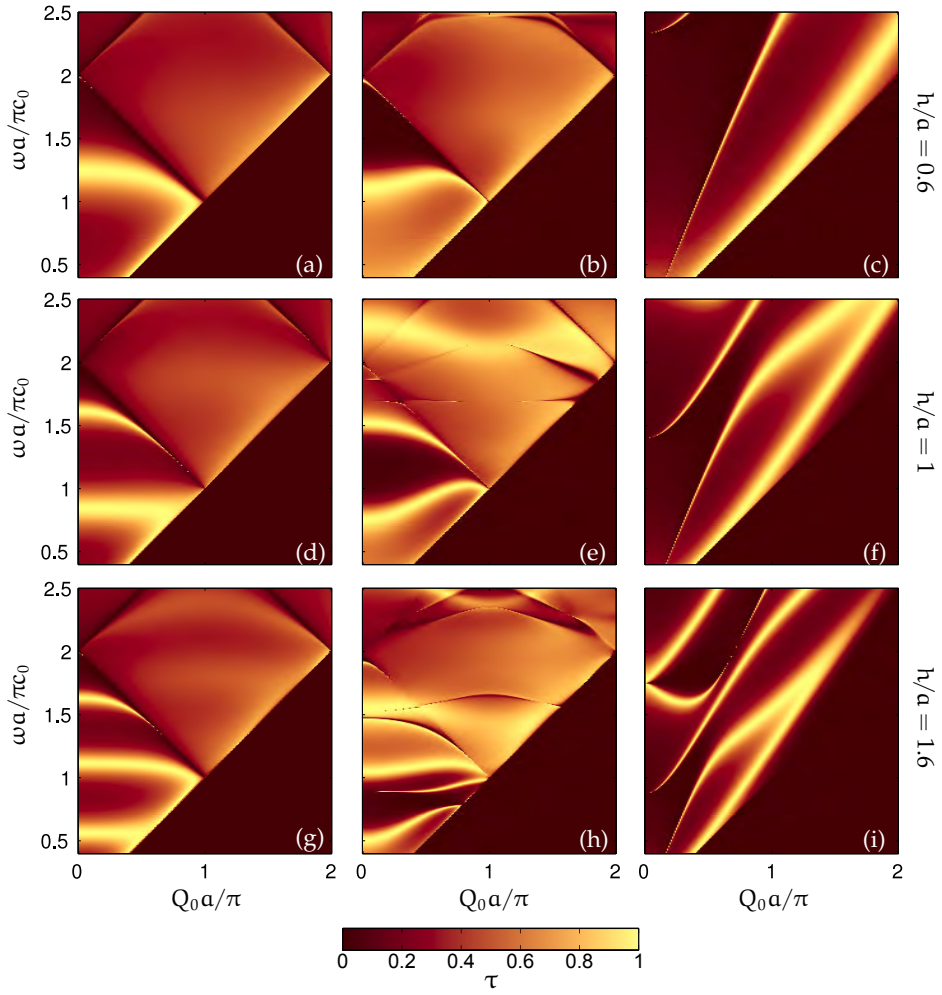

Figure 5.16: Comparison of the transmitted sound power τ (color scale) between the different theoretical models for slit arrays as a function of the parallel wavevector $\mathbf{Q}_0$ and the normalized frequency $\omega a/\pi c_0$. The left column corresponds to the RSM, the central to FEM approximation, and the right to the homogeneous plate. Each row corresponds to one h/a ratio, as indicated by the labels at the right. The impedance mismatch is $K = 8$ in the FEM and the homogeneous plate calculations.

As the periodicity is one-dimensional, Wood anomaly minima are far simpler than the previously considered cases. Looking at the thiner slit array results (Fig. 5.16(a)-(c)), the resonant transmission peak, which appears in the rigid-solid case, is pushed to

lower frequencies by the low transmission zone that appears right above when $K = 8$ in Fig. 5.16(b). One key difference between slit and hole arrays for finite impedance ratio is evident from Fig. 5.16(b) contrasted with the experimental and theoretical results of Fig. 5.15. No zero-order leaky surface modes appear for slit arrays because the solid slabs do not have elastic connection between them as a perforated plate does. As can be observed in the transmission dispersion of the thicker slabs, only the higher order Lamb modes seem to interact with the periodicity and the slit resonances, adding more features to the finite K dispersion. In addition, slit arrays having $h = 0.6a, a$ clearly show a step-like behavior near normal incidence.

To make clearer the key role of the symmetry in the transmission properties of perforated plates we can compare a periodic lattice with a random lattice, both having the same filling fraction (average hole filling fraction $\bar{f}$ for the random array) and sharing the same plate thickness. This comparison is shown in Fig. 5.17, where the upper panels (a) and (b) correspond to transmission dispersions while the lower panels (c) and (d) represent the two-dimensional Fourier transforms of both lattices.

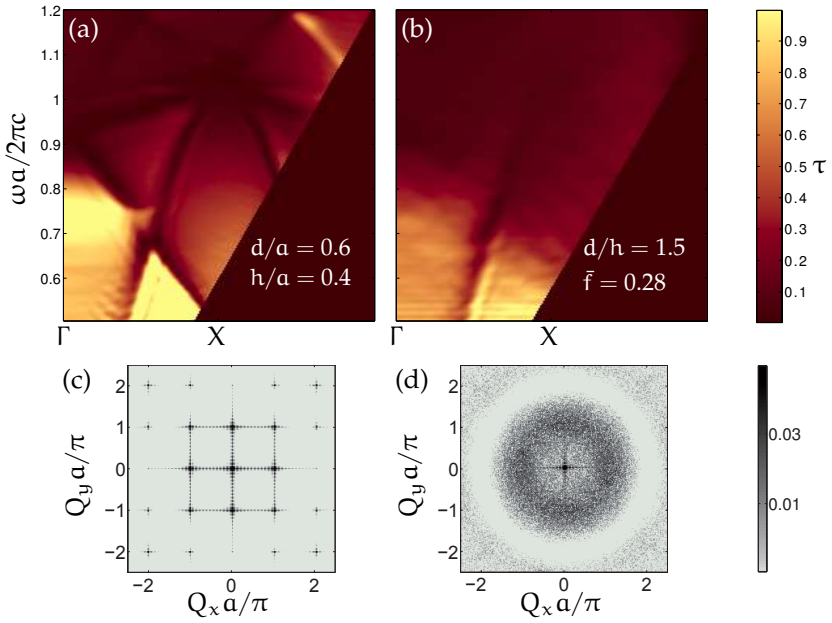

Figure 5.17: Transmitted sound power τ (color scale) through perforated plates as a function of the normalized frequency $\omega a/\pi c_0$ and $\mathbf{Q}_0$ along the ΓX direction of the irreducible Brillouin zone for square (a) and random (b) lattices. (c), (d) two-dimensional Fourier transforms (contour plots in log scale) of the holes for the (c) periodic and (d) random arrays.

The rich interplay between lattice modes and intrinsic plate modes in the ordered array (Fig. 5.17 (a)) is completely absent in the random sample. However, the latter displays a feature resembling the surface mode coming from the plate vibration without the fall due to the array symmetry around the X point.

Interestingly, the Fourier transform of the two-dimensional distribution of geometrical openings in random arrays shows a broad annular maximum with a radius close to $|\mathbf{Q}| = \pi/a$. This maximum gives rise to a broad dark region near normal incidence, close to the Wood anomaly of the ordered array. Regarding the transmission peak, it is reduced nearly to a half for the random lattice at normal incidence, while the high transmission observed near to the X point at low frequencies is mainly due to the plate vibration and not to the hole resonance.

5.5 Solid-solid phononic plates immersed in water

The wave behavior of a solid can differ enormously from that of a fluid. Moreover, the wave interaction at a solid-solid interface is different from that of a fluid-solid interface. As the fluid only supports longitudinal vibrations, the stress tensor reduces to a scalar, i.e. the fluid pressure ($\sigma_{ij} = -p\delta_{ij}$), when viscous effects are neglected. Thus, a different behavior in the transmission properties of perforated plates is expected if the holes are filled with another solid. Two different polymers have been employed to fill the holes drilled in aluminum plates due to it elastic constants, which are close to that of water.

In the following pages it will be shown that the FEAM works flawlessly when the PhPs constituents are both solids. No spurious modes appear as a result of the eigenvalue problem.

Figure 5.18 depicts the experimental (a) and numerical (b) transmission dispersion of PMMA cylinders of $d = 3\,\text{mm}$ arranged periodically in a square lattice of period $a = 5\,\text{mm}$ embedded in an aluminum plate having $h = 3\,\text{mm}$ and immersed in water. Below the sound line, the normalized evanescent transmission is plotted. This normalized transmission reaches unity when a surface mode exists and it will be of great help in the analysis.

The calculations have been made considering $N_G = 97$ (reciprocal lattice vectors), $N_n = 3N_G$ (phononic plate eigenmodes), and nominal elastic constants for water, aluminum, and PMMA (see Tab. 5.3).

Zero order Lamb modes are clearly distinguishable from both pictures. On the one hand, the A_0 mode is broad and couples the surrounding fluid producing full transmission in the calculations and high transmission in the experiments. On the other hand, the S_0 mode preserves its less radiative nature, which shows up with very sharp

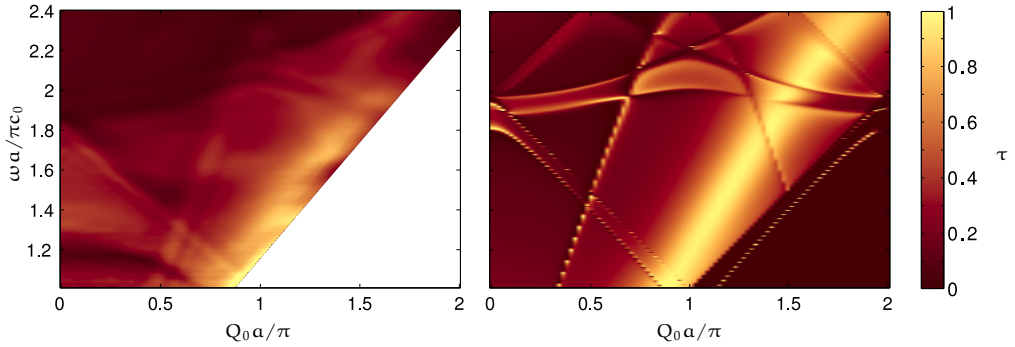

Figure 5.18: Transmitted sound power τ as a function of the parallel wavevector $\mathbf{Q}_0$ in the ΓX direction and the normalized frequency $\omega a/\pi c_0$ from (a) measurements and (b) FEAM calculations for an Al-PMMA PhP immersed in water. The geometrical parameters of the square array are $d = 3\,\text{mm}$, $a = 5\,\text{mm}$, and $h = 3$ mm.

Table 5.3: Elastic constants for aluminum and PMMA used in the calculation of Fig. 5.18(b).

Material	ρ (kg/m^3)	c_ℓ (m/s)	c_t (m/s)	β_ν
Al	2700	6467	3120	0
PMMA	1270	2770	1430	0
Water	1000	1480	0	0

features, and is affected by the symmetry of the array when $Q_0 > \pi/a$. Some modes resembling Wood anomaly minima seem to be doubled when $\omega a/\pi c_0 < 2$ by other two modes. Considering the information available from the calculations regarding non-leaky modes below the sound line (from points $(1,1)$ to $(2,2)$ in the dispersion space), one can observe the mirror image of the non-leaky mode reflected on the $Q_0 a/\pi = 1$ axis. It means that the non-leaky mode is folded due to the array symmetry. Thus, on the leaky side of the dispersion, the mode is characterized by a negative group velocity. The other mode, whose group velocity is low and develops near $\omega a/\pi c_0 = 2$, seems to be related to the folded continuation of the non-leaky mode.

There is a transmission minimum at low frequencies in the measurement which has not been predicted by the theory. It can be due to imperfections of the PhP (non homogeneous thickness due to the sanding process, defects in the PMMA filled holes) or the finite size effects of the measurement setup. However, the main obstacle to obtain better measurements is clearly the limited angular resolution of the immersion

transducers. As can be clearly seen in the theory, most features are very sharp and include abrupt changes of the transmission from $\tau = 0$ to $\tau = 1$ in a small frequency-wavenumber area.

Changing the polymer from PMMA to epoxy resin to fill the holes we obtain the experimental and numerical dispersion showed in Fig. 5.19. Transmission and Nearfield in-Plate Excitation Measurement (NiPEM) as a function of the parallel wavevector $\mathbf{Q}_0$ in the ΓX direction and the normalized frequency $\omega a/\pi c_0$ are compared with the FEAM transmission calculation, which includes the normalized evanescent transmission below the sound line. The NiPEM is required to measure the wave propagation right at the plate surface and thus, unveil the bounded modes predicted by the FEAM.

The elastics constants of both, aluminum and epoxy resin have been previously extracted from homogeneous plate measurements by fitting the theoretical angle dependent data to the measurement data. Attenuation was needed to properly characterize the epoxy resin. However, the measurements of the PhP showed a low frequency shift in comparison with the numerical calculations based on elastic constants measured on homogeneous aluminum and epoxy plates.

Table 5.4: Elastic constants for aluminum and epoxy used in the calculation of Fig. 5.19(b).

Material	ρ (kg/m^3)	c_ℓ (m/s)	c_t (m/s)	β_ℓ	β_t
Al_f	2683	6175	2900	0	0
$Epoxy_f$	880	2038	942	18×10^{-3}	22×10^{-3}

Table 5.5: Deviation of the elastic constants used in the calculation of Fig. 5.19(b) from the measured data of homogeneous aluminum and epoxy plates.

	ρ	c_ℓ	c_t	β_ν
ΔAl	+6%	+1%	−8%	0
ΔEpoxy	−23%	−20%	−18%	0

Then, a further step in the calculation was required. The quadratic error between experimental and numerical data was used as a minimization target and parameter variation is performed in the space of the elastic constants $(\rho_1, \rho_2, c_{\ell 1}, c_{\ell 2}, c_{t1}, c_{t2})$ without including the attenuation to keep the problem as small as possible. During this process, it was found that the thickness of the plate was no more $h = 1$ mm but $h \approx 0.85$ mm due to the sanding process to remove the epoxy over-layer.

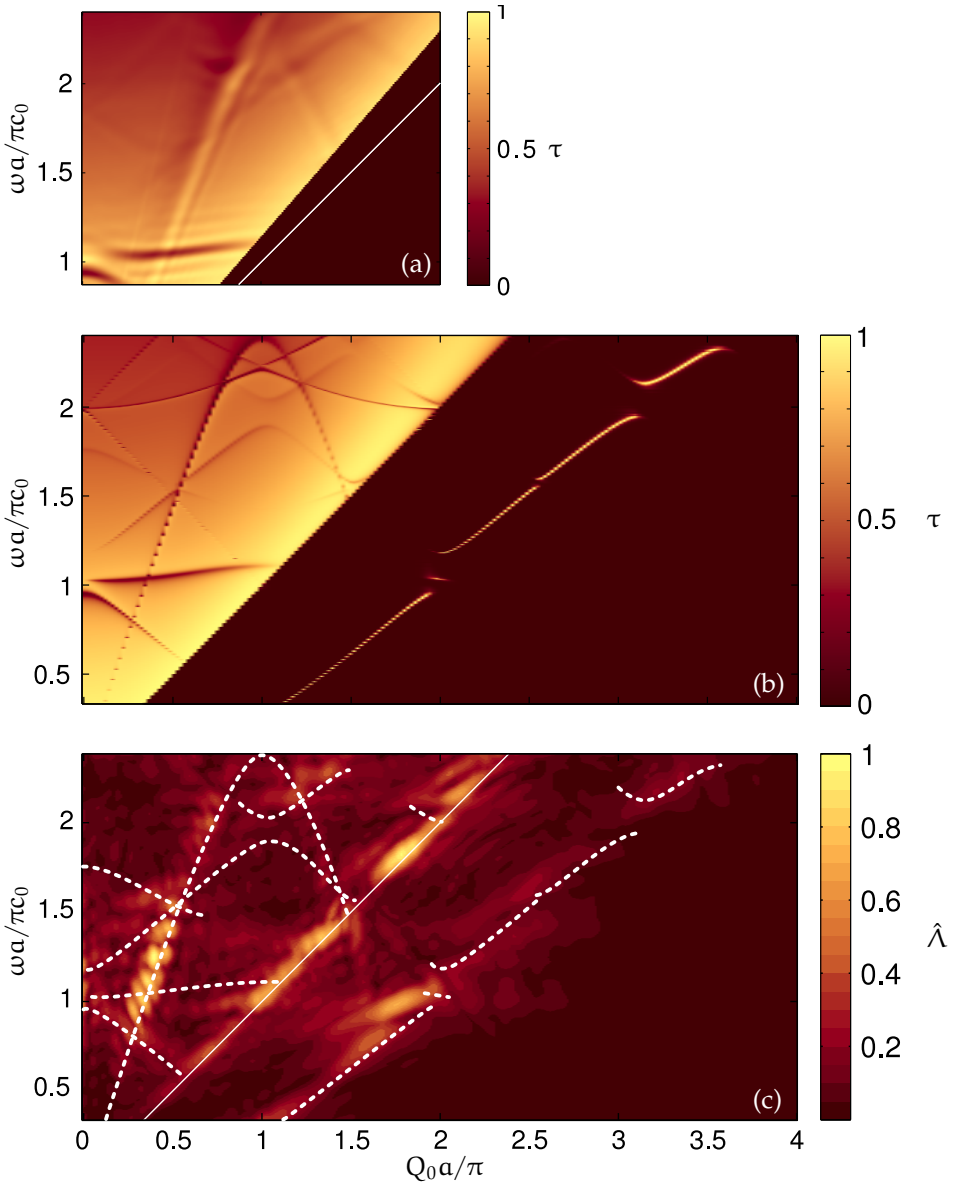

Figure 5.19: Transmitted sound power τ as a function of the parallel wavevector $\mathbf{Q}_0$ in the ΓX direction and the normalized frequency $\omega a/\pi c_0$ from (a) measurements and (b) FEAM model calculations for underwater Al-Epoxy PhP. (c) Near field dispersion measurement for the same PhP immersed in water, where the color scale corresponds to the normalized Λ defined in Eq. (4.3) and white dashed curves correspond to the features predicted by the theory. The geometrical parameters of the square array are $d = 2.5\,\text{mm}$, $a = 5\,\text{mm}$, and $h = 0.85$ mm.

Furthermore, the final elastic constants, which provided the lowest quadratic error, are written in Tab. 5.4 and its percentage deviation from the homogeneous plate extracted ones in Tab. 5.5. The deviations for aluminum are below 10% but, surprisingly, in the case of epoxy all elastic constants show a similar deviation in the same direction of around 20%. As described in subsection 4.3.1, the fabrication process is complicated and several factors can influence the final result.

Despite this issue, there is a good agreement between the theory (see Fig. 5.19 (b)) and the experimental results, not only for the leaky modes measured using the transmission measurement technique (see Fig. 5.19 (a)), but also for the NiPEM (see Fig. 5.19 (c)).

The transmission dispersion looks different from the PMMA-aluminum PhP not only because of the different geometrical parameters ($d = 2.5\,\mathrm{mm}$, $a = 5\,\mathrm{mm}$, $h = 0.85\,\mathrm{mm}$) but also because of the higher attenuation given by the epoxy resin. The features are smoother than in Fig. 5.18 for both, experiments and calculations. Wood anomalies are, however, too narrow to be detected.

The main feature observable from the transmission measurements are the minima around $\omega a/\pi c_0 = 1$. These minima are also predicted by the theory and they can be connected to a zero group velocity non-leaky mode. This is evident from both theory and NiPEM at $(Q_0 a\pi, \omega a/\pi c_0) \approx (2, 1)$ and the lower frequency branch which is folded onto the leaky side of the dispersion having negative group velocity when $\omega a/\pi c_0 < 1$.

In addition, the S_0-like mode can be clearly distinguished from the three sub-figures including its symmetric branch having negative group velocity. As the plate is relatively thin, the A_0 like mode is difficult to visualize in the transmission because its broadness is mixed with the overall high transmission observed. As the A_0 should be localized near the sound line, a closer look into the NiPEM results clearly demonstrates its presence in the dispersion. Remaining modes seen in the transmission dispersion can be easily explained in terms of the folded non-leaky modes predicted by the FEAM and corroborated by the NiPEM. Following the white dashed curves in Fig. 5.19(c) taken from the theory in Fig. 5.19(b) one can observe not only the agreement between theory and experiment, but also the band folding phenomenon.

Non leaky modes show band gaps as well as a subsonic band with zero group velocity dispersion. To the best of our knowledge, this is the first time that this kind of modes are predicted and measured for non-corrugated PhPs.

The relation of these non-leaky modes with Scholte-Stoneley modes can be demonstrated by comparing the c_t/c_0 ratio between the lowest solid c_t of the different PhPs and the nominal speed of sound in water $c_0 = 1480\,\mathrm{m/s}$. For the Al-PMMA PhP this ratio reaches 0.97 whereas for the Al-epoxy PhP it gives 0.64. Comparing now Figs. 5.18(b) and 5.19(b) one can certainly link the distance of the modes to the sound line for a given

frequency to the c_t/c_0 ratio, which is consistent with the observations of wave propagation [150] in fluid-solid interfaces. A fluid-solid interface is governed by Rayleigh waves if $c_t > c$ and by Scholte-Stoneley waves if $c_t < c$. In our case, as we are dealing with PhPs which contains two different materials this condition is reflected in the distance to the sound cone of the non-leaky modes.

Table 5.6: Elastic constants for aluminum, nickel and PMMA used in the calculation of Figs. 5.21 and 5.20.

Material	ρ (kg/m^3)	c_ℓ (m/s)	c_t (m/s)	β_ν
Al	2700	6310	3130	0
Ni	8910	5910	3080	0
PMMA	1270	2770	1430	0

Provided that the FEAM can predict experimental results, more materials and geometrical parameters can be examined. Three different materials have been regarded as appropriate due to their elastic constants, namely aluminum, nickel, and PMMA. Four combinations of these materials have been considered, i.e. nickel plate decorated with aluminum cylinders (Ni-Al), aluminum plate having nickel inclusions (Al-Ni), PMMA plate with aluminum cylinders (PMMA-Al), and finally an aluminum plate decorated with PMMA cylinders (Al-PMMA). Sound power transmission coefficient τ in water is calculated as a function of the parallel wavevector $\mathbf{Q}_0$ in the $M\Gamma X$ directions and the normalized frequency $\omega a/\pi c_0$ for three plate thicknesses ($h/a = 0.4, 0.6, 1$) and a filling fraction $f_\square = 0.28$ for each material combination. Below the sound line the normalized evanescent transmission coefficient is plotted.

Figures 5.20(a)-(c) shows the calculations for Ni-Al PhPs and Figs. 5.20(d)-(f) those for Al-Ni PhPs. In both cases, thiner plates, i.e. $h/a = 0.4, 0.6$ (Figs. 5.20(a), (b), (d), and (e)) differ slightly from and homogeneous plate, where zero order Lamb modes are clearly distinguishable, as well as the Scholte-Stoneley-like mode just below the sound line, in agreement with the previous statement that the bigger the c_t/c_0 (2.11 in this case) ratio, the smaller the distance to the sound line of this mode. However, due to the geometry of the array it is observed some degree of anisotropy. The transmission features for the Al-Ni plate are broader than those of the Ni-Al plate in the same way than a homogeneous nickel plate displays sharper transmission features than an aluminum homogeneous plate. For the thicker plates having $h/a = 1$ (Figs. 5.20(c) and (f)) a small gap for the A_0-like Lamb mode opens.

More complex dispersion is shown in Figure 5.21 above and below the sound line as well as a stronger anisotropy. S_0 like mode is clearly steeper for Al-PMMA (Figs. 5.21(d)-

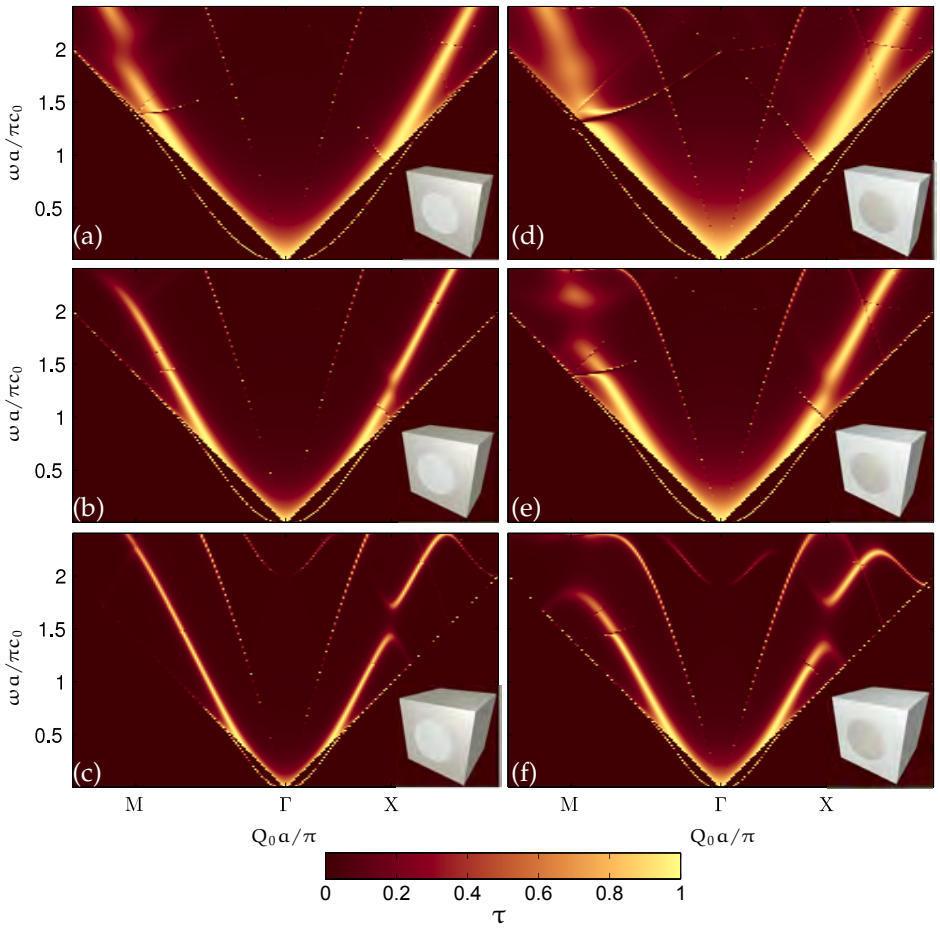

Figure 5.20: Transmitted sound power τ as a function of the parallel wavevector $\mathbf{Q}_0$ across the MΓX directions and the normalized frequency $\omega a/\pi c_0$ calculated with the FEAM model for Ni-Al (left column) and Al-Ni (right column) PhPs immersed in water having $f_\square = 0.28$ and $h/a = 0.4, 0.6, 1$. The insets depict the unit cell geometry for each case.

(f)) PhPs than for PMMA-Al plates (Figs. 5.21(a)-(c)). Scholte-Stoneley-like modes are no more as simple as in the Al-Ni, Ni-Al plates. Several gaps appear as in Fig. 5.21(c) and more interestingly, they are folded to the leaky side due to the symmetry around the M and X points. This phenomenon has been already proposed in [151, 69] to explain transmission features predicted [151] in PMMA PPPs immersed into water and

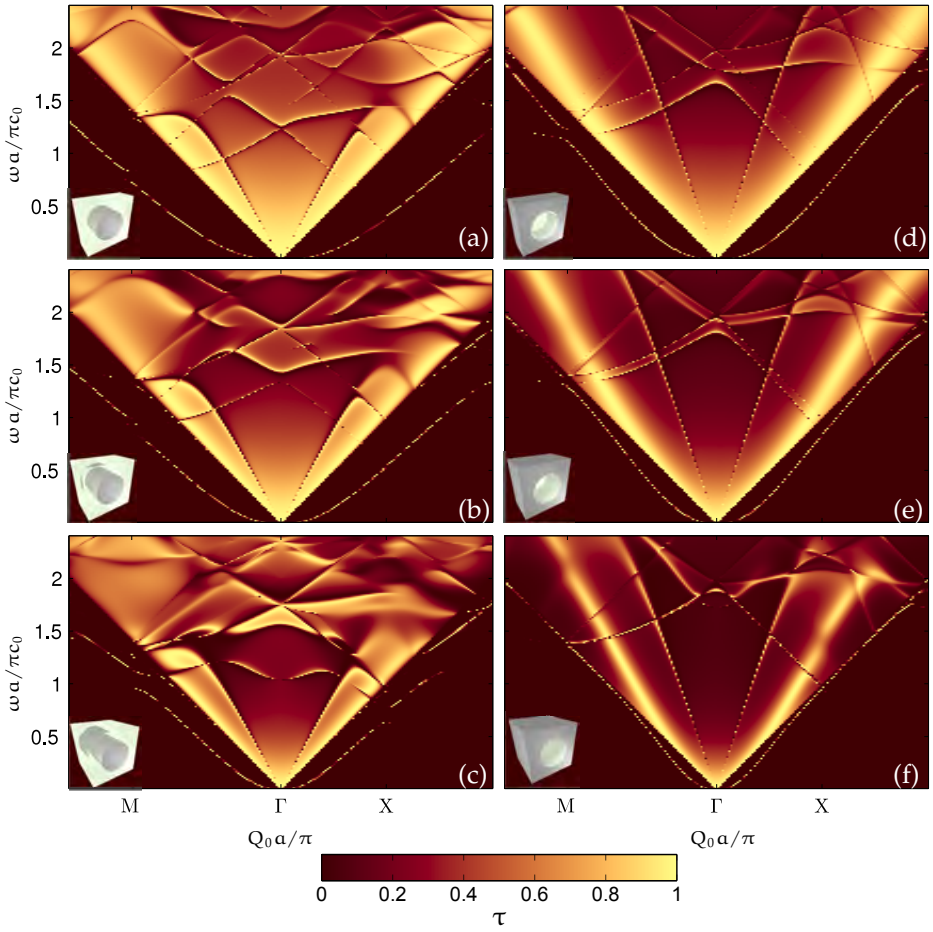

Figure 5.21: Transmitted sound power τ as a function of the parallel wavevector $\mathbf{Q}_0$ across the MΓX directions and the normalized frequency $\omega a/\pi c_0$ calculated with the FEAM model for PMMA-Al (left column) and Al-PMMA (right column) PhPs immersed in water having $f_\square = 0.28$ and $h/a = 0.4\,, 0.6\,, 1$. The insets depict the unit cell geometry for each case.

measured [69] in periodically corrugated brass plates immersed in water both at normal incidence, though no direct proof has been given yet.

These results give a complete description of the phenomena involved in PhPs as they also includes the coupling with the surrounding fluid. The Scholte-Stoneley-like modes reported here do not need a surface corrugation to be strongly confined but one of the phononic crystal constituent materials having lower c_t than the fluid. This constitutes

a key difference with fluid-solid PhPs and perforated plates together with the absence of FPRs in solid-solid PhPs. Even if the solid is considered as perfectly rigid, non-leaky modes can be induced using a corrugation [159, 45]. Although the cavity then has a closed and an open end, it still supports resonances which are intimately linked to these non-leaky modes.

6

Concluding remarks

6.1 Sound, light, and matter waves

This section, which is reported in [53], consist in comparing the behavior of light, electrons, and sound when transmitted through a hole drilled in zero and arbitrary thickness membranes under the unified framework derived in [35] and further extend the analysis to hole arrays.

Figure 6.1 summarizes the comparison between sound, electrons, and light when transmitted through a single hole in a $h = 0$ membrane. In contrast to electron and electromagnetic waves, sound scattered through the hole shows a monopolar behavior (see Eq. (2.25)) instead of dipolar response. Another difference between sound, electrons, and light is the existence of a cutoff-free mode in the acoustical case, where the whole fluid inside the hole moves in phase like an acoustic mass. Both fluid half-spaces are always connected through the hole and the limiting factor for the transmission of sound from one side to the other at the long-wavelength regime is the radiation efficiency of the aperture. This is clearly shown in Fig. 6.1 for a zero thickness screen. While almost all the sound is transmitted, even at large wavelengths, light and electrons display a strong cutoff in their transmission spectra, i.e. subwavelength sound transmission is the rule and not the exception.

Considering the previous results for a single hole interacting with different kind of waves, the following discussion focuses on extending this comparison to hole arrays. The arguments are based on an analytical analysis developed by García de Abajo et al. [53].

Wood anomalies can be analyzed from another point of view, following [35], as the

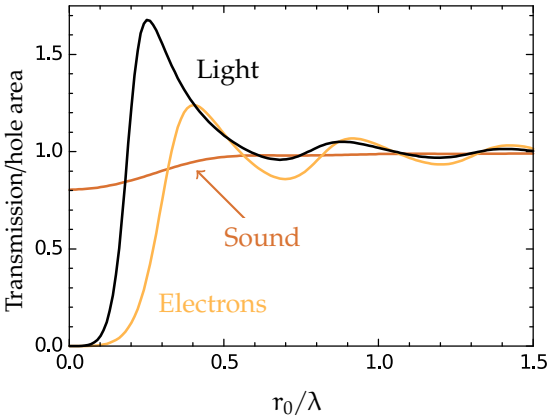

Figure 6.1: Normal-incidence transmission as a function of r_0/λ of light, electrons, and sound through a circular hole drilled in perfect conductor, infinite-potential, and rigid-solid membrane, respectively having zero-thickness.

divergence of the structure factor of the array. Under null-thickness and small hole assumptions one can relate via Babinet's principle the reflection coefficient of a disk array for electrons with the transmission coefficient of the complementary hole array for sound [53] giving

$$T = \frac{1}{1 + i\frac{Sq_0}{2\pi}\mathcal{R}e\left\{\frac{1}{\alpha} - \mathcal{G}(\mathbf{Q}_0)\right\}}, \text{ where } \quad \mathcal{G}(\mathbf{Q}_0) = \sum_{\mathbf{n}} e^{-i\mathbf{Q}_0\mathbf{r}_\mathbf{n}}\frac{e^{ik_0R}}{R} \tag{6.1}$$

corresponds to the inter-hole interaction and $\mathcal{R}e\{\alpha\} = -r_0/\pi$, $\mathcal{I}m\{\alpha^{-1}\} = -2k_0$ is the scattering coefficient of a single hole. When $\mathcal{R}e\{\mathcal{G}(\mathbf{Q}_0)\}$ diverges, the transmission becomes zero. The condition for the divergence [35] of $\mathcal{G}(\mathbf{Q}_0)$ is

$$\mathcal{G}(\mathbf{Q}_0) \propto \frac{1}{\sqrt{|\mathbf{Q}_0 + \mathbf{G}|^2 - k_0^2}}, \tag{6.2}$$

which is the same condition given before for the Wood anomaly. This approach also makes possible the analysis of the full transmission peaks, which require $\mathcal{R}e\{\alpha^{-1} - \mathcal{G}(\mathbf{Q}_0)\}$ to be zero. This condition cannot be fulfilled in the case of sound because $\mathcal{R}e\{\alpha\} < 0$ and $\mathcal{R}e\{\mathcal{G}(\mathbf{Q}_0)\} > 0$, similarly to electrons and in opposite to light [53], where full transmission occurs for arbitrarily small holes. Therefore, in the acoustic case no full transmission peak is produced due to the hole array itself as in the electromagnetic case.

Performing a similar analysis we obtained the results showed in Tab. 6.1, where the existence of different transmission properties is stated against the different kind of waves.

An opposite behavior between light and sound has been found, in contrast with the similarities emphasized by several groups [48, 49, 44]. Whereas subwavelength

Table 6.1: ST of individual small holes, ET of arrayed small holes, and surface-bound modes in arrays. The acoustic transmission of individual holes is proportional to their area, whereas arbitrarily small-hole arrays can trap light and produce full optical transmission.

Type of wave	One-hole ST	Hole-array ET	Hole-array bound states
Sound	Yes	No	No
Electrons	No	No	No
Light	No	Yes	Yes

transmission takes place for sound through a single hole, this is neither the case for electrons nor for light (see Fig. 6.1 (b)). ET and surface-bound states exist exclusively for light and not for sound or electrons.

These analytical results for null thickness membranes, although they could be considered as a specific ideal cases, portrays clearly the key role of hole resonances in the acoustic case. To illustrate this point let us consider a different geometry, for example a wall of large thickness drilled with tiny periodically distributed holes. Each hole, although having a very small aperture, still supports hole resonances dictated by the wall thickness. Then, full transmission will take place for wavelengths much larger than the hole size but not much larger than twice the wall thickness. In fact, recalling Fig. 5.3 and the results reported in [160] the transmission peak of the isolated hole is placed at larger wavelengths than the hole array full transmission peak unless the filling fraction is so small that the Wood anomaly gets involved and extremely deviates the resulting sharp full transmission peak.

In this limit, however, that sharp full transmission peak would be difficult to measure and even minimum dissipative loss could quench it. All the interesting features predicted and observed for sound impinging on a hole array embedded into a finite thickness plate such as evanescent surface modes, full transmission peaks, and subwavelength imaging strongly rely on the existence of hole resonances.

6.2 Conclusions

In summary, the transmission of ultrasound through periodically perforated plates has been studied experimentally and modeled theoretically. Different array geometries including square, triangular, and random lattices have been measured for perforated plates immersed in water including solid-solid phononic plates. The following conclusions can be derived:

A) It has been found that the transmission features of periodically perforated plates involve three different physical phenomena, namely Fabry-Pérot resonances of holes, coherent scattering due to the hole array, and elastic surface-modes of the plate. The interaction of these phenomena results in the following transmission features: a) Full transmission peaks, b) Wood anomaly minima, c) Minima and maxima from surface modes, and d) Scholte-Stoneley-like modes showing band gaps and folding. While a) and b) depend mostly on the geometrical parameters, c) and d) depend strongly on the physical properties of the constituent materials.

B) The key role of Fabry-Pérot resonances in the full transmission peaks has been demonstrated. However, periodicity is required to coherently add the contribution of each aperture, otherwise the transmission peak is quenched to a value of one half for the same global hole filling fraction. The frequency and the width of the peaks can be tuned by changing the hole filling fraction. On the other hand, the number of peaks depends on the plate thickness, the hole filling fraction, and the unit cell symmetry for compound hole arrays.

C) It has been observed that perforated plates could transmit much less sound than homogeneous plates of the same thickness due to the hydrodynamic short-circuit. Thus, a higher transmission loss can be achieved using lighter permeable barriers. Slit array and hole array sound screening could have interesting applications for underwater sound as a reflector. An optimum impedance mismatch has been found to provide a large transmission loss.

D) Two theoretical models have been derived and explained. As they differ only in the behavior of the plate, they allows us to extract the role of the plate vibration and its interaction with the modes derived from the periodical distribution of holes. The rigid-solid model shows a good agreement with the experiment at normal incidence, whereas the full elasto-acoustic model resolves properly the key transmission features for arbitrary angle of incidence despite the numerical instabilities when dealing with fluid-solid interfaces inside the plate. The numerical instabilities could be solved by using a finite element method but at a considerably higher computational cost.

E) Phononic plates have been studied theoretically and experimentally from the point of view of the sound transmission as well as in-plate propagation. Full elasto-acoustic model provides an appropriate description for studying transmission phenomena even for non-leaky modes. The transmission properties have been addressed and the folding phenomenon of non-leaky waves demonstrated.

F) It has been pointed out that in the case of sound the full transmission should not be called extraordinary transmission. In contrast to light, there is a lack of a true lattice resonance [53, 35] and, moreover, there always exist a cutoff-free mode at each hole connecting both sides of the plate, making subwavelength transmission common rather than extraordinary.

6.3 Future work

Some themes and issues that are not covered in the present work are briefly exposed in the following lines as they could lead to improvements in the field:

A) A semi-analytical model similar to the full elasto-acoustic model is required to solve the transmission through infinite fluid-solid phononic plates for high fluid-solid coupling. Such a model should give results without unphysical modes and being less computer intensive than FEM.

B) The better outcomes of the extraordinary sound screening phenomenon have been predicted for materials which cannot be found in nature. However, recent advances in polymer-metal composites could pave the way towards underwater applications. Further research in this direction may be desirable.

C) Although accurate enough to test underlying the physical phenomena, the measurement techniques can be further improved to deal with phononic plates. Synthetic aperture, ultrasonic holography, and spatial fourier analysis are possible candidates to enhance both the precision and the accuracy of the measurements.

D) Lamb waves are known by their peculiar behavior when reflected at plate edges. Therefore, it is important to know if phononic plate modes behave in the same way. This information could be important for many applications.

Appendix A

Mathematical details

A.1 Harmonic wave propagation

Starting from the equation derived in section 2.1, i.e. Eqs. (2.8) and (2.9), some basic results and relations will be given regarding mechanical waves in solids and fluids. More detailed treatment can be found in many textbooks as [78, 83, 161, 84]. Assuming harmonic time dependence, Eq. (2.8) yields

$$[\partial_j(\lambda\partial_n u_n) + \partial_n\left(\mu(\partial_n u_j + \partial_j u_n)\right)] + \rho\omega^2 u_j = 0\,. \tag{A.1}$$

If the elastic material is homogeneous isotropic the equation can be further simplified to

$$(\lambda+\mu)\nabla\left(\nabla\cdot\mathbf{u}\right) + \mu\nabla^2\mathbf{u} + \rho\omega^2\mathbf{u} = 0\,. \tag{A.2}$$

Assuming plane wave propagation of the form $\mathbf{u} = \mathbf{u}_0 e^{i\mathbf{kr}}$ and replacing into Eq. (A.2) one obtains

$$(\rho\omega^2 - \mu\mathbf{k}^2)\mathbf{u}_0 - (\lambda+\mu)\,\mathbf{k}\,(\mathbf{k}\cdot\mathbf{u}_0) = 0\,, \tag{A.3}$$

which gives two different possibilities of wave motion:

$$\text{Longitudinal waves:} \qquad \mathbf{u}_0 = u_0\hat{\mathbf{k}}\,, \qquad k_\ell = \frac{\omega}{c_\ell}\,, \qquad c_\ell = \sqrt{\frac{\lambda+2\mu}{\rho}}\,, \tag{A.4}$$

$$\text{Transverse waves:} \qquad \mathbf{u}_0\cdot\mathbf{k} = 0\,, \qquad k_t = \frac{\omega}{c_t}\,, \qquad c_t = \sqrt{\frac{\mu}{\rho}}\,. \tag{A.5}$$

We can use previous results to express the wave field in the solid as the contribution of longitudinal and transverse waves. This procedure is called the Stokes-Helmholtz

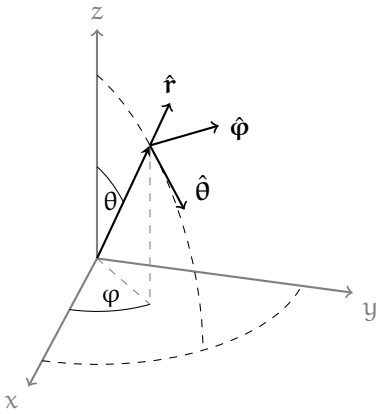

Figure A.1: Diagram of the polarization scheme for the characterization of longitudinal and transverse plane waves. The displacement for a longitudinal wave follows the same direction of the wavevector $\hat{\mathbf{k}} = \hat{\mathbf{r}}$. However, in the case of a transverse wave, the displacement is perpendicular to the wavevector and can be represented using $\hat{\theta}$ and $\hat{\boldsymbol{\varphi}}$

decomposition. Denoting ξ and ψ for longitudinal and transverse wave potentials respectively, one can write $\mathbf{u} = \bigtriangledown\xi + \bigtriangledown\times\psi$, which in two-dimensional in-plane problems takes the form

$$u_x = \partial_x\xi + \partial_z\psi\,, \quad u_z = \partial_z\xi - \partial_x\psi\,. \tag{A.6}$$

With regard to the elastic constants ρ, c_ℓ, and c_t, they are related to the Lamé coefficients by $\mu = \rho c_t^2$ and $\lambda = \rho c_\ell^2 - 2\mu = \rho\left(c_\ell^2 - 2c_t^2\right)$.

Considering linear harmonic propagation in a fluid, the particle displacement is related to the pressure by the Euler equation (2.5) as

$$\mathbf{u} = \frac{1}{\rho\omega^2}\bigtriangledown p\,. \tag{A.7}$$

In addition, Eq. (2.9) under time harmonic considerations and for an isotropic homogeneous fluid yields

$$\nabla^2 p + \frac{\omega^2}{c^2}p = 0\,, \tag{A.8}$$

which for plane waves of the form $p = p_0 e^{i\mathbf{kr}}$ gives longitudinal pressure waves for which $kc = \omega$.

A.2 Bessel functions properties

Some general properties of the Bessel functions are shown as well as some particular expressions involving them which are used through this work. The Jacobi-Anger expansion [162] that represents a plane wave in cylindrical coordinates is given by

$$e^{ix\cos\varphi} = \sum_{m=-\infty}^{\infty} i^m J_m(x) e^{im\varphi}\,, \tag{A.9}$$

The nth order Hankel transform is defined following [100] as

$$F_n(Q) = \int_0^\infty f_n(r) J_n(Qr) r \, dr \,, \tag{A.10}$$

Due to the orthogonality of the Bessel functions we get [162]

$$\int_0^\infty J_m(Qr) J_m(Q'r) r \, dr = \frac{\delta(Q-Q')}{Q} \,. \tag{A.11}$$

Whereas changing the upper limit of the latter integral one obtains [162]

$$I(Q,Q') = \int_0^{r_0} J_m(Qr) J_m(Q'r) r \, dr = \begin{cases} \dfrac{r_0^2}{2} & \text{if } Q = Q' = 0 \,, \\ \dfrac{r_0}{Q^2 - Q'^2} \left[Q' J_m(Qr_0) J_{m-1}(Q'r_0) - Q J_m(Q'r_0) J_{m-1}(Qr_0) \right] & \text{if } Q \neq Q' \,, \\ \dfrac{r_0^2}{2} \left[J_m^2(Qr_0) - J_{m-1}(Qr_0) J_{m+1}(Qr_0) \right] & \text{if } Q = Q' . \end{cases} \tag{A.12}$$

In case $J'_m(Q_{mn} r_0) = 0$ then [162]

$$I(Q_{mn}, Q_{mn'}) = \begin{cases} 0 & \text{if } Q_{mn} \neq Q_{mn'} \\ \dfrac{r_0^2}{2} J_m^2(Q_{mn} r_0) \left[1 - \dfrac{m^2}{(Q_{mn} r_0)^2} \right] & \text{if } Q_{mn} = Q_{mn'} . \end{cases} \tag{A.13}$$

From the derivation of the single hole transmission (Eqs. (2.21), (2.22)) the following integral is obtained

$$\mathbf{I}^m_{nn'} = \int_0^\infty \frac{q_{mn}}{q} I(Q_{mn}, Q) I(Q_{mn'}, Q) Q \, dQ \,, \tag{A.14}$$

An asymptotic approximation [162] for the Bessel function is

$$J_m(Qr)|_{Qr\to\infty} \approx \sqrt{\frac{2}{\pi Qr}} \cos\left(Qr - \frac{m\pi}{2} - \frac{\pi}{4} \right) . \tag{A.15}$$

A.3 Stationary phase approximation

This approximation is an asymptotic method that can be applied to evaluate the integral of Eq. (2.14c) in the farfield using spherical coordinates. The general procedure is well described in [100] and here will be applied to a particular case. First, changing to

spherical coordinates $r = R\sin\theta_T$, $z = R\cos\theta_T$ and taking the asymptotic approximation of the Bessel function (A.15) assuming large values of R, Eq. (2.14c) is rewritten as

$$p_3 \approx \sum_m e^{im\varphi} \int_0^\infty \beta^-_{Qm} \Upsilon \cos\left(QR\sin\theta_T - \frac{m\pi}{2} - \frac{\pi}{4}\right) e^{-iR\cos\theta_T(z+h)} Q\, dQ\,, \tag{A.16}$$

where

$$\Upsilon = \sqrt{\frac{2}{\pi QR\sin\theta_T}}\,, \tag{A.17}$$

Using the identity $\cos x = (e^{ix} + e^{-ix})/2$, neglecting the first exponential since there is no wave propagating backwards in region 3, and arranging terms it yields

$$p_3 \approx \sum_m i^m e^{im\varphi} e^{i\pi/4} \sqrt{\frac{1}{2\pi R\sin\theta_T}}\, I(R)\,, \tag{A.18}$$

$$I(R) = \int_0^\infty \underbrace{\beta^-_{Qm}\, \sqrt{Q}\, e^{-iqh}}_{f(Q)}\, e^{-iR(\overbrace{Q\sin\theta_T + q\cos\theta_T}^{g(Q)})}\, dQ\,. \tag{A.19}$$

Concentrating now in the phase term $g(Q) = -Q\sin\theta_T - q\cos\theta_T$ of the second exponential in Eq. (A.19), we need to determine the stationary phase point to perform the integration around it and thus take out the rapidly oscillating regions that tend to cancel. The stationary point can be found by solving $g'(Q) = 0$. In this case, the stationary point is $Q_T = k_0\sin\theta_T$. We can now replace $f(Q)$ and $g(Q)$ in the expression derived in [100] as

$$I(R) \approx f(Q_T) e^{iRg(Q_T)} e^{i\pi/4} \sqrt{\frac{2\pi}{R|g''(Q_T)|}}\,, \tag{A.20}$$

$$I(R) \approx \beta^-_{Q_T m}\, e^{-iq_T h}\, \sqrt{Q_T}\, e^{-ikR} e^{i\pi/4}\, \cos\theta_T \sqrt{\frac{2\pi k_0}{R}}\,. \tag{A.21}$$

Replacing Eq. (A.21) back in Eq. (A.16) and arranging terms yields

$$p_3 \approx iq_T\, e^{-iq_T h}\, \frac{e^{-ik_0 R}}{R} \sum_m i^m \beta^-_{Q_T m} e^{im\varphi}\,, \tag{A.22}$$

which is the same expression obtained in [97] for the transmitted farfield.

A.4 Homogeneous plate transmission

This appendix is the continuation of the derivation started in section 2.3 for the transmission of sound through an homogeneous plate. Explicit boundary conditions from Eqs. (2.12) and (2.13) applying Eqs. (A.7) and (A.6) are:

$$\frac{1}{\rho_1\omega^2}\,\partial_z\phi_1|_{z=0} = (\partial_z\xi_2 - \partial_x\psi_2)\,|_{z=0}\,, \tag{A.23a}$$

$$\frac{1}{\rho_3\omega^2}\,\partial_z\phi_3|_{z=-h} = (\partial_z\xi_2 - \partial_x\psi_2)\,|_{z=-h}\,, \tag{A.23b}$$

$$\phi_1|_{z=0} = \mu_2\left(k_{t2}^2\xi_2 + 2(\partial_x^2\xi_2 + \partial_{xz}^2\psi_2)\right)|_{z=0}\,, \tag{A.23c}$$

$$\phi_3|_{z=-h} = \mu_2\left(k_{t2}^2\xi_2 + 2(\partial_x^2\xi_2 + \partial_{xz}^2\psi_2)\right)|_{z=-h}\,, \tag{A.23d}$$

$$0 = \mu_2\left(2\partial_{xz}^2\xi_2 + \partial_z^2\psi_2 - \partial_x^2\psi_2\right)|_{z=0,-h}\,, \tag{A.23e}$$

If medium 1 and 3 have the same properties, the system can be written in matrix form as $\boldsymbol{\Lambda}\,\boldsymbol{\alpha} = \boldsymbol{\beta}$ where

$$\boldsymbol{\Lambda} = \begin{bmatrix} \boldsymbol{\Lambda}_{11} & \boldsymbol{\Lambda}_{12} \\ \boldsymbol{\Lambda}_{21} & \boldsymbol{\Lambda}_{22} \end{bmatrix}, \quad \boldsymbol{\alpha} = \begin{bmatrix} R \\ T \\ A^+ \\ A^- \\ B^+ \\ B^- \end{bmatrix}, \quad \boldsymbol{\beta} = \begin{bmatrix} \frac{k_{\ell 1z}}{\rho_1\omega^2} \\ -1 \\ 0 \\ 0 \\ 0 \\ 0 \end{bmatrix}. \tag{A.24}$$

Due to the momentum conservation in the x direction, the wavevector is simply written

as $Q = k_{\nu j} \sin\theta_{\nu j}$, however in the z direction is defined as $k_{\nu jz} = k_{\nu j} \cos\theta_{\nu j}$. Thus,

$$\boldsymbol{\Lambda}_{11} = \begin{bmatrix} \dfrac{k_{\ell 1z}}{\rho_1 \omega^2} & 0 & k_{\ell 2z} \\ 1 & 0 & \mu_2 \left(2Q^2 - k_{t2}^2\right) \\ 0 & 0 & 2Qk_{\ell 2z} \end{bmatrix}, \tag{A.25}$$

$$\boldsymbol{\Lambda}_{12} = \begin{bmatrix} -k_{\ell 2z} & Q & Q \\ \mu_2 \left(2Q^2 - k_{t2}^2\right) & -2\mu_2 Q k_{t2z} & 2\mu_2 Q k_{t2z} \\ -2Qk_{\ell 2z} & \left(2Q^2 - k_{t2}^2\right) & \left(2Q^2 - k_{t2}^2\right) \end{bmatrix}, \tag{A.26}$$

$$\boldsymbol{\Lambda}_{21} = \begin{bmatrix} 0 & -\dfrac{k_{\ell 1z}}{\rho_1 \omega^2} E_{\ell 1}^{-1} & k_{\ell 2z} E_{\ell 2}^{-1} \\ 0 & E_{\ell 1}^{-1} & \mu_2 \left(2Q^2 - k_{t2}^2\right) E_{\ell 2}^{-1} \\ 0 & 0 & 2Qk_{\ell 2z} E_{\ell 2}^{-1} \end{bmatrix}, \tag{A.27}$$

$$\boldsymbol{\Lambda}_{22} = \begin{bmatrix} -k_{\ell 2z} E_{\ell 2} & Q E_{t2}^{-1} & Q E_{t2} \\ \mu_2 \left(2Q^2 - k_{t2}^2\right) E_{\ell 2} & -2\mu_2 Q k_{t2z} E_{t2}^{-1} & 2\mu_2 Q k_{t2z} E_{t2} \\ -2Qk_{\ell 2z} E_{\ell 2} & \left(2Q^2 - k_{t2}^2\right) E_{t2}^{-1} & \left(2Q^2 - k_{t2}^2\right) E_{t2} \end{bmatrix}, \tag{A.28}$$

with $E_{\nu j} = e^{ik_{\nu j} \cos(\theta_{\nu j}) h}$. This 6×6 linear system can be solved using standard numerical routines for each $(\theta_{\ell 1},\ \omega)$ pair.

Appendix B

Extensive results

B.1 K variation in slit arrays

A more complete scenario of the influence of the impedance ratio K can be obtained performing a parameter variation. The parameter space formed by the normalized density ρ/ρ_0 and the normalized longitudinal wave velocity c_l/c_0 is shown in Fig. B.1(a). This two variables can be replaced by $K = \frac{\rho}{\rho_0}\frac{c_l}{c_0}$ and $m = \frac{c_l/c_0}{\rho/\rho_0}$ giving two new variables which appear in Fig. B.1(a) as red hyperbolas (K) and as black lines (m). While K takes 14 different values between $2 \leqslant K \leqslant 15$, $m = \{0.27, 0.58, 1.00, 1.73, 3.73\}$. However, in the solid there also exist transverse waves, whose wave velocity c_t has been chosen to fulfill the $c_l^2 - 2c_t^2 > 0$ condition as $c_t = 0.7c_l/\sqrt{2}$. Care has to be taken with the value of c_t because when it is lower than c_0 the fluid-solid interface is governed by Scholte-Stoneley waves instead of Rayleigh waves [150], although a pure interface mode exist in plates immersed in a fluid even if $c_t > c_0$ [149] in addition to leaky Lamb waves. The region in the parameter space (Fig. 1(a)) where $c_t < c_0$ has been marked with a light yellow (gray) rectangle.

A suitable quantity to address the effect upon the sound transmission of inserting periodically distributed slits in a homogeneous plate is the insertion loss, IL$= -10\log(\tau/\tau_0)$, where τ is the transmitted sound power coefficient through the slit array and τ_0 the transmitted sound power coefficient through the homogeneous plate. Both, slit array and homogeneous plate, share the same thickness and elastic constants. Figures B.1(b)-(f) show the IL of the slit array in the homogeneous plate as a function of the normalized frequency fa/c_0 and K at normal incidence for each m. The normalized IL evolves in a similar way for the five m values. The IL provided by the slit array can reach

60 dB over a homogeneous plate. The darker zones correspond to full transmission in the slit array. When K is small, several sharp peaks are present in the spectrum and the effect of the $c_t < c_0$ condition can be correlated with the existence of these extra IL peaks at frequencies between a minimum of the IL and $fa/c_0 = 1$. As K increases the peaks are shifted to higher frequencies and start to couple forming one peak which decreases as K approach to infinity. There is an optimum between $7 < K < 12$ depending on m having a relatively broad part of the spectrum with 20 dB over the homogeneous plate.

It is clear from Fig. B.1(b), that the parameter with more influence in the transmission features of slit arrays is K, whereas m has only a moderate influence. Therefore, references to m have been mostly omitted from the discussion, although it has been considered and is needed to perform the calculations.

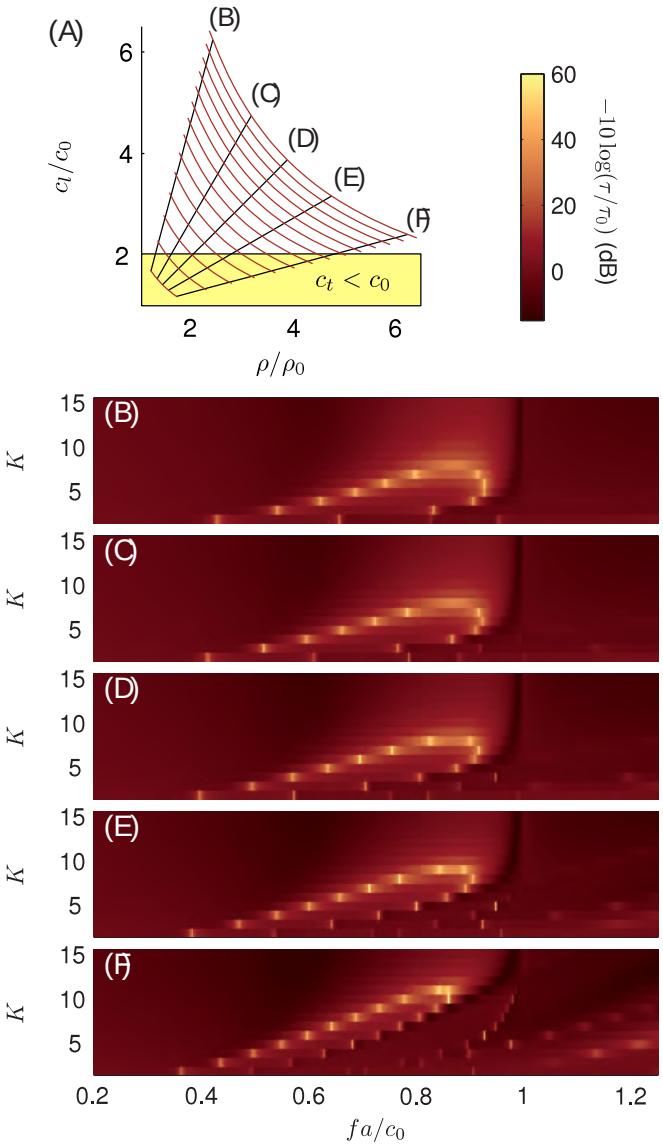

Figure B.1: (a) Parameter space for K variation as a function of ρ/ρ_0 and c_t/c_0. The curves correspond to equal-K hyperbolas and black lines show the different slopes m for which K has been varied. (b)-(f) depict the IL of the slit array in a homogeneous plate (color scale in (dB)) as a function of the normalized frequency and K. Each contour plot corresponds to a line (m) in the parameter space (a) as indicated by the labels.

List of figures

Publications

Journal articles

[1] Héctor Estrada, José María Bravo, and Francisco Meseguer. High sound screening in low impedance slit arrays. *New Journal of Physics*, 13(4):043009, 2011.

[2] Héctor Estrada, Vicente Gómez-Lozano, Antonio Uris, Pilar Candelas, Francisco Belmar, and Francisco Meseguer. Sound transmission through plates perforated with two periodic subwavelength hole arrays. *Journal of Physics: Condensed Matter*, 23(13):135401, 2011.

[3] Héctor Estrada, Pilar Candelas, Antonio Uris, Francisco Belmar, Francisco Meseguer, and F. Javier García de Abajo. Sound transmission through perforated plates with subwavelength hole arrays: A rigid-solid model. *Wave Motion.*, 48:235–242, 2011.

[4] F. J. García de Abajo, Héctor Estrada, and F. J. Meseguer. Diacritical study of light, electrons, and sound scattering by particles and holes. *New Journal of Physics*, 11(9):093013, 2009.

[5] Héctor Estrada, F. Javier García de Abajo, Pilar Candelas, Antonio Uris, Francisco Belmar, and Francisco Meseguer. Angle-dependent ultrasonic transmission through plates with subwavelength hole arrays. *Physical Review Letters*, 102(14):144301, 2009.

[6] Héctor Estrada, Pilar Candelas, Antonio Uris, Francisco Belmar, F. Javier García de Abajo, and Francisco Meseguer. Influence of lattice symmetry on ultrasound transmission through plates with subwavelength aperture arrays. *Applied Physics Letters*, 95(5):051906, 2009.

[7] Héctor Estrada, Pilar Candelas, Antonio Uris, Francisco Belmar, F. J. García de Abajo, and Francisco Meseguer. Extraordinary sound screening in perforated plates. *Physical Review Letters*, 101(8):084302, 2008.

[8] Héctor Estrada, Pilar Candelas, Antonio Uris, Francisco Belmar, Francisco Meseguer, and Francisco J. García de Abajo. Influence of the hole filling fraction on the ultrasonic transmission through plates with subwavelength aperture arrays. *Applied Physics Letters*, 93(1):011907, 2008.

Conference Papers

[1] Héctor Estrada, José María Bravo, and Francisco Meseguer. High transmission loss of slit arrays for underwater sound. In *Oceans 2011*, pages XX, Santander, Spain 2011.

[2] Héctor Estrada, Pilar Candelas, Francisco Belmar, Antonio Uris, Vicente Gómez, F. Javier García de Abajo, and Francisco Meseguer. The Role of Array Symmetry in the Transmission of Ultrasound through Periodically Perforated Plates. In *Proceedings of Phononics 2011*, pages 152-153, Santa Fe, New Mexico, USA 2011.

[3] Héctor Estrada, Pilar Candelas, Antonio Uris, Francisco Belmar, F. Javier García de Abajo, and Francisco Meseguer. Surface modes in periodically perforated plates at ultrasonic frequencies. In *Internoise2010*, page 504, Lisbon 2010.

[4] Héctor Estrada, Pilar Candelas, Antonio Uris, Francisco Belmar, F. Javier García de Abajo, and Francisco Meseguer. Ultrasonic transmission through perforated plates: periodic and random hole arrays. In *Internoise2010*, page 500, Lisbon 2010.

[5] Héctor Estrada, Francisco Meseguer, Pilar Candelas, Antonio Uris, Francisco Belmar, and F. Javier García de Abajo. Ultrasonic transmission through plates with subwavelength hole arrays. In *16th Congress on Sound and Vibration*, Krakow 2009.

[6] Héctor Estrada, Pilar Candelas, Antonio Uris, Francisco Belmar, Francisco Meseguer, and F. Javier García de Abajo. Angle-dependent ultrasonic transmission and surface modes in subwavelength hole arrays. In *4th International Conference on Surface Plasmon Photonics*, Amsterdam 2009. poster.

[7] Héctor Estrada, Pilar Candelas, Antonio Uris, Francisco Belmar, Francisco Meseguer, and F. Javier García de Abajo. Sound transmission through perforated plates. In *Spanish Conference on Nanophotonics*, Castelldefels 2008. poster.

Bibliography

[1] Felix Bloch. Über die quantenmechanik der elektronen in kristallgittern. *Zeitschrift für Physik A*, 52:555–600, 1929. (Cited on page 1.)

[2] Jian Zi, Xindi Yu, Yizhou Li, Xinhua Hu, Chun Xu, Xingjun Wang, Xiaohan Liu, and Rongtang Fu. Coloration strategies in peacock feathers. *Proceedings of the National Academy of Sciences*, 100(22):12576–12578, 2003. (Cited on pages 1 and 2.)

[3] Andrew R Parker. Natural photonics for industrial inspiration. *Philosophical Transactions of the Royal Society A*, 367(1894):1759–1782, 2009. (Cited on page 1.)

[4] Sajeev John. Strong localization of photons in certain disordered dielectric superlattices. *Physical Review Letters*, 58(23):2486–2489, 1987. (Cited on pages 1 and 2.)

[5] E. Yablonovitch and T. J. Gmitter. Photonic band structure: The face-centered-cubic case. *Physical Review Letters*, 63(18):1950–1953, 1989. (Cited on pages 1 and 2.)

[6] L. Brillouin. *Wave Propagation in Periodic Structures*. Dover, New York, 1953. (Cited on pages 1 and 29.)

[7] R. Martinez-Sala, J. Sancho, J. V. Sanchez, V. Gomez, J. Llinares, and F. Meseguer. Sound attenuation by sculpture. *Nature*, 378:241–241, 1995. (Cited on page 1.)

[8] Mihail Sigalas, Manvir S. Kushwaha, Eleftherios N. Economou, Maria Kafesaki, Ioannis E. Psarobas, and Walter Steurer. Classical vibrational modes in phononic lattices: theory and experiment. *Zeitschrift fuer Kristallographie*, 220(9-10):765–809, 2005. (Cited on page 1.)

[9] J. D. Joannopoulos, R. D. Meade, and J. N. Winn. *Photonic Crystals: Molding the Flow of Light*. Princeton University Press, 1995. (Cited on page 1.)

[10] Alvaro Blanco, Emmanuel Chomski, Serguei Grabtchak, Marta Ibisate, Sajeev John, Stephen W. Leonard, Cefe López, Francisco Meseguer, Hernán Míguez, Jessica P. Mondia, Geoffrey A. Ozin, Ovidiu Toader, and Henry M. van Driel. Large-scale synthesis of a silicon photonic crystal with a complete three-dimensional bandgap near 1.5 micrometres. *Nature*, 405(6785):437–440, 2000. (Cited on page 1.)

[11] J. V. Sánchez-Pérez, D. Caballero, R. Mártinez-Sala, C. Rubio, J. Sánchez-Dehesa, F. Meseguer, J. Llinares, and F. Gálvez. Sound attenuation by a two-dimensional array of rigid cylinders. *Physical Review Letters*, 80(24):5325–5328, 1998. (Cited on pages 2 and 4.)

[12] M. Torres, F. R. Montero de Espinosa, D. García-Pablos, and N. García. Sonic band gaps in finite elastic media: Surface states and localization phenomena in linear and point defects. *Physical Review Letters*, 82(15):3054–3057, 1999. (Cited on page 2.)

[13] Attila Mekis, J. C. Chen, I. Kurland, Shanhui Fan, Pierre R. Villeneuve, and J. D. Joannopoulos. High transmission through sharp bends in photonic crystal waveguides. *Physical Review Letters*, 77(18):3787–3790, 1996. (Cited on page 2.)

[14] A. Khelif, A. Choujaa, S. Benchabane, B. Djafari-Rouhani, and V. Laude. Guiding and bending of acoustic waves in highly confined phononic crystal waveguides. *Applied Physics Letters*, 84(22):4400–4402, 2004. (Cited on page 2.)

[15] R. A. Shelby, D. R. Smith, and S. Schultz. Experimental Verification of a Negative Index of Refraction. *Science*, 292(5514):77–79, 2001. (Cited on page 2.)

[16] Alexey Sukhovich, Li Jing, and John H. Page. Negative refraction and focusing of ultrasound in two-dimensional phononic crystals. *Physical Review B*, 77(1):014301, 2008. (Cited on page 2.)

[17] Zhengyou Liu, Xixiang Zhang, Yiwei Mao, Y. Y. Zhu, Zhiyu Yang, C. T. Chan, and Ping Sheng. Locally Resonant Sonic Materials. *Science*, 289(5485):1734–1736, 2000. (Cited on page 2.)

[18] Ulf Leonhardt. Optical Conformal Mapping. *Science*, 312(5781):1777–1780, 2006. (Cited on page 2.)

[19] Steven A Cummer and David Schurig. One path to acoustic cloaking. *New Journal of Physics*, 9(3):45, 2007. (Cited on page 2.)

[20] U. Ingard and R. H. Bolt. Absorption characteristics of acoustic material with perforated facings. *The Journal of the Acoustical Society of America*, 23(5):533–540, 1951. (Cited on page 3.)

[21] T. W. Ebbesen, H. J. Lezec, H. F. Ghaemi, T. Thio, and P. A. Wolff. Extraordinary optical transmission through sub-wavelength hole arrays. *Nature*, 391:667–669, 1998. (Cited on page 4.)

[22] H. A. Bethe. Theory of diffraction by small holes. *Physical Review*, 66(7-8):163–182, 1944. (Cited on page 4.)

[23] C. Genet and T. W. Ebbesen. Light in tiny holes. *Nature*, 445:39–46, 2007. (Cited on page 4.)

[24] J. A. Porto, F. J. García-Vidal, and J. B. Pendry. Transmission resonances on metallic gratings with very narrow slits. *Physical Review Letters*, 83(14):2845–2848, 1999. (Cited on page 4.)

[25] M. M. J. Treacy. Dynamical diffraction in metallic optical gratings. *Applied Physics Letters*, 75(5):606–608, 1999. (Cited on page 4.)

[26] Y. Takakura. Optical resonance in a narrow slit in a thick metallic screen. *Physical Review Letters*, 86(24):5601–5603, 2001. (Cited on pages 4 and 30.)

[27] A. Barbara, P. Quémerais, E. Bustarret, and T. Lopez-Rios. Optical transmission through subwavelength metallic gratings. *Physical Review B*, 66(16):161403, 2002. (Cited on page 4.)

[28] H. F. Ghaemi, Tineke Thio, D. E. Grupp, T. W. Ebbesen, and H. J. Lezec. Surface plasmons enhance optical transmission through subwavelength holes. *Physical Review B*, 58(11):6779–6782, 1998. (Cited on page 4.)

[29] T. Thio, H. F. Ghaemi, H. J. Lezec, P. A. Wolff, and T. W. Ebbesen. Surface-plasmon-enhanced transmission through hole arrays in Cr films. *Journal of the Optical Society of America B*, 16:1743–1748, 1999. (Cited on page 4.)

[30] L. Martín-Moreno, F. J. García-Vidal, H. J. Lezec, K. M. Pellerin, T. Thio, J. B. Pendry, and T. W. Ebbesen. Theory of extraordinary optical transmission through subwavelength hole arrays. *Physical Review Letters*, 86(6):1114–1117, 2001. (Cited on page 4.)

[31] J. Gómez Rivas, C. Schotsch, P. Haring Bolivar, and H. Kurz. Enhanced transmission of THz radiation through subwavelength holes. *Physical Review B*, 68(20):201306, 2003. (Cited on page 4.)

[32] S. Selcuk, K. Woo, D. B. Tanner, A. F. Hebard, A. G. Borisov, and S. V. Shabanov. Trapped electromagnetic modes and scaling in the transmittance of perforated metal films. *Physical Review Letters*, 97(6):067403, 2006. (Cited on page 4.)

[33] Y. Pang, C. Genet, and T.W. Ebbesen. Optical transmission through subwavelength slit apertures in metallic films. *Optics Communications*, 280(1):10 – 15, 2007. (Cited on page 4.)

[34] William L. Barnes, Alain Dereux, and Thomas W. Ebbesen. Surface plasmon subwavelength optics. *Nature*, 424:824–830, 2003. (Cited on page 4.)

[35] F. J. García de Abajo. Colloquium: Light scattering by particle and hole arrays. *Reviews of Modern Physics*, 79(4):1267, 2007. (Cited on pages 4, 89, 90, and 93.)

[36] F. J. Garcia-Vidal, L. Martin-Moreno, T. W. Ebbesen, and L. Kuipers. Light passing through subwavelength apertures. *Reviews of Modern Physics*, 82(1):729–787, 2010. (Cited on page 4.)

[37] Lord Rayleigh. *The Theory of Sound*, volume II. Courier Dover Publications, 2nd edition, 1945. (Cited on pages 5 and 30.)

[38] R. W. Wood. *Philosophical Magazine*, 4:396, 1902. (Cited on pages 5, 30, 58, and 61.)

[39] A. N. Norris and H. A. Luo. Acoustic radiation and reflection from a periodically perforated rigid solid. *The Journal of the Acoustical Society of America*, 82(6):2113–2122, 1987. (Cited on pages 5, 30, and 68.)

[40] J. Christensen, A. I. Fernandez-Dominguez, de F. Leon-Perez, L. Martin-Moreno, and F. J. Garcia-Vidal. Collimation of sound assisted by acoustic surface waves. *Nature Physics*, 3:851–852, 2007. (Cited on page 5.)

[41] J. Christensen, L. Martín-Moreno, and F. J. García-Vidal. Enhanced acoustical transmission and beaming effect through a single aperture. *Physical Review B*, 81(17):174104, 2010. (Cited on pages 5 and 6.)

[42] F. J. García-Vidal, L. Martín-Moreno, H. J. Lezec, and T. W. Ebbesen. Focusing light with a single subwavelength aperture flanked by surface corrugations. *Applied Physics Letters*, 83(22):4500–4502, 2003. (Cited on page 6.)

[43] Jun Mei, Bo Hou, Manzhu Ke, Shasha Peng, Han Jia, Zhengyou Liu, Jing Shi, Weijia Wen, and Ping Sheng. Acoustic wave transmission through a bull's eye structure. *Applied Physics Letters*, 92(12):124106, 2008. (Cited on page 6.)

[44] Yu Zhou, Ming-Hui Lu, Liang Feng, Xu Ni, Yan-Feng Chen, Yong-Yuan Zhu, Shi-Ning Zhu, and Nai-Ben Ming. Acoustic surface evanescent wave and its dominant contribution to extraordinary acoustic transmission and collimation of sound. *Physical Review Letters*, 104(16):164301, 2010. (Cited on pages 6 and 90.)

[45] Zhaojian He, Han Jia, Chunyin Qiu, Yangtao Ye, Rui Hao, Manzhu Ke, and Zhengyou Liu. Nonleaky surface acoustic waves on a textured rigid surface. *Physical Review B*, 83(13):132101, 2011. (Cited on pages 6 and 87.)

[46] Xiangdong Zhang. Acoustic resonant transmission through acoustic gratings with very narrow slits: Multiple-scattering numerical simulations. *Physical Review B*, 71(24):241102, 2005. (Cited on pages 6, 67, and 71.)

[47] Lin Zhou and Gregory A. Kriegsmann. Complete transmission through a periodically perforated rigid slab. *The Journal of the Acoustical Society of America*, 121(6):3288–3299, 2007. (Cited on pages 6, 30, 67, and 71.)

[48] Bo Hou, Jun Mei, Manzhu Ke, Weijia Wen, Zhengyou Liu, Jing Shi, and Ping Sheng. Tuning fabry-perot resonances via diffraction evanescent waves. *Physical Review B*, 76(5):054303, 2007. (Cited on pages 6, 30, 67, 71, and 90.)

[49] Ming-Hui Lu, Xiao-Kang Liu, Liang Feng, Jian Li, Cheng-Ping Huang, Yan-Feng Chen, Yong-Yuan Zhu, Shi-Ning Zhu, and Nai-Ben Ming. Extraordinary acoustic transmission through a 1d grating with very narrow apertures. *Physical Review Letters*, 99(17):174301, 2007. (Cited on pages 6, 30, 67, 71, and 90.)

[50] Héctor Estrada, Pilar Candelas, Antonio Uris, Francisco Belmar, Francisco Meseguer, and F. J. García de Abajo. Influence of the hole filling fraction on the ultrasonic transmission through plates with subwavelength aperture arrays. *Applied Physics Letters*, 93(1):011907, 2008. (Cited on pages 6 and 58.)

[51] J. Christensen, L. Martin-Moreno, and F. J. Garcia-Vidal. Theory of resonant acoustic transmission through subwavelength apertures. *Physical Review Letters*, 101(1):014301, 2008. (Cited on pages 6, 30, 67, and 71.)

[52] Fuzi Yang and J. R. Sambles. Resonant transmission of microwaves through a narrow metallic slit. *Physical Review Letters*, 89(6):063901, 2002. (Cited on page 6.)

[53] F. J. García de Abajo, Héctor Estrada, and F. J. Meseguer. Diacritical study of light, electrons, and sound scattering by particles and holes. *New Journal of Physics*, 11(9):093013, 2009. (Cited on pages 6, 7, 89, 90, and 93.)

[54] Nicholas J. Conard, Maria Malina, and Susanne C. Munzel. New flutes document the earliest musical tradition in southwestern germany. *Nature*, 460(7256):737–740, 2009. (Cited on page 7.)

[55] Héctor Estrada, Pilar Candelas, Antonio Uris, Francisco Belmar, F. J. García de Abajo, and Francisco Meseguer. Extraordinary sound screening in perforated plates. *Physical Review Letters*, 101(8):084302, 2008. (Cited on pages 7, 67, and 71.)

[56] Héctor Estrada, José María Bravo, and Francisco Meseguer. High sound screening in low impedance slit arrays. *New Journal of Physics*, 13(4):043009, 2011. (Cited on pages 8, 67, and 70.)

[57] Xinlong Wang. Acoustical mechanism for the extraordinary sound transmission through subwavelength apertures. *Applied Physics Letters*, 96(13):134104, 2010. (Cited on page 8.)

[58] Xinlong Wang. Theory of resonant sound transmission through small apertures on periodically perforated slabs. *Journal of Applied Physics*, 108(6):064903, 2010. (Cited on page 8.)

[59] Zhifeng Liu and Guojun Jin. Acoustic transmission resonance and suppression through double-layer subwavelength hole arrays. *Journal of Physics: Condensed Matter*, 22(30):305003, 2010. (Cited on pages 8 and 70.)

[60] J. Christensen, L. Martín-Moreno, and F. J. García-Vidal. All-angle blockage of sound by an acoustic double-fishnet metamaterial. *Applied Physics Letters*, 97(13):134106, 2010. (Cited on pages 8 and 70.)

[61] Zhifeng Liu and Guojun Jin. Resonant acoustic transmission through compound subwavelength hole arrays: the role of phase resonances. *Journal of Physics: Condensed Matter*, 21(44):445401, 2009. (Cited on pages 8, 60, 63, and 64.)

[62] Héctor Estrada, Vicente Gómez-Lozano, Antonio Uris, Pilar Candelas, Francisco Belmar, and Francisco Meseguer. Sound transmission through plates perforated with two periodic subwavelength hole arrays. *Journal of Physics: Condensed Matter*, 23(13):135401, 2011. (Cited on pages 8, 33, and 62.)

[63] Feiyan Cai, Fengming Liu, Zhaojian He, and Zhengyou Liu. High refractive-index sonic material based on periodic subwavelength structure. *Applied Physics Letters*, 91(20):203515, 2007. (Cited on page 8.)

[64] Zhifeng Liu and Guojun Jin. Phase effects in the enhanced transmission through compound subwavelength rectangular hole arrays. *Journal of Applied Physics*, 106(6):063122, 2009. (Cited on page 8.)

[65] J. Zhu, J. Christensen, J. Jung, L. Martin-Moreno, X. Yin, L. Fok, X. Zhang, and F.J. Garcia-Vidal. A holey-structured metamaterial for acoustic deep-subwavelength imaging. *Nat Phys*, 7(1):52, 2011. (Cited on page 8.)

[66] Horace Lamb. On waves in an elastic plate. *Proceedings of the Royal Society of London. Series A*, 93(648):pp. 114–128, 1917. (Cited on pages 8 and 17.)

[67] Héctor Estrada, F. J. García de Abajo, Pilar Candelas, Antonio Uris, Francisco Belmar, and Francisco Meseguer. Angle-dependent ultrasonic transmission through plates with subwavelength hole arrays. *Physical Review Letters*, 102(14):144301, 2009. (Cited on pages 8 and 72.)

[68] Héctor Estrada, Pilar Candelas, Antonio Uris, Francisco Belmar, F. J. García de Abajo, and Francisco Meseguer. Influence of lattice symmetry on ultrasound transmission through plates with subwavelength aperture arrays. *Applied Physics Letters*, 95(5):051906, 2009. (Cited on pages 8 and 73.)

[69] Zhaojian He, Han Jia, Chunyin Qiu, Shasha Peng, Xuefei Mei, Feiyan Cai, Pai Peng, Manzhu Ke, and Zhengyou Liu. Acoustic transmission enhancement through a periodically structured stiff plate without any opening. *Physical Review Letters*, 105(7):074301, 2010. (Cited on pages 8, 85, and 86.)

[70] Chen Jiu-Jiu, Qin Bo, and Cheng Jian-Chun. Complete band gaps for Lamb waves in cubic thin plates with periodically placed inclusions. *Chinese Physics Letters*, 22(7):1706–1708, 2005. (Cited on pages 8 and 34.)

[71] A. Khelif, B. Aoubiza, S. Mohammadi, A. Adibi, and V. Laude. Complete band gaps in two-dimensional phononic crystal slabs. *Physical Review E*, 74(4):046610, 2006. (Cited on pages 8 and 34.)

[72] J. O. Vasseur, P. A. Deymier, B. Djafari-Rouhani, Y. Pennec, and A-C. Hladky-Hennion. Absolute forbidden bands and waveguiding in two-dimensional phononic crystal plates. *Physical Review B*, 77(8):085415, 2008. (Cited on pages 8 and 34.)

[73] Xinya Zhang, Ted Jackson, Emmanuel Lafond, Pierre Deymier, and Jerome Vasseur. Evidence of surface acoustic wave band gaps in the phononic crystals created on thin plates. *Applied Physics Letters*, 88:041911, 2006. (Cited on pages 8 and 34.)

[74] Thomas Brunet, Jérôme Vasseur, Bernard Bonello, Bahram Djafari-Rouhani, and Anne-Christine Hladky-Hennion. Lamb waves in phononic crystal slabs with square or rectangular symmetries. *Journal of Applied Physics*, 104(4):043506, 2008. (Cited on pages 8 and 34.)

[75] Saeed Mohammadi, Ali Asghar Eftekhar, Abdelkrim Khelif, William D. Hunt, and Ali Adibi. Evidence of large high frequency complete phononic band gaps in silicon phononic crystal plates. *Applied Physics Letters*, 92(22):221905, 2008. (Cited on pages 8 and 34.)

[76] J. Pierre, O. Boyko, L. Belliard, J. O. Vasseur, and B. Bonello. Negative refraction of zero order flexural Lamb waves through a two-dimensional phononic crystal. *Applied Physics Letters*, 97(12):121919, 2010. (Cited on pages 8 and 34.)

[77] Hyung Jin Lee, Hoe Woong Kim, and Yoon Young Kim. Far-field subwavelength imaging for ultrasonic elastic waves in a plate using an elastic hyperlens. *Applied Physics Letters*, 98(24):241912, 2011. (Cited on pages 8 and 34.)

[78] R. N. Thurston. *Physical Acoustics*, volume IA: Wave Propagation in Fluids and Normal Solids. Academic Press, London, 1964. (Cited on pages 13 and 95.)

[79] L. M. Brekhovskikh and O. A. Godin. *Acoustics of Layered Media*, volume I of *Springer Serires on Wave Phenomena*. Springer-Verlag Berlin Heidelberg New York, 2nd edition edition, 1998. (Cited on page 16.)

[80] L. Cremer and M. Möser. *Technische Akustik*. Springer, 5th edition, 2003. (Cited on pages 16 and 66.)

[81] Horace Lamb. On the vibrations of an elastic plate in contact with water. *Proceedings of the Royal Society of London. Series A*, 98(690):pp. 205–216, 1920. (Cited on page 17.)

[82] Igor Aleksandrovich Viktorov. *Rayleigh and Lamb Waves*. Plenum Press, New York, 1967. (Cited on pages 17 and 20.)

[83] D. Royer and E. Dieulesaint. *Elastic Waves in Solids*, volume I. Springer-Verlag Berlin Heidelberg New York, 2000. (Cited on pages 17, 20, and 95.)

[84] Tribikram Kundu. *Ultrasonic Nondestructive Evaluation*. CRC Press LLC, 2004. (Cited on pages 17, 20, and 95.)

[85] M. F. M. Osborne and S. D. Hart. Transmission, reflection, and guiding of an exponential pulse by a steel plate in water. i. theory. *The Journal of the Acoustical Society of America*, 17(1):1–18, 1945. (Cited on pages 19 and 20.)

[86] Dong Fei, D. E. Chimenti, and Sorin V. Teles. Material property estimation in thin plates using focused, synthetic-aperture acoustic beams. *The Journal of the Acoustical Society of America*, 113(5):2599–2610, 2003. (Cited on page 20.)

[87] Stephen D. Holland and D. E. Chimenti. Air-coupled acoustic imaging with zero-group-velocity Lamb modes. *Applied Physics Letters*, 83(13):2704–2706, 2003. (Cited on page 20.)

[88] Ivan Tolstoy and Eugene Usdin. Wave propagation in elastic plates: Low and high mode dispersion. *The Journal of the Acoustical Society of America*, 29(1):37–42, 1957. (Cited on page 20.)

[89] Horace Lamb. On group - velocity. *Proceedings of the London Mathematical Society*, s2-1(1):473–479, 1904. (Cited on page 20.)

[90] Suraj Bramhavar, Claire Prada, Alexei A. Maznev, Arthur G. Every, Theodore B. Norris, and Todd W. Murray. Negative refraction and focusing of elastic Lamb waves at an interface. *Physical Review B*, 83(1):014106, 2011. (Cited on page 20.)

[91] Lord Rayleigh. On the passage of waves through apertures in plane screens, and allied problems. *Philosophical Magazine*, 43:259–272, 1897. (Cited on page 20.)

[92] Lord Rayleigh. On the incidence of aerial and electric waves upon small obstacles in the form of ellipsoids or elliptic cylinders, and on the passage of electric waves through a circular aperture in a conducting screen. *Philosophical Magazine*, 44:28–52, 1897. (Cited on page 20.)

[93] C. J. Bouwkamp. *Theoretische en Numerieke Behandeling van de Buiging door een Ronde Opening*. PhD thesis, University of Groningen, 1941. (Cited on pages 21 and 24.)

[94] C J Bouwkamp. Diffraction theory. *Reports on Progress in Physics*, 17(1):35–100, 1954. (Cited on page 21.)

[95] Y. Nomura and S. Inawashiro. On the transmission of acoustic waves through a circular channel of a thick wall. *Res. Inst. Elec. Commun*, 2:57–71, 1960. (Cited on page 21.)

[96] George P. Wilson and Walter W. Soroka. Approximation to the diffraction of sound by a circular aperture in a rigid wall of finite thickness. *The Journal of the Acoustical Society of America*, 37(2):286–297, 1965. (Cited on pages 21, 24, and 25.)

[97] Kyung H. Jun and Hyo J. Eom. Acoustic scattering from a circular aperture in a thick hard screen. *The Journal of the Acoustical Society of America*, 98(4):2324–2327, 1995. (Cited on pages 21, 23, and 98.)

[98] Franck Sgard, Hugues Nelisse, and Noureddine Atalla. On the modeling of the diffuse field sound transmission loss of finite thickness apertures. *The Journal of the Acoustical Society of America*, 122(1):302–313, 2007. (Cited on page 21.)

[99] Nicolas Trompette, Jean-Louis Barbry, Franck Sgard, and Hugues Nelisse. Sound transmission loss of rectangular and slit-shaped apertures: Experimental results and correlation with a modal model. *The Journal of the Acoustical Society of America*, 125(1):31–41, 2009. (Cited on page 21.)

[100] Earl G. Williams. *Fourier Acoustics : sound radiation and nearfield acoustical holography*. Academic Press, 1999. (Cited on pages 23, 33, 69, 97, and 98.)

[101] Lawrence E. Kinsler. *Fundamentals of acoustics*. John Wiley & Sons, 4th edition, 2000. (Cited on pages 24 and 41.)

[102] Neil W. Ashcroft and N. David Mermin. *Solid State Physics*. Harcourt College Publishers, 1976. (Cited on pages 27 and 36.)

[103] Charles Kittel. *Introduction to Solid State Physics*. John Wiley & Sons, 7th edition, 1996. (Cited on page 27.)

[104] Lord Rayleigh. On the dynamical theory of gratings. *Proceedings of the Royal Society A*, 79:399–416, 1907. (Cited on page 30.)

[105] R. W. Wood. Anomalous diffraction gratings. *Physical Review*, 48(12):928–936, 1935. (Cited on page 30.)

[106] Jochen Wauer and Tom Rother. Considerations to Rayleigh's hypothesis. *Optics Communications*, 282:339–350, 2009. (Cited on page 30.)

[107] R. Sainidou, N. Stefanou, I. E. Psarobas, and A. Modinos. Scattering of elastic waves by a periodic monolayer of spheres. *Physical Review B*, 66(2):024303, 2002. (Cited on page 34.)

[108] Waldemar Maysenholder. Sound transmission through periodically inhomogeneous anisotropic thin plates: Generalizations of cremer's thin plate theory. *Acta Acustica united with Acustica*, 84:668–680(13), 1998. (Cited on page 34.)

[109] Waldemar Maysenholder and Ralph Haberkern. Sound transmission through periodically inhomogeneous plates: Solution of the general problem by a variational formulation. *Acta Acustica united with Acustica*, 89:323–332(10), 2003. (Cited on page 34.)

[110] Jiu-Jiu Chen, Kai-Wen Zhang, Jian Gao, and Jian-Chun Cheng. Stopbands for lower-order Lamb waves in one-dimensional composite thin plates. *Physical Review B*, 73(9):094307, 2006. (Cited on page 34.)

[111] Jin-Chen Hsu and Tsung-Tsong Wu. Efficient formulation for band-structure calculations of two-dimensional phononic-crystal plates. *Physical Review B*, 74(14):144303, 2006. (Cited on page 34.)

[112] Jin-Chen Hsu and Tsung-Tsong Wu. Lamb waves in binary locally resonant phononic plates with two-dimensional lattices. *Applied Physics Letters*, 90(20):201904, 2007. (Cited on page 34.)

[113] Jia-Hong Sun and Tsung-Tsong Wu. Propagation of acoustic waves in phononic-crystal plates and waveguides using a finite-difference time-domain method. *Physical Review B*, 76(10):104304, 2007. (Cited on page 34.)

[114] A-Li Chen, Yue-Sheng Wang, Ya-Fang Guo, and Zheng-Dao Wang. Band structures of fibonacci phononic quasicrystals. *Solid State Communications*, 145:103–108, 2008. (Cited on page 34.)

[115] Bernard Bonello, Christine Charles, and Francois Ganot. Lamb waves in plates covered by a two-dimensional phononic film. *Applied Physics Letters*, 90(2):021909, 2007. (Cited on page 34.)

[116] Tsung-Tsong Wu, Zi-Gui Huang, Tzu-Chin Tsai, and Tzung-Chen Wu. Evidence of complete band gap and resonances in a plate with periodic stubbed surface. *Applied Physics Letters*, 93(11):111902, 2008. (Cited on page 34.)

[117] Y. Pennec, B. Djafari Rouhani, H. Larabi, A. Akjouj, J. N. Gillet, J. O. Vasseur, and G. Thabet. Phonon transport and waveguiding in a phononic crystal made up of cylindrical dots on a thin homogeneous plate. *Physical Review B*, 80(14):144302, 2009. (Cited on page 34.)

[118] Tzung-Chen Wu, Tsung-Tsong Wu, and Jin-Chen Hsu. Waveguiding and frequency selection of Lamb waves in a plate with a periodic stubbed surface. *Physical Review B*, 79(10):104306, 2009. (Cited on page 34.)

[119] Mourad Oudich, M. Badreddine Assouar, and Zhilin Hou. Propagation of acoustic waves and waveguiding in a two-dimensional locally resonant phononic crystal plate. *Applied Physics Letters*, 97(19):193503, 2010. (Cited on page 34.)

[120] Mourad Oudich, Yong Li, Badreddine M Assouar, and Zhilin Hou. A sonic band gap based on the locally resonant phononic plates with stubs. *New Journal of Physics*, 12(8):083049, 2010. (Cited on page 34.)

[121] Che-Yuan Sun, Jin-Chen Hsu, and Tsung-Tsong Wu. Resonant slow modes in phononic crystal plates with periodic membranes. *Applied Physics Letters*, 97(3):031902, 2010. (Cited on page 34.)

[122] Feng-Chia Hsu, Chiung-I Lee, Jin-Chen Hsu, Tsun-Che Huang, Chin-Hung Wang, and Pin Chang. Acoustic band gaps in phononic crystal strip waveguides. *Applied Physics Letters*, 96(5):051902, 2010. (Cited on page 34.)

[123] Chao-Yi Huang, Jia-Hong Sun, and Tsung-Tsong Wu. A two-port zno/silicon Lamb wave resonator using phononic crystals. *Applied Physics Letters*, 97(3):031913, 2010. (Cited on page 34.)

[124] J. O. Vasseur, A.-C. Hladky-Hennion, B. Djafari-Rouhani, F. Duval, B. Dubus, Y. Pennec, and P. A. Deymier. Waveguiding in two-dimensional piezoelectric phononic crystal plates. *Journal of Applied Physics*, 101(11):114904, 2007. (Cited on page 34.)

[125] I. V. Ostrovskii, A. B. Nadtochiy, and V. A. Klymko. Velocity dispersion of plate acoustic waves in a multidomain phononic superlattice. *Physical Review B*, 82(1):014302, 2010. (Cited on page 34.)

[126] Y. Cheng, X. J. Liu, and D. J. Wu. Temperature effects on the band gaps of Lamb waves in a one-dimensional phononic-crystal plate (l). *The Journal of the Acoustical Society of America*, 129(3):1157–1160, 2011. (Cited on page 34.)

[127] Jian Gao, Xin-Ye Zou, Jian-Chun Cheng, and Baowen Li. Band gaps of lower-order Lamb wave in thin plate with one-dimensional phononic crystal layer: Effect of substrate. *Applied Physics Letters*, 92(2):023510, 2008. (Cited on page 34.)

[128] Zhilin Hou and Badreddine M Assouar. Transmission property of the one-dimensional phononic crystal thin plate by the eigenmode matching theory. *Journal of Physics D: Applied Physics*, 41(9):095103, 2008. (Cited on page 34.)

[129] Zhilin Hou and Badreddine M. Assouar. Modeling of Lamb wave propagation in plate with two-dimensional phononic crystal layer coated on uniform substrate using plane-wave-expansion method. *Physics Letters A*, 372:2091–2097, 2008. (Cited on page 34.)

[130] Xuefeng Zhu, Tao Xu, Shengchun Liu, and Jianchun Cheng. Study of acoustic wave behavior in silicon-based one-dimensional phononic-crystal plates using harmony response analysis. *Journal of Applied Physics*, 106(10):104901, 2009. (Cited on page 34.)

[131] Abdelkrim Khelif, Younes Achaoui, Sarah Benchabane, Vincent Laude, and Boujamaa Aoubiza. Locally resonant surface acoustic wave band gaps in a two-dimensional phononic crystal of pillars on a surface. *Physical Review B*, 81(21):214303, 2010. (Cited on page 34.)

[132] Younes Achaoui, Abdelkrim Khelif, Sarah Benchabane, Laurent Robert, and Vincent Laude. Experimental observation of locally-resonant and bragg band gaps for surface guided waves in a phononic crystal of pillars. *Physical Review B*, 83(10):104201, 2011. (Cited on page 34.)

[133] Sarah Benchabane, Olivier Gaiffe, Gwenn Ulliac, Roland Salut, Younes Achaoui, and Vincent Laude. Observation of surface-guided waves in holey hypersonic phononic crystal. *Applied Physics Letters*, 98(17):171908, 2011. (Cited on page 34.)

[134] Charles M. Reinke, M. F. Su, R. H. Olsson, III, and I. El-Kady. Realization of optimal bandgaps in solid-solid, solid-air, and hybrid solid-air-solid phononic crystal slabs. *Applied Physics Letters*, 98(6):061912, 2011. (Cited on page 34.)

[135] Tsung-Tsong Wu, Yan-Ting Chen, Jia-Hong Sun, Sz-Chin Steven Lin, and Tony Jun Huang. Focusing of the lowest antisymmetric Lamb wave in a gradient-index phononic crystal plate. *Applied Physics Letters*, 98(17):171911, 2011. (Cited on page 34.)

[136] W. Xiao, G.W. Zeng, and Y.S. Cheng. Flexural vibration band gaps in a thin plate containing a periodic array of hemmed discs. *Applied Acoustics*, 69(3):255 – 261, 2008. (Cited on page 34.)

[137] Mohamed Farhat, Sebastien Guenneau, and Stefan Enoch. High directivity and confinement of flexural waves through ultra-refraction in thin perforated plates. *EPL (Europhysics Letters)*, 91(5):54003, 2010. (Cited on page 34.)

[138] Mohamed Farhat, Sebastien Guenneau, Stefan Enoch, Alexander B. Movchan, and Gunnar G. Petursson. Focussing bending waves via negative refraction in perforated thin plates. *Applied Physics Letters*, 96(8):081909, 2010. (Cited on page 34.)

[139] Yukihiro Tanaka and Shin-ichiro Tamura. Surface acoustic waves in two-dimensional periodic elastic structures. *Physical Review B*, 58(12):7958–7965, 1998. (Cited on page 36.)

[140] Yukihiro Tanaka, Yoshinobu Tomoyasu, and Shin-ichiro Tamura. Band structure of acoustic waves in phononic lattices: Two-dimensional composites with large acoustic mismatch. *Physical Review B*, 62(11):7387–7392, 2000. (Cited on page 40.)

[141] H. J. Wintle. Kramers–Kronig analysis of polymer acoustic data. *Journal of Applied Physics*, 85(1):44–48, 1999. (Cited on page 41.)

[142] Steffen Marburg and Bodo Nolte, editors. *Computational Acoustics of Noise Propagation in Fluids*. Springer-Verlag Berlin Heidelberg, 2008. (Cited on page 41.)

[143] Jean-Pierre Berenger. A perfectly matched layer for the absorption of electromagnetic waves. *Journal of Computational Physics*, 114(2):185 – 200, 1994. (Cited on page 42.)

[144] X. Jia. Modal analysis of Lamb wave generation in elastic plates by liquid wedge transducers. *The Journal of the Acoustical Society of America*, 101(2):834–842, 1997. (Cited on page 51.)

[145] Ismael Núñez, Ros K. Ing, Carlos Negreira, and Mathias Fink. Transfer and green functions based on modal analysis for Lamb waves generation. *The Journal of the Acoustical Society of America*, 107(5):2370–2378, 2000. (Cited on page 51.)

[146] D. Alleyne and P. Cawley. A two-dimensional fourier transform method for the measurement of propagating multimode signals. *The Journal of the Acoustical Society of America*, 89(3):1159–1168, 1991. (Cited on page 51.)

[147] P. M. Morse and K. U. Ingard. *Theoretical Acoustics*. Princeton University Press, 1986. (Cited on page 52.)

[148] David R. Lide, editor. *Handbook of Chemistry and Physics*. CRC Press LLC, 84th edition, 2003-2004. (Cited on page 52.)

[149] I.A Viktorov. *Rayleigh and Lamb Waves: Physical Theories and Applications*. Plenum Press, New York, 1967. (Cited on pages 56 and 101.)

[150] Christ Glorieux, Kris Van de Rostyne, Keith Nelson, Weimin Gao, Walter Lauriks, and Jan Thoen. On the character of acoustic waves at the interface between hard and soft solids and liquids. *The Journal of the Acoustical Society of America*, 110(3):1299–1306, 2001. (Cited on pages 56, 84, and 101.)

[151] Fengming Liu, Feiyan Cai, Yiqun Ding, and Zhengyou Liu. Tunable transmission spectra of acoustic waves through double phononic crystal slabs. *Applied Physics Letters*, 92(10):103504, 2008. (Cited on pages 68, 70, and 85.)

[152] David Shiga. A hole new way of get a bit of peace and quiet. New Scientist, August 2008. (Cited on page 70.)

[153] Hamish Johnston. Holes prevent sound from passing through plate. Physicsworld.com, September 2008. (Cited on page 70.)

[154] Charles Q. Choi. Blocking sound with holes. Scientific American, December 2008. (Cited on page 70.)

[155] Marieke Hannink. *Acoustic resonators for the reduction of sound radiation and transmission*. PhD thesis, University of Twente, Enschede, The Netherlands, 2007. (Cited on page 70.)

[156] D. Takahashi. Excess sound absorption due to periodically arranged absorptive materials. *The Journal of the Acoustical Society of America*, 86(6):2215–2222, 1989. (Cited on page 72.)

[157] F.P. Mechel. Sound fields at periodic absorbers. *Journal of Sound and Vibration*, 136(3):379 – 412, 1990. (Cited on page 72.)

[158] Daniel Torrent and José Sánchez-Dehesa. Acoustic metamaterials for new two-dimensional sonic devices. *New Journal of Physics*, 9(9):323, 2007. (Cited on page 72.)

[159] Luc Kelders, Walter Lauriks, and Jean F. Allard. Surface waves above thin porous layers saturated by air at ultrasonic frequencies. *The Journal of the Acoustical Society of America*, 104(2):882–889, 1998. (Cited on page 87.)

[160] Héctor Estrada, Pilar Candelas, Antonio Uris, Francisco Belmar, Francisco Meseguer, and F. J. García de Abajo. Sound transmission through perforated plates with subwavelength hole arrays: A rigid-solid model. *Wave Motion*, 48(3):235 – 242, 2011. (Cited on page 91.)

[161] L.D. Landau and E. M. Lifshitz. *Theory of Elasticity*. Course of Theoretical Physics. Butterworth-Heinemann, Oxford, 3rd edition, 1986. (Cited on page 95.)

[162] Milton Abramowitz and Irene A. Stegun. *Handbook of Mathematical Functions with Formulas, Graphs, and Mathematical Tables*. Dover, New York, ninth dover printing, tenth gpo printing edition, 1964. (Cited on pages 96 and 97.)